UNIVERSITA' DEGLI STUDI DI NAPOLI ''FEDERICO II''

SCUOLA POLITECNICA E DELLE SCIENZE DI BASE
Department of Chemical, Materials and Production Engineering

Ph.D. Thesis in
INDUSTRIAL PRODUCT AND PROCESS ENGINEERING
XXXII CYCLE

A microfluidic platform to design nanostructures with improved multi-modal imaging properties

Ph.D. Candidate

Olimpia Tammaro

Supervisors

Paolo Antonio Netti
Professor of Biomaterials and Tissue Engineering at UNINA, Italy

Enza Torino
Researcher in Bioengineering at UNINA, Italy

Luisa De Cola
Professor of Supramolecular and Bio-Material Chemistry at University of Strasbourg,ISIS, France

Ph.D. program Coordinator
Giuseppe Mensitieri
Professor of Materials Science and Engineering, UNINA, Italy

2017-2020

AUTHOR

Olimpia Tammaro

SUPERVISOR

Prof. Dr. Paolo A. Netti

Eng. Enza Torino

Prof. Luisa De Cola

COORDINATOR

Prof. Dr. Giuseppe Mensitieri

Abstract

Nowadays, researchers are making many efforts in the medical field leading to new therapy and diagnosis methods exploiting opportunities given by nanotechnology innovation. For example, the combination of different imaging modalities can give the opportunity to obtain morphological and functional information simultaneously, providing a more accurate diagnosis. This advancement can be reached through the use of multimodal tracers and nanotechnology-based solutions allowing the simultaneous delivery of different diagnostic compounds and their safe administration for multimodal imaging acquisition. In this way is possible to protect the cargo molecules. Furthermore, a fundamental aspect is due to a proper design of the nanovectors used, correlating it with respect to the target purpose. Among different materials and processes available, nanoprecipitation is a consolidate method for polymeric nanoparticle production and its implementation in microfluidics can further improve the control over final product features accelerating its potential clinical translation. In this scenario, a Hydrodynamic Flow Focusing (HFF) approach is proposed and investigated as a production route to synthesis through a ONE-STEP process pegylated crosslinked Hyaluronic Acid NanoParticles (PEG-cHANPs). A feasibility study has been conducted to define the principal guidelines in terms of size and stability for the produced nanosystem. Based on the obtained results, a set of conditions has been elected as “gold conditions” and used in the following parts. To exploit the versatility of our microfluidic (μF) platform, the ONE-STEP process has been implemented to generate more complex structures with differents loaded agent.

First, we have demonstrated that a homogeneous population of NPs with an average size of 140 nm is obtained and Gadolinium-based contrast agent (Gd-DTPA CA) and ATTO488 compounds are co-encapsulated simultaneously during the ONE-STEP process The results showed that the obtained architectures can be used as multimodal Magnetic Resonance Imaging (MRI)/Optical imaging probe. Furthermore, in accordance with the Hydrodenticity concept, a boosting of the T1 values is obtained with respect to the free Gd-DTPA.

Thereafter, we have synthesized hybrid materials combining SiO_2 and HA-PEG hydrogels loaded with Gd-DTPA as new MRI probes. Pre-synthetized SiO_2 NPs have been added to the solvent phase during the ONE-STEP process. In this case, silica nanoparticles act as a templating agent, interfering with the nanoprecipitation step during the HFF. Resulting hybrid nanosystems have been characterized in terms of size, morphology and T1 values.

Intending to develop new probes for combining MRI/Near-Infrared Fluorescence Imaging (NIRF), we explore the possibility to co-encapsulate Gd-DTPA and Indocyanine Green (ICG) in the ONE-STEP process for PEG-cHANPs production. ICG is the only NIRF dye approved by Food and Drug Administration, but its use is restricted by its low stability in biological media. Here we report a stability study of ICG regarding its interaction with the materials involved in PEG-cHANPs production and preliminary characterization of PEG-cHANPs loaded with ICG as Reactive Oxygen Species generators.

Preliminary *in-vitro* tests with different cells lines have been conducted to evaluate the PEG-cHANPs-Gd-DTPA-ATTO488 behaviour for biological application.

List of Abbreviations

APTES: (3-Aminopropyl) triethoxysilane

ATR-FTIR: Attenuated Total Reflection- Fourier-Transform Infrared Spectroscopy

BBB: Blood Brain Barrier

BCA Assay: Bicinchoninic Acid Assay

CAs: Contrast Agents

cHANPs: crosslinked Hyaluronic Acid Nanoparticles

CM: Complete Medium

CT: Computed Tomography

CTAB: Cetyltrimethylammonium bromide

DDS: Drug Delivery Systems

DLS: Dynamic Light Scattering

DMPO: 5,5-Dimethyl-1-pyrroline N-oxide

DVS: Divynil Sulfone

ECM: Extracellular matrix

EE: Encapsulation Efficacy

EPR effect: Enhanced Permeability and Retention effect

EPR: Electron Paramagnetic Resonance

EtOH: Ethanol

FBS: Fetal Bovin Serum

FDA: Food and Drug Administration

FR^2: Flow Rate Ratio

Gd: Gadolinium

Gd-DTPA: diethylenetriaminepentaacetic acid gadolinium(iii) dihydrogen salt hydrate;

HA: Hyaluronic Acid

HA-NPs: Hyaluronic Acid Nanoparticles

HA-SH: Thiolated Hyaluronic Acid

HFF: Hydrodynamics Flow Focusing regimen

HSA: Human Serum Albumin

ICG: Indocyanine Green

ICP-MS: Inductive Coupled Plasma Mass Spectroscopy

MRI: Magnetic Resonance Imaging

MSP: Mesoporous Silica Particles

NIR: Near InfraRed

NPs: Nanoparticles

PBS: Phosphate Saline Buffer

PDT: Photodynamic Therapy

PEG-cHANPs: PEGylated crosslinked Hyaluronic Acid Nanoparticles

PEG-VS: PEG-vinylsulfone

PET: Positron Emission Tomography

PTT: Photothermal Therapy

RB: Round Bottle

RES: Reticuloendothelial System

ROS: Reactive Oxygen Species

SANS: Small-Angle Neutron Scattering

SEM: Scanning Electron Microscopy

SPECT: Single-Photon Emission Computed Tomography

STEM: Scanning Transmission Electron Microscopy

TEA: triethanolamine

TEM: Transmission Electron Microscopy

TEOS: Tetraethyl Orthosilicate

TGA: Thermogravimetric Analysis

TNPs: Theranostic Nanoparticles

WS: Working Solution

ζ-Pot: Zeta Potential

µF: Microfluidics

Table of contents

Chapter 1

STATE OF THE ART

1.1 NanoParticles and NanoMedicine

Nowadays terms like "NanoParticles", "NanoTechnologies" and "NanoMedicine" are common in the daily language, but their origins are farther back in time. One of the most famous examples of the use of nanoparticles in ancient times is the *Lycurgus Cup*, dating from the IV century AD. In this artefact, the presence of metallic particles (silver and gold) typically with a diameter of 50–100 nm, provides unusual properties under light exposition[1]. Nevertheless, the concept *nanoscience* was introduced for the first time by the Nobel Prize Laureate R. Feynman at the end of 1959. In his talk, Feynman described a process in which scientists would be able to manipulate and control individual atoms and molecules[2]. Over a decade later, in his explorations of ultraprecision machining, Professor Norio Taniguchi coined the term "NanoTechnology"[3]. However, the real age of nanotechnologies was born in the 80s, after the development of the Scanning Tunneling Microscope (STM)[4] and the Atomic Force Microscope (AFM)[5], as new tools that make possible to investigating the matter at atomic level[6]. Starting from this point, in the last decades it was observed an increasing number of studies and applications of nanomaterials in different fields, due to their interesting electronic, magnetic, optical and biological properties[7-12].

Nanoparticles (NPs) are generally defined as any particulate material of any shape such as a sphere, rod, wire, etc. for which at least one dimension lies in the range of 1−100 nm[13]. In *Figure 1. 1* is reported a schematic representation of several nanoparticles used for medical applications. Thanks to their versatility, nanomaterials, which can be divided into three main categories (organic, inorganic or hybrid), offer a broad range of applications in various domains such as cosmetics, environment, electronics [14,15].

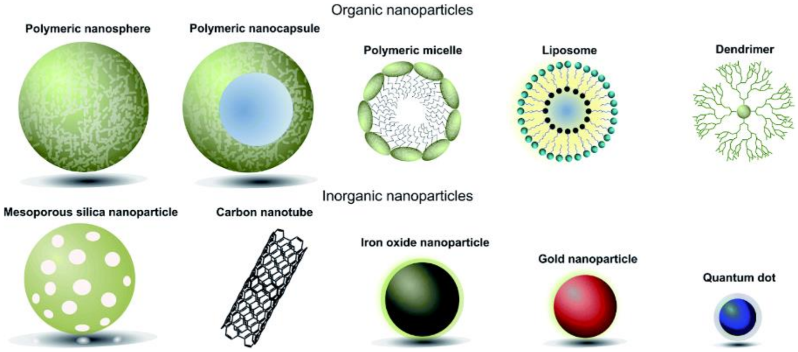

Figure 1. 1: Schematic representation of several types of nanoparticles for biomedical applications. Reproduced from A. Richards, D., Maruani, A. & Chudasama, V. Antibody fragments as nanoparticle targeting ligands: a step in the right direction. Chemical Science 8, 63-77 (2017)

In particular, their unique features make this class of materials very fascinating for biomedical applications opening a new field of research defined as Nanomedicine by National Institute of Health in USA[16].

Indeed, the nanometric size is also the scale of many biological mechanisms in the human body allowing nanoparticles and nanomaterials to potentially cross natural barriers to access new sites of delivery and to interact with DNA or small proteins at different levels, in blood or within organs, tissues or cells. Nanomaterials for medicine have a number of applications in several disciplines, such as oncology, cardiology and neurology, because pathological and physiological processes occur at the level of cells [17,18]. Engineered nanomaterials can be used in different ways, such as drug delivery systems, diagnostic agents, for the detection of a specific compound and gene delivery (*Figure 1. 2*).

Other advantages of nanomedicine include specific binding of drugs to targets in cancer cells or the disease microenvironment, simultaneous visualization of tumors using innovative imaging techniques, enhanced drug-circulation times, controlled drug-release kinetics, and superior dose scheduling for improved patient compliance[19,20].

However, nanomedicine for cancer therapy is advantageous over conventional medicine because it has the potential to enable the preferential delivery of drugs to tumors owing to the enhanced permeability and retention (EPR) effect, and the delivery of more than one therapeutic agent for combination therapy. medicine seeks to address various medical challenges and shortcomings faced by conventional medicine, which include poor bioavailability, impaired target specificity, systemic and organ toxicity, etc [21].

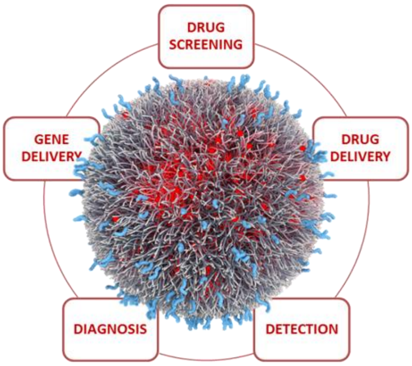

Figure 1. 2 Applications and research targets of nanomedicine. Nanoparticles have been designed in a rational way in order to turn these nanomaterials into biosensors, molecular-scale fluorescent tags, imaging agents, targeted molecular delivery vehicles, and other useful biological tools.

Nanomaterials with different physicochemical properties exhibit different *in vitro* and *in vivo* behaviour and consequently could be used for different applications. When the NPs are intravenously injected, they are transported along the blood vessels and accumulate in disparate organs through different mechanisms depending on their size[22]. Large particles (size > 7 µm) could be entrapped in the smallest capillaries of the lung[23], while system with an average size around 5 µm could be preferentially accumulated in the organ of the reticulo-endothelial system (RES) after the opsonization and subsequent uptake by resident macrophages; instead, particles smaller than 500nm could passively extravasate and accumulate in tumor site by the EPR effect[24].

Decuzzi *et al.* investigate the biodistribution of uncoated silica beads and not conjugated with any specific ligand, with different sizes from 0,7 to 3µm, injected into tumor bearing mice, showing a steady increase of silica accumulation as the bead diameter decrease. The organs with the higher content of Si are spleen, lungs and liver. They also investigate the shape-dependent accumulation in the major organs, testing also discoidal, hemispherical and cylindrical particles. In the lungs, discoidal particles represent the major accumulation, while in the liver the most accumulated are the cylindrical ones. In the spleen, discoidal and quasi-hemispherical particles behave nearly the same and accumulate more than the cylindrical particles and the spherical beads[22]. Parameters such as size and shape are involved not only in the biodistribution but also in the fluidodynamic behaviour in the blood vessel. Hemorheology studies have been conducted to understand nanoparticles behaviour in blood vessels.

As reported by Blanco and co-worker[25], nonspherical particles, such as those possessing discoidal geometries, are more prone to tumbling and oscillatory effects in the vasculature, increasing greatly the propensity of nanoparticles-wall contact and potential extravasion through fenestration in vasculate. Once in contact with endothelial cells, the small size and surface area of conventional spherical nanoparticles reduce the number of binding and contact points compared with larger, discoidal nanoparticles (as well as other nonspherical geometries), which can affect tumour accumulation and active targeting strategies.

A better knowledge of NPs features and their influence is mandatory in order to overcome the major barrier in cancer nanomedicine[26]. Exploiting a rational design, NPs could be modulated in terms of size, shape and surface charge. Different studies have been conducted in order to establish the influence of shape, size or surface charge in the biodistribution and crossing ability of the different biological barriers. Different materials offer in addition the possibility of surface functionalization with specific ligand or polymer in order to escape from immune response such as opsonization by macrophage capture and to achieve a specific target.

Surface charge and shape of nanoparticles are crucial in extravasation, in interstitial transport and in targeting, while size affects circulation time in bloodstream, in renal clearance and can be optimized for each tumour. All these properties play an active role in determining the circulation of NPs in the bloodstream to modulating cellular responses[27,28].

NPs' design and production present some issues that still need to be overcome. The first problem concerns the size distribution of the NPs; indeed, high polydispersity can compromise the pharmacokinetics and the efficacy of the treatment.

Furthermore, NPs need to be biocompatible and low toxic *in vivo*. In addition, sterility conditions must be preserved through all the production processes.

To understand better NPs' advantages, it is important to know those differences between tumour and normal tissues that can influence the delivery of diagnostic or therapeutic agents. In fact, during their travel toward the target, NPs flow in the bloodstream, overcome vessel walls and penetrate through interstitial space to reach target cells.

To obtain a desirable effect, it is necessary the overpassing a series of obstacles that can reduce bioavailability and therapeutic or diagnostic efficacy. Macrophages and monocytes of the reticuloendothelial system (RES) are highly efficient at removing NPs through opsonization. Digestive enzymes and low pH contribute to the rapid degradation of NPs, while the renal system rapidly filter NPs with diameter under 10 nm. Therefore, it is important to understand all factors affecting biodistribution to develop successful nanostructured drug delivery systems.

In tumour tissues, these aspects become abnormal: tortuous and leaky vessels, heterogeneous blood flow, lack of functional lymphatic vessels, vascular hyperpermeability owing to vessel walls irregular structure, a uniformly elevated interstitial fluid pressure (IFP) that reduces pressure gradients across vessel wall and so convective transport, a dense Extracellular Matrix (ECM) with high collagen-fibers concentration that hinders diffusion. All these issues can be resolved using engineered nanoparticles.

1.2 Theranostic

The possibility to combine in only one nanocarrier, at the same time, different compounds for different aim, therapeutic and diagnosis, make enable the introduction of a new concept: “theranostic”. The term is defined as the possibility of exploiting a single agent for diagnostic and therapeutic purposes simultaneously. Administering a theranostic agent gave the possibility of being able to combine different contrast agents or radiopharmaceuticals for diagnostic aims developed over time with the release of specific drugs or supplements for different types of diseases, tumor lesions, tissue degenerations, neurodegenerative pathologies as Alzheimer`s disease and inflammations[16]. Nowadays, the difficult to project the design of a theranostic nanovector (TNPs) is to combine the use of biocompatible materials to exploit their properties and peculiarities in order to achieve structures that can increase the efficiency of diagnosis, increase the therapeutic effects and at the same time control that the two mechanisms occur at different time. Indeed, the clearance of a vector, in fact, is another key factor, it must be fast enough to allow the elimination of a diagnostic agent such as a contrast medium or a radiopharmaceutical from the bloodstream but sufficiently slow to allow the controlled release of a drug, a supplement or a therapeutic substance that we want to encapsulate in. The development of effective TNPs will require some give and take between imaging sensitivity, the accuracy of targeting, and controlled drug release. Via a host of materials, many pathways are being explored to reach these goals.

In the therapeutic area, there are many different methods for administering a therapeutic agent, such as administration through the oral cavity, through injection by different routes, through the nasal mucosa, through the use of surgically implantable devices or through drug delivery by micro and nanocarriers. Controlled Drug Delivery technology represents one of the most rapidly developing areas that offers numerous advantages compared to conventional dosage forms including improved efficacy and reduced toxicity[29]. In addition, the diagnostic field aims to reach an even more high-resolution image in order to have early detection of different kinds of diseases[20,30].

1.2.1 Therapeutic Agent

Currently, the most typical cancer treatments in the clinic include chemotherapy, radiotherapy and surgery. Theranostics extensively employ these therapeutic strategies, aiming to reduce the severe side effects of chemotherapy and radiotherapy, as well as to avoid the high risk, large trauma and complications of surgery. Moreover, with the help of nanotechnology, theranostics may promote the diversification of therapeutic approaches such as photothermal therapy (PTT), photodynamic therapy (PDT) and immunotherapy[31].

Chemotherapy uses one or more anti-cancer drugs (chemotherapeutic agents). Traditional chemotherapeutic agents are cytotoxic by means of interfering with cell division (mitosis) but cancer cells vary widely in their susceptibility to these agents. To a large extent, chemotherapy can be thought of as a way to damage or stress cells, which may then lead to cell death if apoptosis is initiated. Many of the side effects of chemotherapy can be traced to damage to normal cells that divide rapidly and are thus sensitive to anti-mitotic drugs. The most common side-effects of chemotherapy are decreased production of blood cells, hence immunosuppression, inflammation of the lining of the digestive tract, and hair loss. Because of the effect on immune cells (especially lymphocytes), chemotherapy drugs often find use in a host of diseases that result from harmful overactivity of the immune system against self (so-called autoimmunity)[32,33]. In photodynamic therapy, a particle (photosensitizer) is placed within the body and it is illuminated with light from the outside. The light energy absorbed by the particle is transferred to surrounding tissue and causes the production of cytotoxic reactive oxygen species (ROS) which leads to cell apoptosis and destruction of the diseased tissue. Side effects and toxic trails are not found for this kind of therapy but the disadvantage is the possible allergic reaction caused by light[34]. Also, photothermal therapy uses external light, absorbed by organic dye and inorganic nanoparticles, but in this case the absorbed light energy is converted in heath that kills cancer cells through hyperthermia. The efficacy of this therapy is limited by the light penetration depth (used mainly for skin cancer)[35,36].

1.2.2 Diagnosis Compartment

Imaging modality plays a crucial role in a theranostic system. The most commonly applied imaging techniques in preclinical research and clinical trials include optical imaging, magnetic resonance imaging, acoustical imaging, radionuclide based imaging and computed tomography. These imaging techniques can provide excellent sensitivity, resolution and specificity for precise, sensitive, and reliable diagnosis and effective therapy in personalized treatment, thus promoting the exploration of ideal imaging probes for the construction of novel theranostic systems[31].

- Optical imaging

Optical imaging is one of the more common modalities used in research. Optical imaging utilizes photons emitted from bioluminescent or fluorescent probes. It has advantages over other imaging modalities in that the detection of low energy photons is relatively inexpensive; furthermore, the spectrum from visible to near-infrared (NIR) light provides good spatial resolution, without exposure to ionizing radiation. Unfortunately, this modality suffers from poor tissue penetration (0–2 cm) and fluorescent imaging is highly susceptible to noise due to the tissue scattering of photons in the visible light region (395–600 nm). Optical imaging also suffers from significant background because of tissue autofluorescence and light absorption by proteins (257–280 nm), and even water (above 900 nm). Despite these challenges, the NIR (700–900 nm) window has the advantages of reduced autofluorescence, reduced tissue scattering, and greater depth of penetration, which is most suitable for *in vivo* imaging[30].

• Magnetic resonance imaging (MRI)

Magnetic Resonance Imaging (MRI) is a routinely applied diagnostic imaging tool because of its not invasive nature and its ability to obtain three-dimensional tomographical information of soft tissues. Furthermore, it can be used for visualizing functions of cardiac, brain, and central nervous systems, as well as detecting tumours. The basis for the MRI signal is the precession of water hydrogen nuclei within an applied magnetic field. After the application of radiofrequency pulses, the relaxation process through which the nuclei return to the original aligned state can be exploited to produce an image. To enhance the differentiation between tissues, Contrast Agents (CAs) are used to shorten the relaxation parameters (T1 and T2) of water. Paramagnetic molecules such as gadolinium (Gd) and manganese (Mn) can be tagged into small molecules, macromolecules, or nanoparticles. Conversely, magnetic iron-oxide nanoparticles are inherently superparamagnetic and can be tagged at their surfaces with cargo. For Gd-based CAs, they enhance the signal in

T1-weighted images, otherwise super-paramagnetic iron-oxide (SPIO) conjugates provide a strong contrast effect in T2-weighted images. To offset this, relatively high concentrations of contrast agents are required to produce a detectable signal. The administration of high doses of these contrast agents leads to concerns over accumulation and toxicity, which have become a significant issue for Gd (III) complexes. While Gd (III) provides superior contrast for tumor and vascular imaging, problems with slow excretion and toxicity due to long-term accumulation may hinder its future development in the clinic.

Although MRI enables visualization of tissues at high spatial resolution without using ionizing radiation or invasive procedures[37], it is largely limited because it lacks the proper sensitivity, which is significantly lower than other imaging modalities, such as PET/SPECT[38-41].

• Acoustical imaging

UltraSound (US) is one of the most common clinical imaging modalities due to its low cost, speed, simplicity, and safety. In this modality, a transducer that emits high-frequency sound waves (N20 kHz) is placed against the skin and US images are obtained based on the sound wave reflected back from the internal organs. US contrast agents can improve imaging by introducing a material with different acoustic properties from that of tissues, such as gas[42].

Radionuclide-based imaging

γ-ray emissions are the basis for single-photon computed tomography (SPECT) and positron emission tomography (PET). For both modalities, radiopharmaceuticals are administered and can be detected by a camera. SPECT and PET images are acquired over a nominally low background signal and require little signal amplification since the gamma rays have energies in the megavolt range. SPECT and PET are quantitative techniques, which is an advantage over other modalities such as MRI and optical imaging. Although PET suffers from poor spatial resolution, this can be overcome by hybrid imaging, where PET is used to track molecular events and high-resolution CT is used to localize events (PET/CT multimodal imaging).

Computed Tomography (CT)

CT provides anatomical information. CT measures the absorption of X-rays as they pass through tissues. The ability of CT to distinguish tissues is based on the fact that different tissues provide distinct degrees of X-ray attenuation, where the attenuation coefficient depends on the atomic number and electron density of the tissues. Differences in absorption between bone, fat, air, and water produce high contrast images of anatomical structures. Currently, CT contrast agents are typically low molecular weight and are characterized by rapid extravasation and clearance.

Multimodality Imaging

Single-modality imaging may not satisfy the correct localization of tumour sites. The development of a more sophisticated theranostic nanoplatform for multimodal imaging-guided therapy is highly desired. In multimodality imaging, the need to combine morphofunctional information can be approached by either acquiring images at different time (asynchronous) and fused them through digital image manipulation techniques or simultaneously acquiring images (synchronous) and merging automatically. The asynchronous post-processing solution presents various constraints, mainly conditioned by the different positioning of the patient in the two scans acquired at different times in separate machines. The best solution to achieve consistency in time and space is obtained by the synchronous image acquisition. Nowadays in the clinical scenario are standard combined techniques such as SPECT-CT, PET-CT, PET-MRI.

Furthermore, MRI-Optical imaging has been intensely studied in the last years as an emerging and very powerful technique for combining the functional, structural and morphological information, especially for the cancer treatments.

1.3 Chapter 1 References:

1 Schaming, D. & Remita, H. Nanotechnology: from the ancient time to nowadays. *Foundations of Chemistry* **17**, 187-205, doi:10.1007/s10698-015-9235-y (2015).

2 P., F. R. Vol. 23 22-36 (Engineering and Science, 1960).

3 Taniguchi, N. 18-23 (Proceedings of the International Conference on Production Engineering, 1974).

4 Tersoff, J. & Hamann, D. R. THEORY OF THE SCANNING TUNNELING MICROSCOPE. *Physical Review B* **31**, 805-813, doi:10.1103/PhysRevB.31.805 (1985).

5 Binnig, G., Quate, C. F. & Gerber, C. ATOMIC FORCE MICROSCOPE. *Physical Review Letters* **56**, 930-933, doi:10.1103/PhysRevLett.56.930 (1986).

6 Binnig, G. & Rohrer, H. SCANNING TUNNELING MICROSCOPY. *Ibm Journal of Research and Development* **30**, 355-369 (1986).

7 Jariwala, D., Sangwan, V. K., Lauhon, L. J., Marks, T. J. & Hersam, M. C. Carbon nanomaterials for electronics, optoelectronics, photovoltaics, and sensing. *Chemical Society Reviews* **42**, 2824-2860, doi:10.1039/c2cs35335k (2013).

8 Wu, K., Su, D. Q., Liu, J. M., Saha, R. & Wang, J. P. Magnetic nanoparticles in nanomedicine: a review of recent advances. *Nanotechnology* **30**, doi:10.1088/1361-6528/ab4241 (2019).

9 Bhateria, R. & Singh, R. A review on nanotechnological application of magnetic iron oxides for heavy metal removal. *Journal of Water Process Engineering* **31**, doi:10.1016/j.jwpe.2019.100845 (2019).

10 Wu, Y. J., Chen, C. H., Chang, H. S. W., Chen, W. C. & Chen, J. J. J. in *5th Kuala Lumpur International Conference on Biomedical Engineering (BIOMED 2011).* 380-+ (2011).

11 Jin, X. *et al.* Synthesis and properties of nanocrystal up-converting materials for thin film solar cells. *Acta Physica Sinica* **57**, 4580-4584 (2008).

12 Lu, A. H., Salabas, E. L. & Schuth, F. Magnetic nanoparticles: Synthesis, protection, functionalization, and application. *Angewandte Chemie-International Edition* **46**, 1222-1244, doi:10.1002/anie.200602866 (2007).

13 Whitesides, G. M. Nanoscience, nanotechnology, and chemistry. *Small* **1**, 172-179, doi:10.1002/smll.200400130 (2005).

14 Li, J., Papadopoulos, C. & Xu, J. Nanoelectronics - Growing Y-junction carbon nanotubes. *Nature* **402**, 253-254, doi:10.1038/46214 (1999).

15 Stark, W. J., Stoessel, P. R., Wohlleben, W. & Hafner, A. Industrial applications of nanoparticles. *Chemical Society Reviews* **44**, 5793-5805, doi:10.1039/c4cs00362d (2015).

16 Liu, Y. Y., Miyoshi, H. & Nakamura, M. Nanomedicine for drug delivery and imaging: A promising avenue for cancer therapy and diagnosis using targeted functional nanoparticles. *International Journal of Cancer* **120**, 2527-2537, doi:10.1002/ijc.22709 (2007).

17 Jain, K. K. Nanomedicine: Application of nanobiotechnology in medical practice. *Medical Principles and Practice* **17**, 89-101, doi:10.1159/000112961 (2008).

18 Buzea, C., Pacheco, II & Robbie, K. Nanomaterials and nanoparticles: Sources and toxicity. *Biointerphases* **2**, MR17-MR71, doi:10.1116/1.2815690 (2007).

19 Chauhan, V. P. & Jain, R. K. Strategies for advancing cancer nanomedicine. *Nature Materials* **12**, 958-962, doi:10.1038/nmat3792 (2013).

20 Doane, T. L. & Burda, C. The unique role of nanoparticles in nanomedicine: imaging, drug delivery and therapy. *Chemical Society Reviews* **41**, 2885-2911, doi:10.1039/c2cs15260f (2012).

21 Jain, R. K. & Stylianopoulos, T. Delivering nanomedicine to solid tumors. *Nature Reviews Clinical Oncology* **7**, 653-664, doi:10.1038/nrclinonc.2010.139 (2010).

22 Decuzzi, P. *et al.* Size and shape effects in the biodistribution of intravascularly injected particles. *Journal of Controlled Release* **141**, 320-327, doi:10.1016/j.jconrel.2009.10.014 (2010).

23 Slack, J. D., Kanke, M., Simmons, G. H. & DeLuca, P. P. Acute hemodynamic effects and blood pool kinetics of polystyrene microspheres following intravenous administration. *Journal of pharmaceutical sciences* **70**, 660-664, doi:10.1002/jps.2600700621 (1981).

24 Moghimi, S. M., Hunter, A. C. & Murray, J. C. Nanomedicine: current status and future prospects. *Faseb Journal* **19**, 311-330, doi:10.1096/fj.04-2747rev (2005).

25 Blanco, E., Shen, H. & Ferrari, M. Principles of nanoparticle design for overcoming biological barriers to drug delivery. *Nature Biotechnology* **33**, 941-951, doi:10.1038/nbt.3330 (2015).

26 Nie, S. M. Understanding and overcoming major barriers in cancer nanomedicine. *Nanomedicine* **5**, 523-528, doi:10.2217/nnm.10.23 (2010).

27 Fang, J., Nakamura, H. & Maeda, H. The EPR effect: Unique features of tumor blood vessels for drug delivery, factors involved, and limitations and augmentation of the effect. *Advanced Drug Delivery Reviews* **63**, 136-151, doi:10.1016/j.addr.2010.04.009 (2011).

28 Lin, P. C., Lin, S., Wang, P. C. & Sridhar, R. Techniques for physicochemical characterization of nanomaterials. *Biotechnology Advances* **32**, 711-726, doi:10.1016/j.biotechadv.2013.11.006 (2014).

29 Cho, K., Wang, X., Nie, S., Chen, Z. & Shin, D. M. Therapeutic nanoparticles for drug delivery in cancer. *Clinical Cancer Research* **14**, 1310-1316, doi:10.1158/1078-0432.ccr-07-1441 (2008).

30 Janib, S. M., Moses, A. S. & MacKay, J. A. Imaging and drug delivery using theranostic nanoparticles. *Advanced Drug Delivery Reviews* **62**, 1052-1063, doi:10.1016/j.addr.2010.08.004 (2010).

31 Ma, Y. F., Huang, J., Song, S. J., Chen, H. B. & Zhang, Z. J. Cancer-Targeted Nanotheranostics: Recent Advances and Perspectives. *Small* **12**, 4936-4954, doi:10.1002/smll.201600635 (2016).

32 Wang, R. B., Billone, P. S. & Mullett, W. M. Nanomedicine in Action: An Overview of Cancer Nanomedicine on the Market and in Clinical Trials. *Journal of Nanomaterials*, doi:10.1155/2013/629681 (2013).

33 Astier, A. *et al.* ENHANCEMENT OF ADRIAMYCIN ANTITUMOR-ACTIVITY BY ITS BINDING WITH AN INTRACELLULAR SUSTAINED-RELEASE FORM, POLYMETHACRYLATE NANOSPHERES, IN U-937 CELLS. *Cancer Research* **48**, 1835-1841 (1988).

34 Huang, Z. *et al.* Photodynamic therapy for treatment of solid tumors - Potential and technical challenges. *Technology in Cancer Research & Treatment* **7**, 309-320, doi:10.1177/153303460800700405 (2008).

35 Yang, K. *et al.* In Vitro and In Vivo Near-Infrared Photothermal Therapy of Cancer Using Polypyrrole Organic Nanoparticles. *Advanced Materials* **24**, 5586-5592, doi:10.1002/adma.201202625 (2012).

36 Boisselier, E. & Astruc, D. Gold nanoparticles in nanomedicine: preparations, imaging, diagnostics, therapies and toxicity. *Chemical Society Reviews* **38**, 1759-1782, doi:10.1039/b806051g (2009).

37 Frias, J. C., Ma, Y., Williams, K. J., Fayad, Z. A. & Fisher, E. A. Properties of a versatile nanoparticle platform contrast agent to image and characterize atherosclerotic plaques by magnetic resonance imaging. *Nano Letters* **6**, 2220-2224, doi:10.1021/nl061498r (2006).

38 Xue, S., Qiao, J., Pu, F., Cameron, M. & Yang, J. J. Design of a novel class of protein-based magnetic resonance imaging contrast agents for the molecular imaging of cancer biomarkers. *Wiley Interdisciplinary Reviews-Nanomedicine and Nanobiotechnology* **5**, 163-179, doi:10.1002/wnan.1205 (2013).

39 Lee, N. *et al.* Iron Oxide Based Nanoparticles for Multimodal Imaging and Magnetoresponsive Therapy. *Chemical Reviews* **115**, 10637-10689, doi:10.1021/acs.chemrev.5b00112 (2015).

40 Iagaru, A. *et al.* Simultaneous Whole-Body Time-of-Flight F-18-FDG PET/MRI A Pilot Study Comparing SUVmax With PET/CT and Assessment of MR Image Quality. *Clinical Nuclear Medicine* **40**, 1-8 (2015).

41 Sampath, S. C. *et al.* Detection of Osseous Metastasis by F-18-NaF/F-18-FDG PET/CT Versus CT Alone. *Clinical Nuclear Medicine* **40**, E173-E177 (2015).

42 Blomley, M. J. K., Cooke, J. C., Unger, E. C., Monaghan, M. J. & Cosgrove, D. O. Science, medicine, and the future - Microbubble contrast agents: a new era in ultrasound. *British Medical Journal* **322**, 1222-1225, doi:10.1136/bmj.322.7296.1222 (2001).

1.4 Chapter 1 List of Figure:

Aim of the work

In light of the previously reported state of the art, it is clear that a wide variety of nanosystems are now available to overcome the medical challenges. Their advantages for diagnostic and therapeutic applications are very promising for some of the most challenging human diseases.

In this context, the following thesis project has been focused on the design and synthesis of new nanosystems for diagnostic applications.

Initially, starting from a consolidate microfluidic platform, its implementation has been studied for the production of crosslinked PEGylated nanogels through a one-step synthesis, allowing the production of a biocompatible shuttle for the delivery of active compounds. Hyaluronic acid has been used as a model polymer, while the PEGylation process has been conducted using a polymer that can act also as a crosslinking agent, allowing the simultaneous occurrence of different processes. The obtained nanoparticles, labeled PEG.cHANPs, have been physicochemically characterized and their final properties have been investigated in relation with process parameters involved during the microfluidic synthesis.

In this framework, thanks to the acquired knowledge about the manipulation of this nanopolymer systems, it has been exploited the opportunity to encapsulate one or more different active agents during the unique synthesis step, without a chemical modification of selected active compounds.

The opportunity to develop a safer and more effective probe for diagnostic purpose starting by clinical approved CAs is a significant and valuable challenge.

Gd-DTPA compound has been the first diagnostic agent (for MRI) selected for encapsulation in our nanosystem. The design of Gd-based polymer NPs leads to enhanced relaxometric properties, able to minimize the needed amount of CAs for accurate diagnosis, reducing also side effects. The Hydrodenticity concept summarizes very well this condition explaining the importance of the selection of hydrophilic polymer constrain in nanodomain.

Furthermore, to exploit the versatility of our nanosystems for medical applications, the second loaded-agent in this thesis work has been silica nanoparticles. Differents batch synthesis have been studied and reported to obtain silica nanosystem with defined properties loaded with Gd-DTPA. Then the obtained SiO_2 nanoparticles have been implemented in our microfluidic process combining the inorganic part with the polymers used before in order to produce hybrid nanosystems for enhanced MRI.

In order to use PEG-cHANPs systems in the field of Optical Imaging, the presented polymeric nanosystem has been loaded with Indocyanine Green (ICG), the only dye approved by FDA. In this part of the work, it has been studied not only the possibility of embed ICG within PEG-cHANPs but also the component-interaction in terms of fluorescence stability. Moreover, the electron paramagnetic analysis reveals that this system can be potentially used as a therapeutic agent for photodynamic therapy using the ROS production of ICG under light exposure. Furthermore, in this section, it has studied the possibility of combining simultaneously Gd-DTPA and ICG for obtaining a nanovector for multimodal imaging.

The last part of the thesis presents *in-vitro* cytotoxicity studies of the PEG-cHANPs nanosystem loaded with Gd-DTPA and ATTO 488. First of all, we investigate nanosystem toxicity on different cell lines, with the aim to obtain a more general characterization of biological PEG-cHANPs properties. Different cancer cell lines have been selected for cytotoxicity and cellular interaction studies: Panc-1, human epithelioid carcinoma of pancreatic tissue, A549 cells, human epithelial carcinoma of lung tissue and U87-MG for brain cancer. Moreover, system stability has been investigated in different serums for a better understanding of the nanovector behaviours when the formation of the protein corona occurs. Starting from the obtained results, the possibility to functionalize our NPs with a peptide to create a vector for the Blood-Brain Barrier (BBB) crossing has been investigated.

Chapter 2:

DESIGN OF MICROFLUIDIC PLATFORM TO SYNTHESIZE PEGYLATED HYALURONIC ACID NANOPARTICLES IN ONE STEP SYNTHESIS

In this Chapter, a Hydrodynamic Flow Focusing (HFF) approach is proposed and investigated as a production route to synthesized through a ONE-STEP process pegylated crosslinked Hyaluronic Acid NanoParticles (PEG-cHANPs). Exploiting an HFF approach it is possible to combine simultaneously in the same step the crosslinking reaction of HA and the PEGylation process, with a previous selection of correct materials.

Furthermore, a feasibility study has been conducted to define the principal guidelines for this kind of synthesis. The obtained nanoparticles labeled PEG-cHANPs, have been physicochemically characterized and their final properties have been investigated in relation to process parameters involved during the microfluidic process. Based on results, a set of conditions has been elected as "gold conditions".

2.1 Introduction

Nanosystems can be used as Drug Delivery Systems (DDSs) of active agents and their composition, size, shape, and surface chemistry can be finely modulated to obtain the simultaneous delivery of multiple diagnostic compounds with a significant impact an early and accurate diagnosis[1-3]. Nanocarriers can provide simultaneous visualization of the diseased site through different innovative imaging techniques, enhanced-circulation time for the diagnostic compounds, controlled release kinetics, and superior dose scheduling for improved patient compliance[4]. However, when systemically injected, nanoparticles are immediately sequestered by macrophages because of the opsonization, i.e. the formation of a corona of plasma proteins on the particle surface. This phenomenon implies a reduced blood-circulation time and rapid clearance impairing the reaching of sufficient active agent concentrations at the diseased site. One of the most efficient ways to escape the macrophages capture and the protein corona formation is the covering of the particle surface with a hydrophilic material, such as Polyethylene glycol (PEG). In this way, it is possible to increase particle half-life and reduce the toxicity related to unspecific biodistribution.

In the framework of the principles for the production of nanoparticles, nanoprecipitation-based methodologies open new possibilities regarding particle production, size regulation, active agent encapsulation and offers improvements in batch processes being less complicated and time consuming compared to other production techniques.

Despite these advantages, limits such as high batch-to-batch variations, non-homogenous reaction environment and insufficient production rate reveal the need to move towards techniques providing a higher control in the production of nanosystems with well-defined features.

In this sense, the advent of microfluidics constituted a breaking point. This simple, cost-effective and scalable technology poses as an alternative way to implement consolidate production processes strongly improving their controllability. Indeed, microfluidic-based production offers the possibility of tuning product composition and properties by process parameter adjustments such as flow rate ratio, polymer concentration, pH and temperature. In addition, when microfluidic platforms are used as microreactors, they provide improved space-time yields (product formed per reactor volume and time) producing faster reactions than bulk counterparts. Moreover, the degree of control over local environmental conditions is such to guarantee homogeneous products.

The listed attributes elect microfluidics a “disruptive technology” in tailorable nanovectors production and in the acceleration of their clinical translation.

An efficient implementation of nanoprecipitation for particle production in microfluidics is the hydrodynamic flow focusing (HFF) regimen. Indeed, as reported by Liu et al.[5] the HFF can be used to improve different component mixing and to induce nanoprecipitation. In recent years, the literature showed a great interest in the use of HFF and effective mixing. One of the first examples is presented by Karnik and co-workers[6] who produced poly(lactic-co-glycolic acid)- polyethylene glycol (PLGA-PEG) nanoparticles, studying the effect of the flow-rate ratio on particle size and polydispersity by micellization. Recently, Xu et al. proposed a continuous flow focusing–based strategy to improve the encapsulation efficiency (EE%) of Tamoxifen and Doxorubicin, a hydrophobic and a hydrophilic anticancer drug respectively, in PLGA NPs[7]. In this work, they demonstrated that an improved EE% translates into a more controlled drug release. A homogeneous drug distribution in the particle core is, in fact, able to avoid the initial burst release due to superficial drug distribution.

Starting from a previous study about the possibility to synthesize crosslinked Hyaluronic Acid nanoparticles, in this chapter we investigate the production of PEGylated Hyaluronic Acid NPs in a one-step process, combining thiolated hyaluronic acid (HA-SH) and mPEG-vinylsulfone (PEG-VS). The proposed microfluidic platform enables the simultaneous reaction of the thiol moieties of HA with the vinylsulfone groups of PEG. Indeed, the use of a single step process makes suitable a higher control of particles features and a more homogeneous product. The reduced time of synthesis allows furthermore, an easier translation regarding the scaling up procedure.

2.2 Materials and Methods

Hyaluronate Thiol (HA-SH) with 5 mol % substitution, MW 50 kDa, and mPEG-Vinylsulfone (PEG-VS), MW 2kDa, were purchased from Creative PEGWorks. Ethanol (ACS reagent, (200 proof), absolute; Acetone (puriss. p.a., ACS reagent, reag. ISO, Ph. Eur., ≥ 99.5%); Sodium Hydroxide NaOH (ACS reagent, ≥ 97.0 %, MW 40.00g/mol). Water for synthesis and characterization, was purified by distillation, deionization, and reserve osmosis (Milli-Q Plus; Merck, Darmstadt, Germany).

2.2.1 Rational of the design

HA-based materials have been extensively studied for biomedical applications. In this context also the reaction with PEG play a crucial role in the synthesis route of new biomaterials. For instance, Choi et al.have developed a PEGylated HA-NPs for cancer therapy to overcome the preferential accumulation in the liver of the NPs after systemic administration[8]. Although the PEGylation of HA-NPs slightly affects the binding affinity to the receptor on the cancer cell, PEG on the nanoparticular surface effectively reduces liver uptake and increases the circulation time in the blood, leading to selective accumulation of the nanoparticles to the tumor site. Jin et al. used the PEGylation of thiolated hyaluronic acid (HA-SH) in order to obtain injectable hydrogels with a high potential for cartilage tissue engineering[9]. Instead of making one reaction with the common crosslinker divinyl sulfone (DVS) and subsequently a functionalization reaction with PEG, our idea is to design a single-step synthesis platform. In order to do these, we have chosen a modified PEG with DVS (PEG-VS). The molecular structures of the selected materials are reported in *Figure 2. 1.*

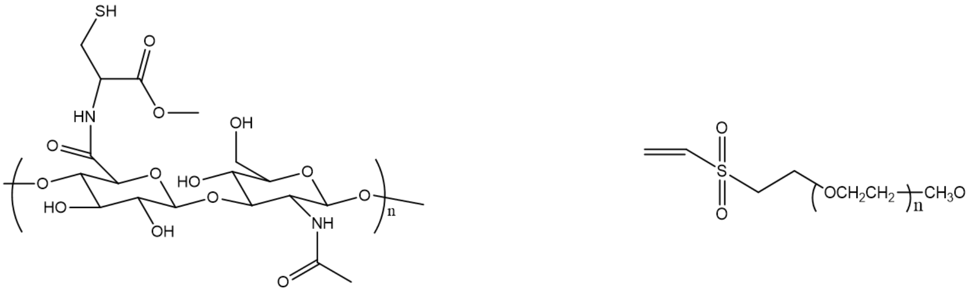

Hyaluronic Acid Thiolated (HA-SH)   mPEG-Vinylsulfone (PEG-VS)

Figure 2. 1 Molecular structures of select polymer: Hyaluronic Acid with a thiol substitution (-SH) of 5% mol and linear PEG with monofunctional vinylsulfone (VS) moieties.

2.2.2 Microfluidics set-up for Flow Focusing (FF) approach

A quartz microfluidic device "Droplet - Junction Chip" (depth x width: 190 µm x 390 µm), purchased from Dolomite Centre Ltd, was used. The internal surface of the channels is coated by a hydrophobic material. On the chip, there are two separate droplet junctions, which can be used in combination. For all the experiments, an X-junction with three inlets and a single outlet channel has been used. The device has a flow-focusing geometry with a 90° angle between the inlets to enhance the diffusion process *Figure 2. 2.a*. It is compatible with Chip interface H for fluidics connections. Three-way isolation ethylene tetrafluoroethylene (ETFE) valves, connected to the syringes and the microfluidic device, make the automatic fill-in of the syringes feasible, thus allowing a continuous dispensing of reagents. The linkage between fluorinated ethylene propylene tubes and the device is carried out through a specially designed connection with polytetrafluoroethylene connectors. The glass syringes (volume 2.5-5 mL) are selected with respect to solvent compatibility and are controlled by a pressure pump (Low Pressure Syringe Pump neMESYS 290N by CETONI). The flow focusing regimen in the microchannel is observed through an optical fluorescence microscope (Olympus IX71) with a 4x scanning objective (*Figure 2. 2.b*).

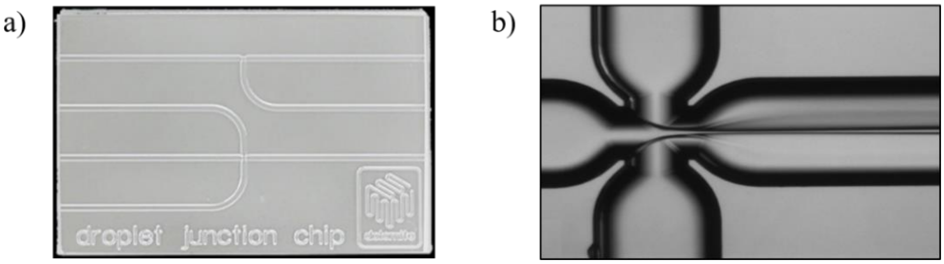

Figure 2. 2: Representation of microfluidic chip used: a) "Droplet Junction Chip 190 µm" with two configurations T- and X- junction, which can be used in combination, b) Optical Fluorescence Microscopy Image of Flow-Focusing pattern (objective 4x)

2.2.3 Synthesis in one-step process of PEGylated Hyaluronic Acid Nanoparticles

Different flow rates were tested and the influence of the flow rate ratio variation on the particle production, size and morphology are determined. For the feasibility study, an aqueous solution of thiolated HA (HA-SH) at a concentration range from 0.01 to 0.5% w/V was tested. The initial solution was kept under continuous stirring for at least 15 min and then PEG-Vinyl sulfone (PEG-VS) (ranging from 0.005 to 0.2 % w/v) was added. This solution is injected in the middle channel with flow rates ranging from 10 μL/min to 40 μL/min; acetone, used as non-solvent, is injected laterally varying flow rates from 90 μL/min to 160 μL/min in order to induce nanoprecipitation in a flow focusing approach. Precipitated NPs are collected in a glass Petri dish containing about 25 mL of non-solvent phase.

In our microfluidic system, a study about the reagent concentration and the influence of the functional group ratio on the nucleophilic addition of the carbanion (HA-SH) to the unsaturated carbonyl compound (PEG-VS) is performed. Each successful experiment is repeated at least ten times.

2.2.4 Purification Recovery and Characterization of Nanoparticles

Purification is performed by dialysis using a solvent gradient across the Spectra Por Cellulose Membrane 6 (Molecular Weight Cut Off, MWCO 50000 Da). A typical procedure consists of loading collected samples into dialysis tubing and keeping the external solution under continuous stirring at 200 rpm to increase the diffusional rate.

It is worth highlighting that all nanoparticles are purified in ethanol to remove partially the unreacted reagents.

The first purification step is in ethanol:

Purify the sample for 1 h in 70% Acetone +30% Ethanol; 1h in 50% Acetone + 50% Ethanol; 1h in 30% Acetone + 70% Ethanol; 2h in 100% Ethanol.

The second purification step is in water:

We purify the sample for 1 h in 70% Ethanol +30% MilliQ water; 1h in 50% Ethanol + 50% MilliQ water; 1h in 30% Ethanol + 70% MilliQ water; 2h in 100% MilliQ water.

Dynamic light scattering (DLS) is used to determine nanoparticle size, polydispersity and superficial charge (Zeta sizer, Malvern UK). The wavelength of the laser is 633 nm and the scattering used is 173°. 1 mL of sample is put in 12 mm square glass cuvettes for 90° sizing (Optical Cuvette, Sarstedt). Zeta potential measurements are also performed at a temperature of 25 °C on a Zetasizer Nano ZS (Malvern, UK), fitted with a high-concentration zeta potential cell. Characterization of the particles morphology and structure is realized through electron microscopy. For TEM analysis (Cryo-TEM TECNAI by FEI) 20 μL of purified sample are dropped on a Carbon Film membrane (Agar scientific) and dried before use. SEM observations (Carl Zeiss Ultraplus Field Emission) are made depositing 200 μL of purified samples on polycarbonate Isopore membrane filters (different cut-offs 0.05, 0.1 and 0.2 μm) through an ultrafiltration vacuum system. On the membrane filter, 7 nm of Au are deposited.

2.2.5 Swelling behaviour of the NPs

The PEG-cHANPs swelling behaviour is studied to indirectly characterize the reaction of occurrence and efficiency. The solution was observed 0, 1, 2, 3, 4, 6 and 8 hours after water dialysis to identify possible variation in size.

2.2.6 Physicochemical Characterization of NPs

The PEG-cHANPs physicochemical behaviour has been studied with spectroscopy measurement. The Fourier transform infrared spectra (FT-IR) were collected from Nicolett 6700 FT-IR spectrometer (Thermo Scientific). All the IR spectra of the specimen were collected at 0.09 cm^{-1} resolution with 2 min interval. Thiolated HA, mPEG-Vinylsulfone and PEGylated cHANPs were analyzed to confirm if the reaction has taken place. Spectra were recorded and analyzed for signal assignation.

Furthermore, the optical properties of the NPs were tested by confocal microscopy (Zeiss LSM 700, Laser Scanning Microscopy with a confocal unit). Different preparation protocols are used to characterize fluorescent NPs. They are observed both in solution, in a Willco-dish glass or on a polycarbonate Isopore membrane.

2.3 Results of the synthesis and discussion of basic phenomena

2.3.1 Set-up of the microfluidic platform process for PEG-cHANPs production

HFF nanoprecipitation is a consolidate method for the production of nanoparticles. The regimen of hydrodynamic flow focusing ensures uniform reaction conditions and particle formation kinetics. A study about the feasibility of the particle production process is conducted to evaluate the effect of the flow rate ratio on the obtaining of the nanoparticle and their properties such as composition, size, shape and superficial charge. Moreover, optimized conditions for the microfluidic translation of the nucleophilic attack reaction are evaluated both in terms of total polymer concentration and of molar ratio between functional groups (SH/VS).

The nanoprecipitation process is implemented in a microfluidic chip with an X-junction configuration ("Droplet - Junction Chip", depth x width: 190 µm x 390 µm) where particle formation occurs by diffusion and nanoprecipitation. The middle channel is injected with an aqueous solution composed of thiolated hyaluronic acid (HA-SH) and polyethylene glycol- vinyl sulfone (PEG-VS); the side channels are injected with pure acetone to provide the extraction of the water phase (*Figure 2. 3*).

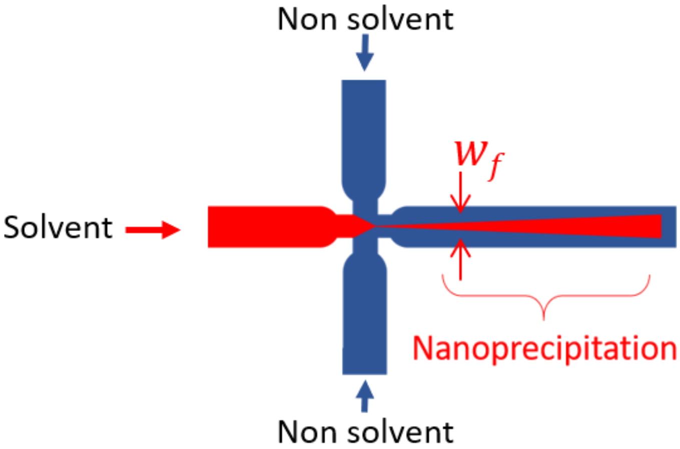

Figure 2. 3: Qualitative Illustration of crosslinking strategies processed in our microfluidic device. W_fr represents the width of the focused stream in HFF regime, a value proportional to mixing time needed. Rapid mixing and nanoprecipitation occur due to diffusion of the solvent out of the focused stream and diffusion of non-solvent into the focused stream.

The production process involves the simultaneous control of many steps. The two different polymers are nanoprecipitated and, in the meanwhile, the Michael addition reaction between thiol groups and vynilsulfone moieties starts to produce at the same time crosslinked and pegylated nanoparticles (*Figure 2. 4*). In batch processes, the only driving force for reaction occurrence and group interaction is thermal motion. In a flow focusing regimen, the middle stream is squeezed by lateral flows to a width related to the flow rate ratio (FR^2), defined as the ratio between the volumetric flow rate of the solvent phase (middle channel) and the non-solvent phase (side channels). Thus, tuning the FR^2, it is possible to reduce the τ_{mix} of the components improving the probability of reaction occurrence. This effect confers to the HFF approach the accurate control over final nanoparticle properties by simple tuning of focused stream width and process parameter adjustment.

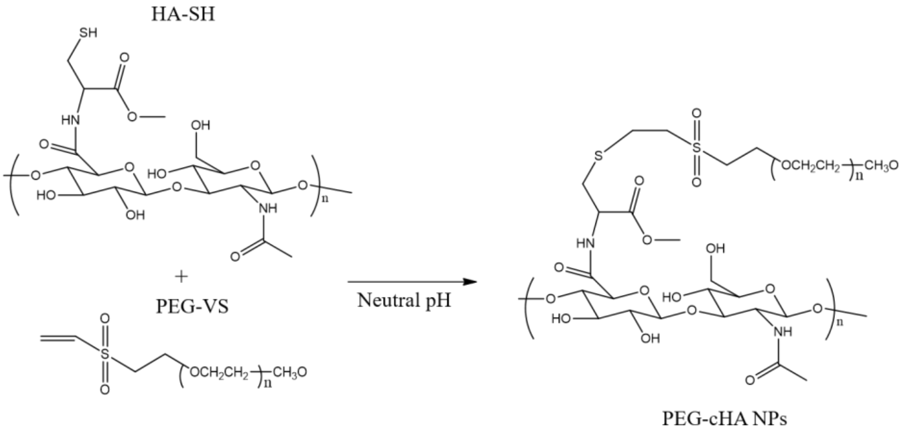

Figure 2. 4: Schematic illustration of the Michael addition reaction mechanism of thiolated HA with PEG-vinylsulfone: nucleophilic addition of a carbanion (HA-SH) to unsaturated carbonyl compound (PEG-VS).

2.3.2 Feasibility study: Flow Rate Ratio effect

In the previous section, we defined the platform set-up in terms of chip geometry and operative parameters. To characterize the resulting particle production, size and morphology, the effect of the Flow Rate Ratio (FR^2) was studied. In our work, different FR^2 values ranging from 0.06 to 0.44 are tested to characterize their influence on nanoprecipitation phases of nucleation and growth. Middle channel flow rates are varied from 10 µL/min to 40 µL/min while side ones from 90 µL/min to 160 µL/min. In order to avoid flow rate fluctuations and to guarantee flux stability, each FR^2 value is tested singularly, without variations during the process. Some combinations could not be explored because of middle channel backflow or massive precipitation. In *Figure 2. 5.a* the variation of particle size in function of FR^2 is shown. All data of Size-Average and standard deviation are obtained by DLS measurements, morphologically analyzed by SEM and plotted fixing the side channel flow rate. Each measurement has been repeated at least three times.

The plot shows that there is an increasing trend of particle size with FR^2 values. Deep in details, we identified three different regions. In the first one, where the FR^2 value is lower than 0.12 and the mean particle size is around 30 nm (*Figure 2. 5.b*). In the second region, FR^2 ranges from 0.12 to 0.27 and the particle size increases from ~250 nm to ~800 nm (*Figure 2. 5.c-d-e-f*). Finally, the third region with FR^2 higher than 0.27 is characterized by massive precipitation. Indeed, in this range, SEM observations show the formation of big aggregates and films of material that compromise the DLS analysis (*Figure 2. 5.g*). This suggests that increasing the FR^2 over a certain limit, the production moves towards a region in which every variation would not produce any effect different from uncontrolled and massive aggregate precipitation.

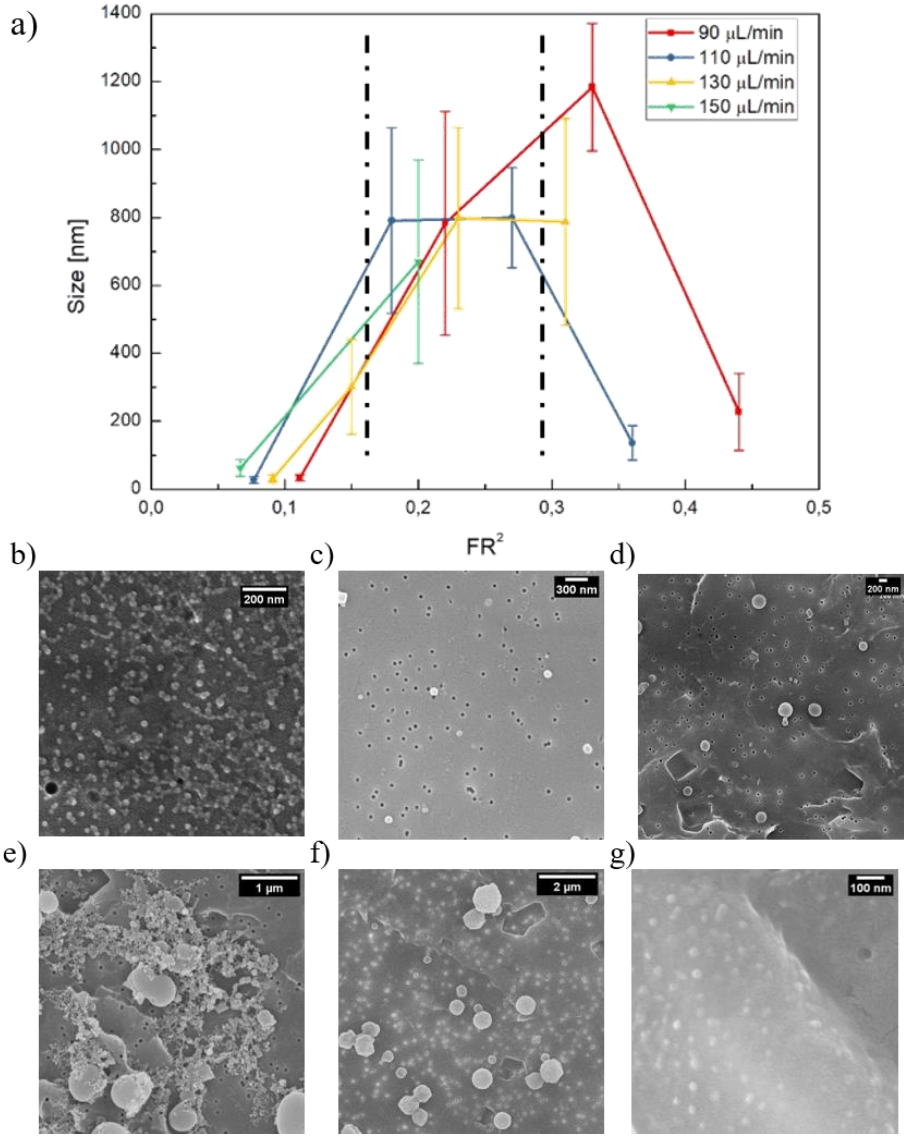

Figure 2. 5: Study flow rate ratio effect: a) plot FR^2 versus nanoparticles size; SEM images presenting variation of particle size and morphology with FR^2: b) First FR^2 region, c-d-e-f) Second FR^2 region, g) Third FR^2 region.

At the same time, moving towards the lowest values of FR^2 there is the production of very small particles that can provide a low loading capability and could be not optimal for our final goal of simultaneous encapsulation of different probes. For these reasons, we selected as Operative-Working Region (OR) for FR^2 the second region where the variation of FR^2 from 0.12 to 0.27 corresponds to a size variation between 250 nm and 800 nm. Moreover, since a FR^2 value of 0.27 (obtained at 30 μL/min – solvent flow rate – and at 110 μL/min – non solvent flow rate) provides a fine and stable flow focusing and absence of precipitates in the mixing channel, it is selected as the "standard condition" and used in the next experiments. In each trial, both HA-SH and PEG-VS are dissolved in water and injected in the middle channel. However, the main need is to guarantee that the Michael addition takes place in the focused stream in a controlled fashion avoiding its premature occurrence in the preparation step or before the reaching of the nozzle. To this purpose, the effect of the temperature on the reaction rate is studied. Two different strategies, Low Temperature (LT) and Room Temperature (RT) are compared. In the first case, the temperature of the injected polymer solution is kept at 4°C both during the preparation step and injection; in the second one, both mixing and processing of the solution occurred at room temperature. For all cases no temperature control on the chip is present. However, we assume that, for the RT strategy, the mixing Temperature in the main channel is constant while for the LT strategy a Temperature gradient moving toward the RT is obtained achieving the favorable conditions for the promotion of the crosslinking reaction. It is worth notice that, also at RT, the solvent solution is processed with no difficulties, meaning that the crosslinking is not completed before injection. However, results show that in this case, a film of material is formed, and the particle formation is impaired. When the temperature is kept at 4°C a uniform population of nanoparticles is obtained (*Figure 2. 6*).

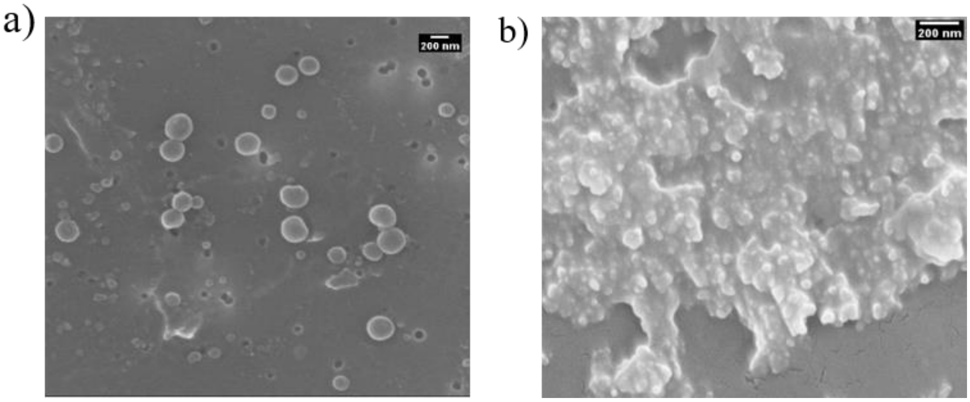

Figure 2. 6: SEM Images represent the influence of temperature on reaction a) Low Temperature (LT), b) room temperature (RT).

These observations reveal that Temperature control is necessary to slow down the reaction rate and to control its occurrence in the device. To study the effect of the Temperature, all trials are conducted in a standard condition of 30 µL/min for the middle channel and 110 µL/min for the side ones.

2.3.3 Effect of collection volume

It is important to select the solvent and the volume where the material, already processed in the microfluidic platform, is collected. The NPs were collected in acetone in order to avoid the re-solubilization of the polymer component. Two collection volumes have been tested: 25 mL (as reported by Russo et al. [10]) and 3mL. The DLS measurements and SEM images show the difference in size due to the changing in the volume of collection. In our system, the nanoprecipitation process is assisted by diffusion and subsequent extraction of the solvent. It is possible to hypothesize that the higher volume the more favourite extraction is, with a reduction of nanoparticles size. Therefore, the best condition in terms of size, shape and morphology is a collection phase of 25 mL of acetone.

2.3.4 Optimization in microfluidic of the Michael addition reaction

A study of the influence of the functional group ratio (defined as the number of thiol groups over the number of vinyl sulfone groups, SH/VS) on particle size and on the crosslinking occurrence, is conducted. Literature data on the SH/VS ratio are reporting a value of 1.2 and a total polymer concentration of 6% w/V as an optimized condition for batch processes.

To make a comparison about the traditional batch processes and the more efficient microfluidic approach and to evaluate the impact of this ratio on the stability of the PEG-cHANPs. a study about the microfluidic implementation of the Michael addition is conducted. At our standard FR^2 value of 0.27, the total polymer concentration is reduced up to 0.23% w/V and significantly smaller values of the functional group ratio are explored. SH/VS value has been varied from 0.0009 to 0.2. The optimized condition is found at SH/VS value of 0.0011 that is three order of magnitude lower than the literature reference. In these conditions, a uniform population of spherical particles with a mean dimension of 140 nm is obtained (*Figure 2. 8.a*). All the other explored values show that the mean particle size increases with increasing SH/VS values (*Figure 2. 7*).

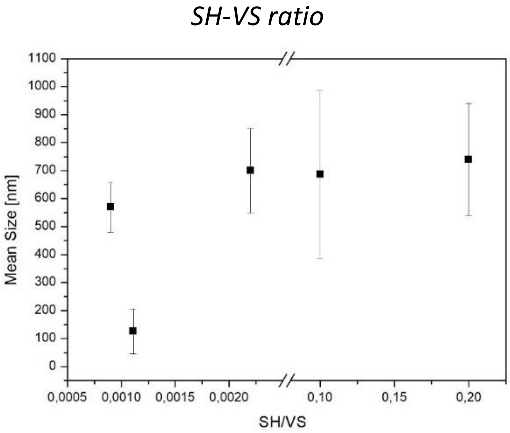

Figure 2. 7: DLS measurement: Particle size and polydispersity variation with SH/VS ratio.

The effectiveness of the crosslinking reaction is indirectly characterized through a study of particle stability in water since in absence of reaction a fast and irreversible swelling of the nanoparticles would be observed. The particle swelling behaviour has been studied for 8 hours through DLS measurements. Data in *Figure 2. 9* show that there is no significative variation in the mean particle size and polydispersity up to 6 hrs, from 6 to 8 hr a slight increase in the size is observed. Particle morphology has been characterized through SEM and TEM (*Figure 2. 8.a-b)*.

The surface charge of these particles is measured through a Z-potential measurement. As expected from the combination of two negatively charged polymers, it reveals a superficial charge of -28 ± 5 mV.

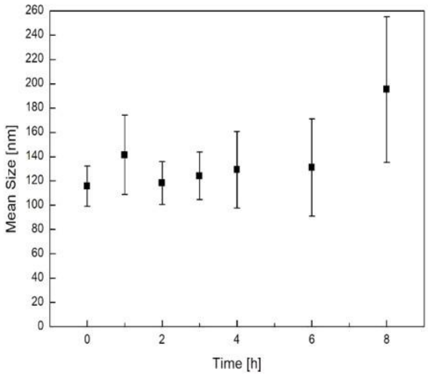

Figure 2. 9 :Swelling behaviour of crosslinked nanoparticles at different time point until 8 hours.

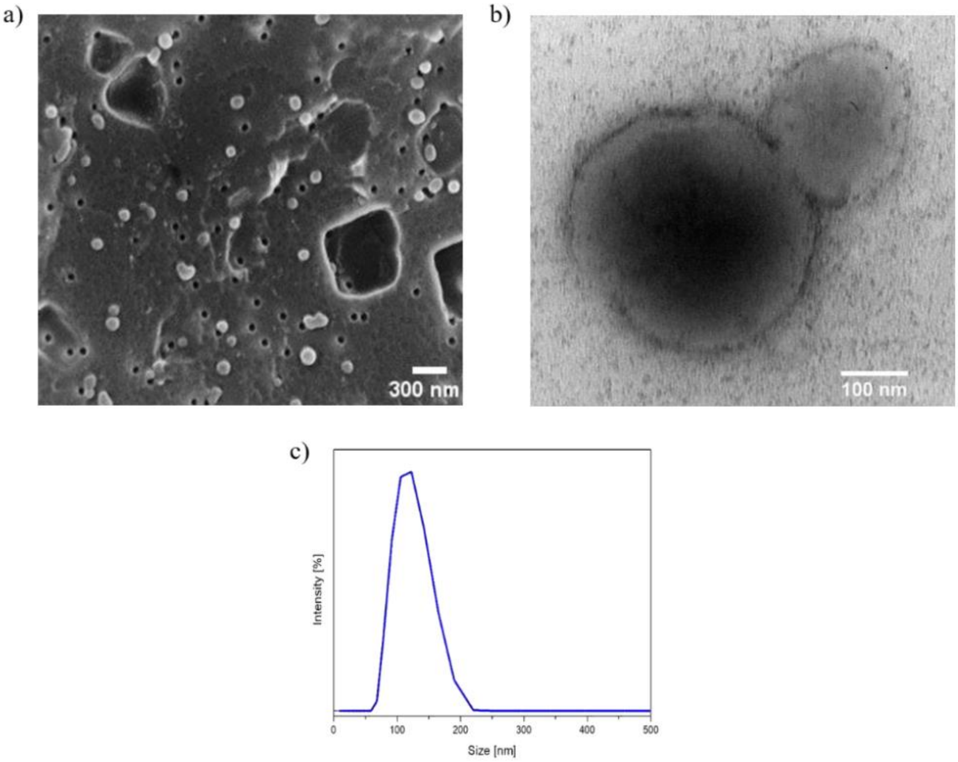

Figure 2. 8 Study of morphological properties of nanoparticles obtained by “gold condition” (a) FE-SEM image of NPs, scale bar 300 nm ; (b) TEM, scale bar 100 nm, image of cross-linked hyaluronic acid nanoparticles with PEG-vynilsulfone in water; (c) DLS profile of cross-linked nanoparticles.

2.3.5 Physicochemical Characterization

FT-IR analysis is performed to confirm the effectiveness of the reaction. Comparative FTIR spectra of HA-SH, PEG-VS and PEGylated cHANPs are showed in *Figure 2. 10*. The analysis shows that the PEGylated cHANPs do not exhibit the double bond C = C, observed for PEG-VS at 750 cm^{-1}, due to the Michael addition reaction between the double bond of the PEGVS and thiol group of HA. Furthermore, the success of the reaction is also guaranteed by the presence of the peak at 600 cm^{-1} that indicates the C-S bond stretching. Nevertheless, results on PEGylated cHANPs also present the peak at 1245 cm^{-1} associated with C-SH vibration related to the residual not reacted thiols of the precursor HA-SH. Further details are reported in Supporting Information. FT-IR analysis finally reports that microfluidic platform to produce PEGylated cHANPs can accurately control the tuning of the crosslinking reaction to improve relaxometric properties and stability of the system.

The optical properties of PEG-cHANPs have been analyzed under confocal microscopy. Indeed, our analysis showed an “auto-fluorescence” behaviour of PEG-cHANPs. When irradiated with a 405nm laser light, the presence of spherical fluorescent spots is detected, without the need of specific dye. However, nanoparticles size cannot be evaluated due to the low spatial resolution of the optical light (*Figure 2. 11*).

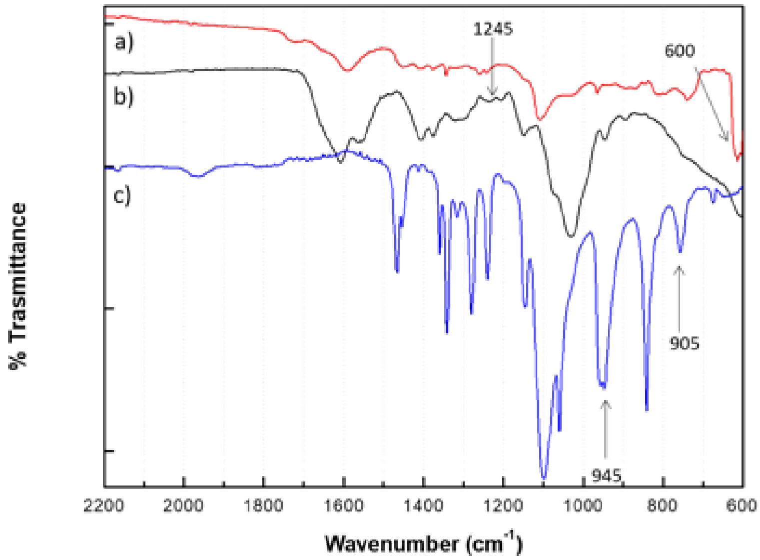

Figure 2. 11: Fourier transform infrared spectra analysis. Comparison of FT-IR spectra of (a) PEGylated cHANPs, (b) HA-SH and (c) PEG-VS precursors.

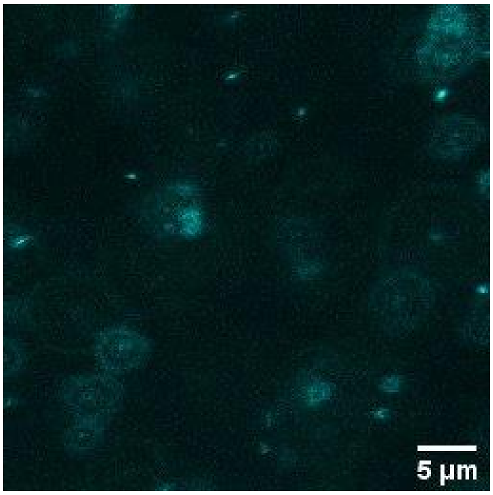

Figure 2. 10: Optical Imaging of “autofluorescence” nanoparticles observed under Confocal Microscopy (λ_{ex}= 405nm, acquisition spectra 430-500 nm), scale bar 5µm.

2.4 Conclusions

Microfluidics is considered a disruptive technology for pharmaceutical manufacturing and is becoming a gold standard in the production of nanoparticles for drug delivery. Here, a ONE-STEP microfluidic synthesis of pegylated crosslinked Hyaluronic Acid NanoParticles (PEG-cHANPs) has been investigated for Multimodal Imaging application. A feasibility study has been conducted exploiting all the process parameters such as FR^2, Temperature and SH/VS ratio. Results have shown the ability of the microfluidic platform to tune the properties and control the size of the particles from 30 nm up to 800 nm. Moreover, it has been proved that the reaction conditions in the microfluidic device are less prohibitive than in a batch mode, indeed, we are able to stabilize the nanoparticles at a SH/VS ratio several orders of magnitude lower than the value reported in the literature. These conditions are able to guarantee particle stability in water.

Our approach has the potential advantage of being able to generate a wider range of slot sizes of hydrogel structure while maintaining monodispersity compared to the similar bulk system. Furthermore, the flexibility of the process enables the tuning of the nanoparticles' size for a specific disease through changes of parameters involved during the process. Nevertheless, the obtained optimization can be furthermore involved in the production of nanosystems with a defined aim.

Furthermore, thanks to PEGylation occurring during the one step synthesis, it is possible to achieve a better stability of possible loaded agents with particular attention in the nanomedicine field.

2.5 Chapter 2 References:

1 Rizvi, S. A. A. & Saleh, A. M. Applications of nanoparticle systems in drug delivery technology. *Saudi Pharmaceutical Journal* **26**, 64-70, doi:10.1016/j.jsps.2017.10.012 (2018).

2 Safari, J. & Zarnegar, Z. Advanced drug delivery systems: Nanotechnology of health design A review. *Journal of Saudi Chemical Society* **18**, 85-99, doi:10.1016/j.jscs.2012.12.009 (2014).

3 Tiwari, G. *et al.* Drug delivery systems: An updated review. *International journal of pharmaceutical investigation* **2**, 2-11, doi:10.4103/2230-973x.96920 (2012).

4 Jain, R. K. & Stylianopoulos, T. Delivering nanomedicine to solid tumors. *Nature Reviews Clinical Oncology* **7**, 653-664, doi:10.1038/nrclinonc.2010.139 (2010).

5 Liu, D. F., Zhang, H. B., Fontana, F., Hirvonen, J. T. & Santos, H. A. Current developments and applications of microfluidic technology toward clinical translation of nanomedicines. *Advanced Drug Delivery Reviews* **128**, 54-83, doi:10.1016/j.addr.2017.08.003 (2018).

6 Karnik, R. *et al.* Microfluidic platform for controlled synthesis of polymeric nanoparticles. *Nano Letters* **8**, 2906-2912, doi:10.1021/nl801736q (2008).

7 Xu, J. *et al.* Controllable Microfluidic Production of Drug-Loaded PLGA Nanoparticles Using Partially Water-Miscible Mixed Solvent Microdroplets as a Precursor. *Scientific Reports* **7**, doi:10.1038/s41598-017-05184-5 (2017).

8 Choi, K. Y. *et al.* PEGylation of hyaluronic acid nanoparticles improves tumor targetability in vivo. *Biomaterials* **32**, 1880-1889, doi:10.1016/j.biomaterials.2010.11.010 (2011).

9 Jin, R. *et al.* Synthesis and characterization of hyaluronic acid-poly(ethylene glycol) hydrogels via Michael addition: An injectable biomaterial for cartilage repair. *Acta Biomaterialia* **6**, 1968-1977, doi:10.1016/j.actbio.2009.12.024 (2010).

10 Russo, M., Bevilacqua, P., Netti, P. A. & Torino, E. A Microfluidic Platform to design crosslinked Hyaluronic Acid Nanoparticles (cHANPs) for enhanced MRI. *Scientific Reports* **6**, doi:10.1038/srep37906 (2016).

2.6 Chapter 2 List of Figures:

Chapter 3:

LOADING CAPABILITIES: ENCAPSULATION OF HYDROPHILIC AND HYDROPHOBIC COMPOUNDS FOR MEDICAL APPLICATION

In this chapter, we firstly investigate the use of PEG-cHANPs as nanovector to encapsulate an active agent for Magnetic Resonance Imaging. The first agent encapsulated was the clinical approved Gd-DTPA, then we moved to study the hybrid system composed by PEG-cHANPs-SiO_2NPs loaded with the same CAs.

Moreover, for the multimodal imaging purpose, we studied the possibility of co-encapsulate simultaneously CAs for MRI and dye for Optical Imaging in PEG-cHANPs matrix. All the results were obtained through the microfluidic platform.

3.1 Gd-DTPA loaded system

3.1.1 Introduction

The Magnetic Resonance Imaging (MRI) represents the first-line diagnostic imaging modality for numerous indications. During the past 30 years, it has emerged as an established technique for preclinical imaging and clinical diagnosis[1,2]. Indeed, MRI enables visualization of tissues at high spatial resolution without using ionizing radiation or invasive procedures[3-7]. Performances of MRI examinations can be improved by using Contrast Agents (CAs), which allow differentiating tissue types that would otherwise be indistinct, overcoming its low sensitivity compared to other imaging techniques[8-10]. MRI Performances of the CAs are well-described by the“ relaxivity”, defined as the rate of change in longitudinal or transverse relaxation times of the water protons per mM concentration of metal ions and determining the enhancement of the image contrast[11].
The presence of the CAs causes a significant increase in the relaxation rate of the water proton nearby paramagnetic ions (such as MnII, FeIII and GdII)[12], thereby adding details to the anatomical resolution[13-20].

In recent times, the rational design of a new class of CAs has been investigated exploiting nanoconstruct opportunities. In particular, polymer-based architecture and their properties can influence the MRI [13,17,21,22] results without chemical modification of the CAs already approved by Food and Drug Administration (FDA).
Among possible construct, crosslinked hydrophilic biopolymers networks (hydrogels) have been investigated because of their biocompatibility,

biodegradability, low immunogenicity, low toxicity, prolonged circulation time [23] and, last but not least, high affinity to water and swelling properties[13-16]. Crosslinked polymers, like nanogels and hydrogels, have high potential to the design of switchable CAs, because an increase of the crosslinking degree can induce relaxivity enhancement by restricting molecular tumbling while maintaining the switching property[24] and allowing facile access of water throughout the structure, which is a key feature in the development of MRI contrast agents[25,26].

In particular, hydrogels[15,16,27,28] show three-dimensional networks, made of hydrophilic polymer chains held together by chemical or physical crosslinking with the ability to swell in water, forming elastic gels that retain a large quantity of fluid in their mesh-like structures[29]. Inside this structure, a favourable aqueous environment for Gadolinium-based CAs, which are the most common clinical used, occurs. In this way the rotational motion of the encapsulated CAs (Gd-DOTP, Gd-DOTA and Gd-DTPA) is restricted and its magnetic properties are amplified The presence of hydrophilic polymer interfaces and the control of water behaviour in hydrogels play a fundamental role in the relaxation enhancement of the Gd CAs by influencing the characteristic correlation times defined by the theory of Solomon and Bloembergen[30].

Courant et al.[22] and Callewaert et al[31]showed that biocompatible hydrophilic hydrogels can be exploited to produce high water content nanoparticles (NPs) encapsulating the metal chelate.

In our research group, we have initially analyzed the impact that hydrophilic biopolymer networks have on the relaxivity of Gd-based CAs and explained the role of the water in the interaction between polymers and metal chelates. This concept, called "*Hydrodenticity*", has been the subject of further investigations as reported by Russo et al. in 2017[32].

In a recent work, we reported an efficient way to produce Hybrid Core-Shell (HyCoS) NPs composed of a Chitosan core and a shell of HA with improved relaxometric properties (up to 5-times than the commercial CAs)[33]. Subsequently, the same nanosystem is used to develop a new nanoprobe for simultaneous Positron Emission Tomography (PET)/MRI acquisitions as reported in our more recent publication[34].

In addition, Russo and co-worker[35] showed that crosslinked Hyaluronic Acid NanoParticles (cHANPs) containing a Gd chelate (Gd-DTPA), are synthesized through a microfluidic platform that allows a high degree of control over particle synthesis, enabling the production of monodisperse particles as small as 35 nm for MRI applications. The relaxivity (r1) achieved with the cHANPs is 12-times higher compared to free Gd-DTPA. Within cHANPs, the properties of *Hydrodenticity* can be modulated to obtain desired mesh size, crosslink density, hydrophilicity and loading capability, as reported by Russo et al[32]. Moreover, they proved that an increase of the crosslinking degree of biopolymer can induce the enhancement of relaxivity by restricting molecular scrambling while maintaining the switching property and allowing easy access of water throughout the structure, which is a key feature in MRI CAs. The possibility to adopt a unique platform to tune the hydrogel structural parameters and, consequently, increase the relaxivity of a metal chelate without any chemical modification, could have a great impact on the clinical outcome. In fact, thanks to their improved relaxometric properties, cHANPs could ensure a brighter contrast with a lower amount of metal chelate, thus enabling the potential reduction of the administration dosage as approved for clinical use.

Nevertheless, the obtained cHANPs, for to not trigger immune system response after intravenous injection, need a post-production functionalization with PEG. Starting from the observation of the Chapter 2 and from the results of Russo works, here we investigate the encapsulation of Gd-DTPA in PEG-cHANPs nanosystem through microfluidics. The gold standard conditions previously defined (*see paragraph 2.3*) have been used to produce in one step-synthesis a nanovector for MRI diagnosis. The influence of metal molecules during the nanoprecipitation process has been evaluated.

3.1.2 Materials and methods

Hyaluronate Thiol (HA-SH) with 5 mol % substitution, MW 50 kDa, and mPEG-Vinylsulfone (PEG-VS), MW 2kDa, were purchased from Creative PEGWorks. Diethylenetriaminepentaacetic acid gadolinium (III) dihydrogen salt hydrate Gd-DTPA (97%), Ethanol (ACS reagent, (200 proof), absolute; Acetone (puriss. p.a., ACS reagent, reag. ISO, Ph. Eur., ≥ 99.5%); Sodium Hydroxide NaOH (ACS reagent, ≥ 97.0 %, MW 40.00g/mol) were purchased from Sigma-Aldrich, Water for synthesis and characterization, was purified by distillation, deionization, and reserve osmosis (Milli-Q Plus; Merck, Darmstadt, Germany).

3.1.2.1 Microfluidic Platform

A quartz microfluidic device "Droplet - Junction Chip" (depth x width: 190 μm x 390 μm), purchased from Dolomite Centre Ltd, was used. On the chip, there are two separate droplet junctions, which can be used in combination. For all the experiments, an X-junction with three inlets and a single outlet channel has been used. The device has a flow-focusing geometry with a 90° angle between the inlets to enhance the diffusion process. The glass syringes (volume 2.5-5 mL) are controlled by a pressure pump (Low Pressure Syringe Pump neMESYS 290N by CETONI). The flow focusing regimen in the microchannel is observed through an optical fluorescence microscope (Olympus IX71) with a 4x scanning objective (*Figure 3. 1*).

3.1.2.3 Preparation of Gd-DTPA loaded crosslinked Pegylated Hyaluronic Acid Nanoparticles (PEG-cHANPs-Gd)

As already presented in the previous chapter, literature studies report that the chemical reaction between thiols moiety of HA and Divynil sulfone groups on PEG chains was performed at neutral pH values and 37°C. In our microfluidic system, a study on the reagents was conducted to create, at the nozzle section, sulfonyl bis-ethyl linkages between the hydroxyl groups of the polymer chains forming nanoparticles. Gd-DTPA (0,1% wt/v) was added to the HA-SH aqueous solution and stirring for 15 min at room temperature. Then the solution was cooled at low temperature and mixed with the crosslinker PEG-VS. The obtained solution was injected in the middle channel with a flow rate of 30 μl/min while the non-solvent phases were fluxed at 110 μl/min.

In our system, the occurrence of the solvent extraction, by acetone phase, produces the dilution of water into the mainstream, slightly increasing the reaction time. The obtained NPs were collected in 25 mL of acetone in a petri dish and after moved to a vial and left on a wheel overnight in stirring, to ensure the crosslinking reaction. To stop it and remove the unreacted materials several dialysis steps have been conducted (*See paragraph 2.2.4*).

3.1.2.4 In vitro T1

In vitro MR has been realized both on empty and on loaded NPs and results were compared to the control water solutions at a known concentration of Gd-DTPA. After vigorous stirring, 300 µl of the sample was put in glass tubes and changes in relaxation time (T1) were evaluated at 1.5 Tesla by Minispec Bench Top Relaxometer (Bruker Corporation). The relaxation time distribution is obtained by a CONTIN Algorithm and the relaxation spectrum is normalized by its processing parameters. The integral of a peak corresponds to the contribution of the species exhibiting this peculiar relaxation to the relaxation time spectrum. Experiments were repeated at least ten times.

3.1.2.5 Inductively Coupled Plasma (ICP-MS)

The loading capability of Gd-DTPA is calculated by Inductively Coupled Plasma (ICP-MS, NexION 350, Perkin Elmer) measurements. All data are collected and processed using the Syngistix Nano Application Module. Gd-DTPA is measured at m/z 157 using a 100 µs dwell time with no settling time. For all data, purified NPs suspension were used.

3.1.2.6 Rheologycal data

In the perspective of processed the material in a microfluidic platform, the rheological properties of the polymeric solution represent a critical factor for the flow properties. Rheological measurements are performed on a HAAKE MARS Rheometers (ThermoFischer Scientific) using a plate-plate geometry (P35/Ti). The volume used for each measurement was 1mL, with a gap between plates of 1mm. Three sets of samples of HA-SH in water, HA-SH plus Gd-DTPA and HA-SH with PEG-VS plus Gd-DTPA (for all the set the HA-SH concentration ranging from 0,1 to 2%w/v) have been investigated using 1mL at room temperature.

3.1.2.7 Small Angle Neutron Scattering (SANS)

SANS measurements were performed at 25 °C with the KWS-2 diffractometer operated by Julich Centre for Neutron Science at the FRMII source located at the Heinz Maier Leibnitz Centre, Garching (Germany). Neutron scattering analyses have been conducted on empty PEG-cHANPs and PEG-cHANPs-Gd. For all the samples, neutrons with a wavelength of 5 Å and $\Delta\lambda/\lambda \leq 0.2$ were used and the scattering intensity *I(q)* was collected in the range of the modulus of the scattering vector $q = 4\pi n\, sin(\theta/2)/\lambda$, between 0.0001 $Å^{-1}$ and 0.02 $Å^{-1}$, where λ and θ represent the wavelength of the neutron beam and scattering angle respectively.

3.1.3 Result and discussion

As presented in *Chapter 2*, in the flow focused nanoprecipitation, the non solvent phase, flowing through two side channels, focuses the solvent phase in the main channel inducing the mutual diffusion of all solvents and promoting the precipitation of the solute and, therefore, the production of PEG-cHANPs. The value of FR^2 of 0.27 (obtained at 30 μL/min -solvent flow rate – and 110 μL/min – non-solvent flow rates) with HA-SH and PEG-VS of 0.05% wt/v and 0,18% wt/v respectively, are considered as “standard process conditions” for all the experiments.

Previous optimizations led to the definition of the following conditions as standard conditions for the particle production: T = 4°C, FR2 = 0.27 and SH/VS = 0.0011.

Starting from these conditions, the encapsulation of Gd-DTPA was conducted and tested to provide diagnostic properties of the nanovectors. Briefly, the payload agent was dissolved in the polymer solution before the injection. Later, the nanoprecipitation occurs in the mixing channel producing the encapsulation of the compound (*Figure 3. 1 a*). We have observed that the presence of this agent is not significantly influencing the stability of the flow focusing in the microfluidic device even if higher precipitation at the interface between the solvent and the non-solvent phase in the mixing channel has been visually observed through optical microscopy (*Figure 3. 1 b*).

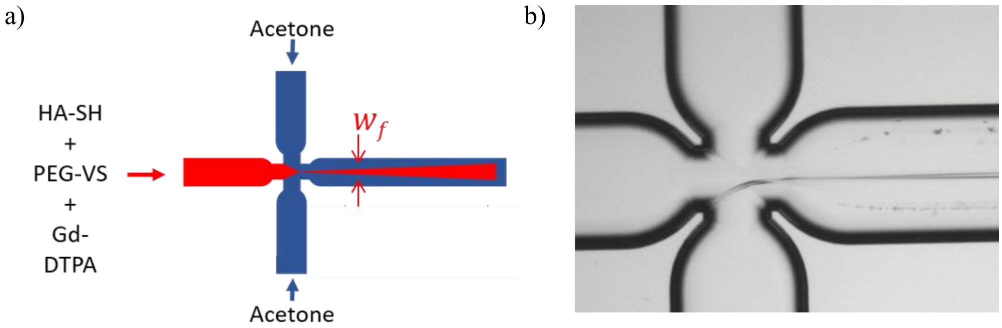

Figure 3. 1:a) Schematic Illustration of crosslinking strategies processed in our microfluidic device; b) Optical Fluorescence Microscopy Image of Flow-Focusing pattern.

In *Figure 3. 2* were reported SEM and DLS analyses that show mean size at 150 ± 25 nm, slightly higher compared to empty PEG-cHANPs (*See chapter 2.3*).

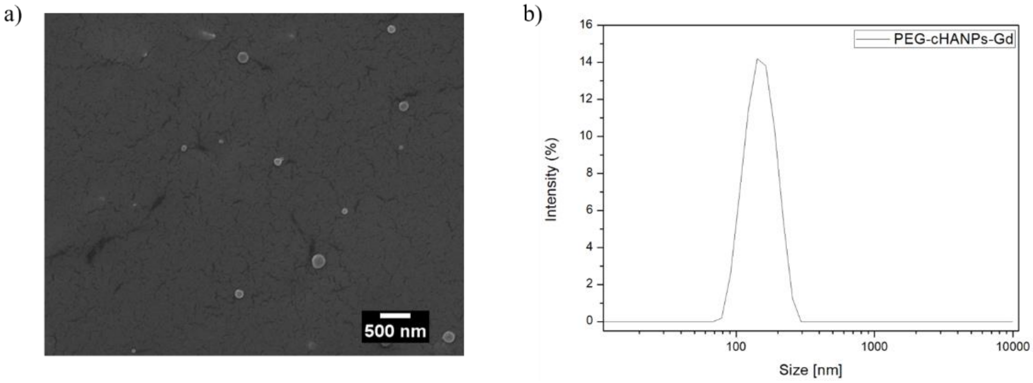

Figure 3. 2 Morphological Characterization of Gd-DTPA loaded nanoparticles. a) SEM image and b) DLS measurement in distilled water.

ICP-MS analyses have been used to quantify the amount of Gd-DTPA entrapped in nanoparticles. Gd-loaded PEG-cHANPs exhibit a loading capability (LC) of 60%.

In-vitro longitudinal relaxation time T1 evaluation is performed for pure water as sample control, empty PEG-cHANPs and PEG-cHANPs loaded with Gd-DTPA. The longitudinal relaxation time T1 is measured at 37°C and at 1.5 T. Each measurement shows a reduced mean T1 value with respect to pure water *Figure 3. 3*.

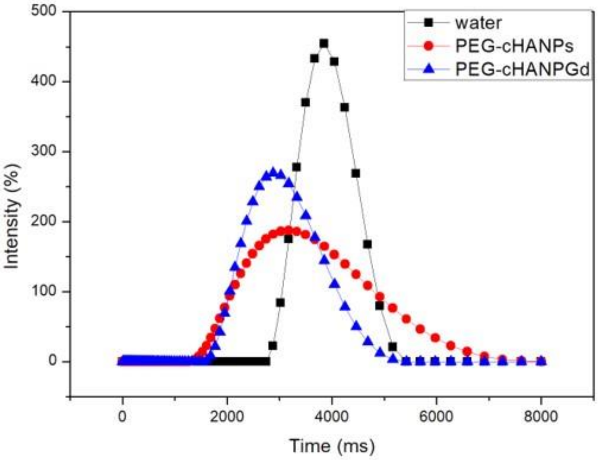

Figure 3. 3: In vitro MR. Comparison of longitudinal relaxation time distributions of water (-■-), empty PEG-cHANPs suspension (-●-), PEG-cHANPs loaded with Gd-DTPA (-▲-);

Moreover, the relaxation time of free Gd-DTPA at different molar concentrations is measured to compare this value to the relaxation time obtained from different nanoparticle formulations. The calibration curve for the free Gd-TPA solution is reported in *Figure 3. 4*.

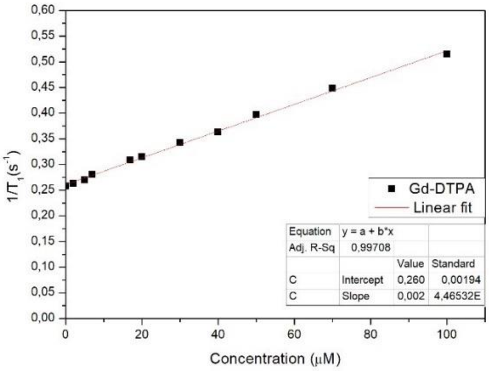

Equation	y = a + b*x		
Adj. R-Sq	0,99708		
		Value	Standard
C	Intercept	0,260	0,00194
C	Slope	0,002	4,46532E

Figure 3. 4: Calibration Curve of relaxivityfrom Minispec Measurement for free Gd-DTPA in water at different concentrations.

The comparison reveals that T1 = 1640 ms associated to Gd loaded PEG-cHANPs corresponds to an equivalent free-Gd-DTPA content of 135 μM, a value slightly higher than the effective concentration inside our nanosystems (110 μM by ICP-MS measurement), anyway 1.22 times higher than the free Gd-DTPA at the same concentration. Gd loaded PEG-cHANPs confirm the boosting of the Relaxometric properties of the metal chelate and, therefore, also this new formulation is preserving the effect of Hydrodenticity.

From the graphs reported in *Figure 3. 5* and *Figure 3. 6* it was possible to note that the viscosity of HA-SH solution in MilliQ water, with concentration ranging from 0,1 to 2% wt/v, is dependent by concentration itself. Adding Gd-DTPA, at final concentration 1mM, to these solutions, the viscosity of all concentration decrease. This is probably due to the presence of hydroxide groups that act as plasticizer. The same behaviour was observed when the systems were loaded with PEG-VS. The decreasing viscosity is a key point that allows us to have a better processability through a microfluidic platform.

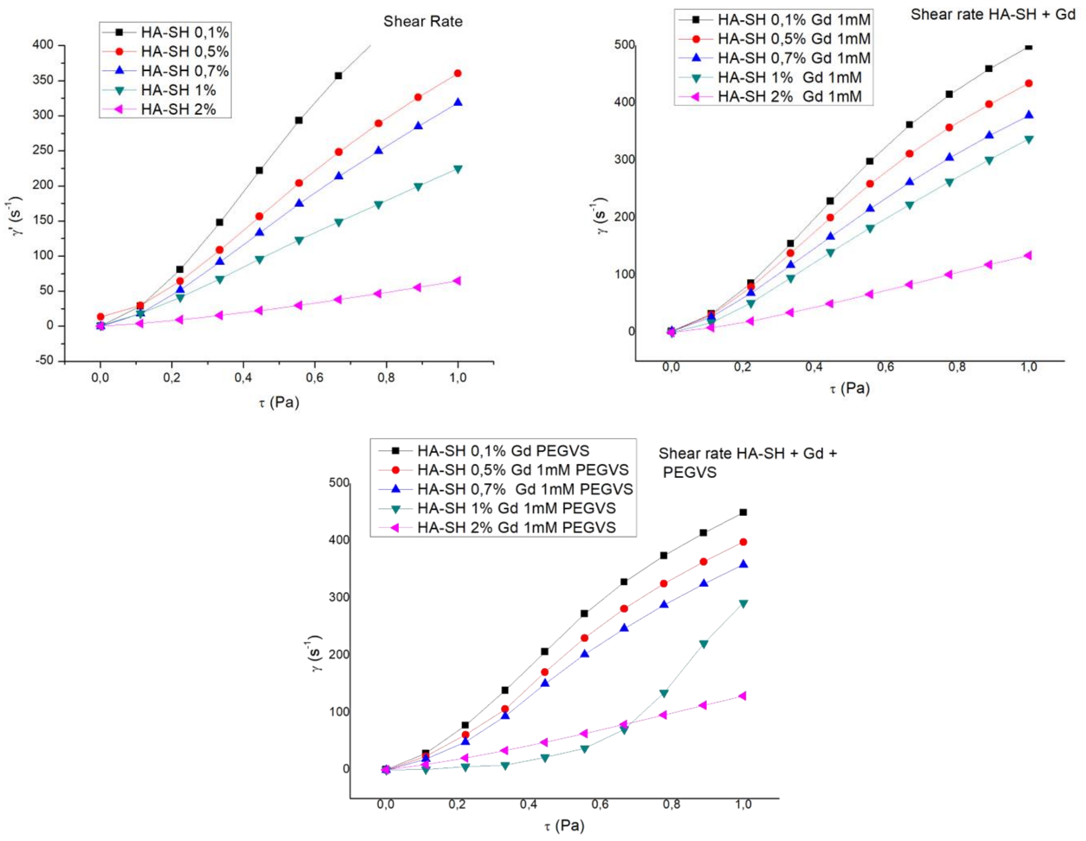

Figure 3. 5: Rheological data obtained by measurements of the shear rate behaviour on HA-SH solution, concentration from 0,1 to 2%wt/v, with 1mM of Gd-DTPA and 0,18%wt/v of PEG-VS.

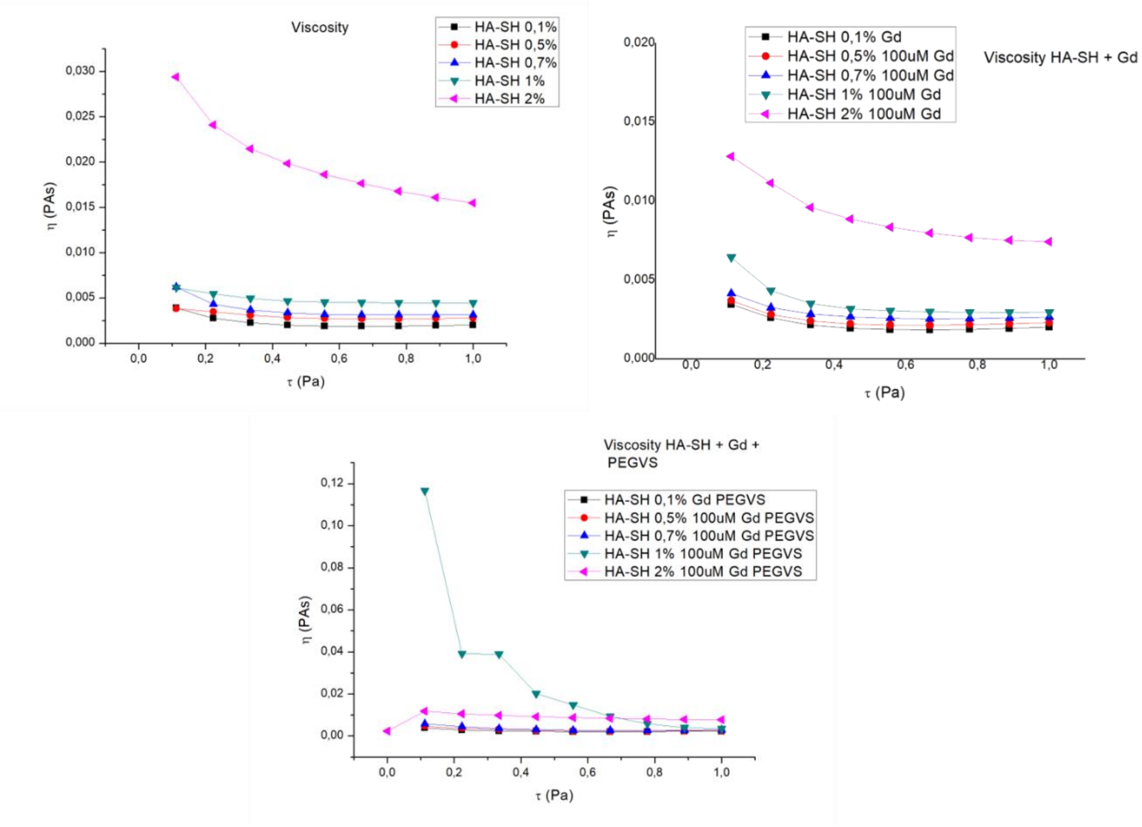

Figure 3. 6: Rheological data obtained by measurements of viscosity of HA-SH solution, concentration from 0,1 to 2%wt/v, with 1mM of Gd-DTPA and 0,18%wt/v of PEG-VS.

In *Figure 3. 7* was reported the scattering cross section pattern dΣ/dΩ for the two samples analyzed. The quantitative analysis of SANS data required the identification of a suitable model to describe the scattered intensity vs *q* (scattering vector) and to extract structural information on the sample. Accordingly, the SANS profiles of all samples have been fitted by using the Guinier-Porod model that is used to determine the size and dimensionality of scattering objects, including asymmetric objects such as rods or platelets, and shapes intermediate between spheres and rods or between rods and platelets.

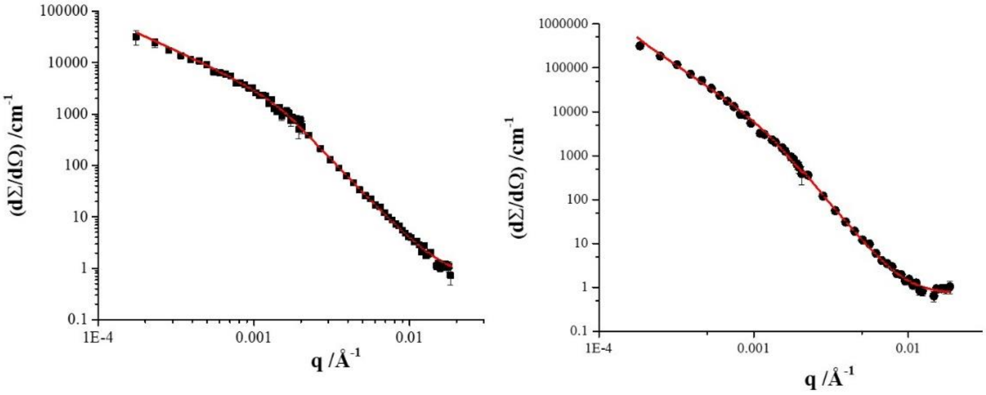

Figure 3. 7: SANS measurement: At left it was showed the data obtained from sample PEG-cHANPs-empty and fitted with the Guinier-Porod model, at right the same model has been used to fit the sample PEG-cHANPs-Gd.

From the applied Guinier-Porod model the gyration radius calculated for the sample was reported in *Table 3. 1*. It was possible to observe that the presence of Gd-DTPA within the polymeric matrix influences the final size reducing the Rg value. This leads us to assume that polymeric meshes were more closed to each other due to Gd-DTPA structure.

Table 3. 1: Gyration radius calculated by Guiner-Porod methods for PEG-cHANPs systems empty and loaded with Gd-DTPA:

	Rg (gyration radius) /Å
PEG-cHANPs empty	630 ± 21
PEG-cHANPs-Gd	536 ± 10

3.2 Hybrid systems with SiO_2

3.2.1 Introduction

Recent advancements in imaging diagnostics have been focused on the use of engineered nanostructures that entrap Magnetic Resonance Imaging (MRI) Contrast Agents (CAs), without chemically modifying the clinically approved compounds and which are able to increase the too poor relaxivity of commercial CA. Port et al. have reported that the rigidification of MRI CAs, obtained through covalent or noncovalent binding to macromolecules, could increase the relaxivity of the metal-chelate[17]. Decuzzi et al. have proved that it is possible to modify the relaxometric properties of MRI CAs through the geometrical confinement by controlling their characteristic correlation times without the chemical modification of the chelate structure. Another tentative approach to increase the relaxivity was attempted by Courant et al by adding the Gd-DOTA to a Polymer matrix[22].

In this perspective, our research group has exploited the impact of crosslinked and un-crosslinked biopolymer matrices on relaxometric properties of Gd-DTPA where the contribution to the enhancement of CAs is highlighted and attributed to the reduced mobility of water within the hydrogel network. The presence of hydrophilic polymer interfaces and the control of water behaviour in hydrogels play a fundamental role in the relaxation enhancement of the Gd CAs by influencing the characteristic correlation times defined by the theory of Solomon and Bloembergen[30]. The presence of nanocompartments due to polymeric network acts as an attractive region for water molecules that could enhance the hydration of contrast agent ion. The interaction between elastic stretches of the polymer chain, hydration degree of Gd-CAs and water osmotic pressure forms a complex equilibrium that we have called Hydrodenticity[35,36].

Hydrodenticity, hence, refers to the status of the hydrated Gd-DTPA with the coordination water molecules subjected to osmotic pressure deriving from elastodynamics equilibrium of swollen gels. We hypothesize that the achievement of this equilibrium is reached when the normal morphology of the meshes and its energetic stability is compromised by the presence of the Gd-DTPA and evolves to a new spontaneous equilibrium involving the formation of nanocompartments in which water is in an abnormal aggregate state that influences the relaxivity.

A high relaxivity can be achieved by fine and accurate control of the characteristic parameters, such as the number of water molecules in the coordination sites of the Gd ion, their diffusion nearby the metal complex and the rotational correlation time of metal complex, that regulate the dipolar interaction between water protons and Gd-based CAs[37].

In order to modulate the hydrogel properties, we have successfully used a microfluidic strategy. Applying this approach we have synthesized as first Gd-DTPA-loaded crosslinked hyaluronic acid nanoparticles (cHANPs) and after we have implemented the process to reach PEGylated- cHANPs in one step manner[35,36].

Modulation of crosslink density, mesh size, hydrophilicity and loading capability, through microfluidic approach, reflect on Hydrodenticity properties. Nanoparticles with a mean particle size as low as 35nm are obtained without the chemical modification of the clinically approved chelate, achieving a signal intensity in r1 (where r1 is the longitudinal relaxivity component) 12- times larger than that of the commercial MRI CA, Magnevist, at the magnetic field used in clinical MRI, 1.5 Tesla; while in the case of Gd-loaded PEG-cHANPs we have a mean particles size of 150nm and an r1 signal intensity of 5 times higher.

Furthermore, the possibility for both cHANPs and PEG-cHANPs, to co-encapsulate several dyes simultaneously with Gd-DTPA make these nanostructures highly desirable as nanocarriers for multimodal diagnosis.

The use of microfluidic devices for nanoparticle synthesis is advantageous in many aspects, including enhanced processing accuracy and efficiency. Compared with conventional nanoprecipitation batch methods, advantages of microfluidic systems lay in their excellent ability to manipulate nanoliter flows. The fast and efficient mixing provides different physicochemical properties of NPs, controlling the ratio of flow rates of the non-solvent to the solvent solution or by changing the configuration of the micromixer. It usually results in the production of smaller particles compared to conventional methods[38-40].

Future outlooks are addressed to the ability to build more complex nanostructures exploiting the Hydrodenticity effect due to the combination of different hydrophilic materials. In this scenario, the interaction of polymer matrix and silica nanostructure can be very intriguing to investigate for a depth understanding of relaxivity properties of Gd-based CA.

Indeed, even though a literature data regarding Gd-loaded silica structure exists, the main principles and the opportunity to take advantage by the microfluidic is still missing. For example, different sizes (diameter 25, 50 and 60 ± 5nm) of silica NPs containing water-accessible GdIII complex (not clinically approved Gd-ebpatcn) have been synthesized by Wartenberg's group[41]. Their results show a very high value of relaxivity r1 of CA-loaded complexes, larger than those of free complex. Zhou et al[42]. had synthesized mesoporous silica nanoparticles loaded with Gadopentic-acid (Gd-DTPA).

Other interesting research shows the possibility to combine in mesoporous silica CA for MRI and dye for optical imaging. Sharma et al.[43] presented a novel pathway for encapsulating Indocyanine Green (ICG), in a biocompatible silica matrix with an outer silane coating for chelating GdIII. This work proves an enhancement of optical stability of ICG and relaxivity values higher than commercially available contrast agent ones.

The combination of silica NPs with superparamagnetic metal oxide as a negative MR contrast agent has been intensively investigated[42-48]. However, the combination of silica with Gd(III) compounds (T1 contrast agents) requires further exploration.

In this section, we analyze and compare different synthetic procedures in order to obtain silica nanoparticles loaded with Gd-DTPA.

Firstly, we investigated the possibility to load Gd-DTPA within amino-functionalized Mesoporous Silica (MSP) particles obtained by a modified Stober method[49].

Actually, this time-consuming protocol, exploit that electrostatical interaction between negatively charged CAs structure and superficial positive charge of the amino group of MSP occurs. Afterward, we focused our interest in one-step synthesis able to load directly the drug in the silica nanoparticles. Starting from results reported in literature several strategies have been investigated varying the emulsion method (direct or indirect) and the ratio between the phases involved during the hydrolysis and condensation process for silica production. At least a novel strategy to obtain positively charged Silica NPs has investigated.

3.2.2 Materials and Methods

Tetraethyl orthosilicate (TEOS), (3-Aminopropyl)triethoxysilane (APTES), Ammonia Solution in water (28-30%), Cetyltrimethylammonium bromide (CTAB), Tween 80, Cyclo Hexane, triethanolamine (TEA), toluene and 1-hexanol were purchased by Sigma Aldrich and used without further purification. Triton x-100 (bio grade). Water for synthesis and characterization was purified by distillation, deionization, and reserve osmosis (Milli Q).

3.2.2.1 Synthesis Procedure

- *Synthesis of mesoporous silica nanoparticles (NPs1OT)*

Synthesis procedure for mesoporous silica nanoparticles (MSP) has been conducted as described by Pan et al.[50] with slight modification1. Basically, 2 g CTAB (5,48 mmol) and 0,08 g of TEA (796 nmol) were dissolved in 20 mL of distilled Milli-Q H2O for one hour at 95°C. After that 1,5mL TEOS (6,76 mmol) was added dropwise and left to react for one hour. The reaction mixture was interrupted by adding 30mL of EtOH and then additionally stirred for another hour. The resulted nanoparticles were then cooled down at room temperature and centrifuged (3 times in EtOH at 35 krcf for 20 min at 17°C, 1 time in water 40krcf for 10 min at 17°C) before drying under vacuum. The material, denoted as NPs 1OT, was characterized by: SEM, TEM, FTIR, TGA, DLS, ζ-potential and N2 adsorption (BET analysis).

- *Post synthetic amino groups loading (Amino-MSP):*

MSP was functionalized with amino groups, in order to create a possible point of linkage with Gd-DTPA. The procedure for the loading was the following: 27 mg of dried NPs (white powder) were dispersed in a mixture, containing 10,8 mL of Toluene, 6,75 μL APTES and 5,75 μL of TEA. The final mixture was stirred and refluxed at 60° over-night. After the occurrence of the reaction, amino-functionalized NPs were obtained by centrifugation, washed three times in Milli-Q water at 35krfc for 20 minutes at 17°C and dried under vacuum for further use.

- *Impregnation Protocol with Gd-DTPA:*

The obtained nanoparticles were impregnated with Gd-DTPA. The procedure was reported as following: 4 mg of nanoparticles were dispersed in 0,200mL of solvent (in our case water), with 4mg of the compound (Gd-DTPA) and left under mechanical stirring overnight. After the impregnation occurrence, the solution was cleaning several times with water.

- *One-step Synthesis of MSN loaded with Gadopentetic acid (NPs 3-4OT)*

The synthesis used for this section, with some slight modification, has been described by Zhou et al.[42] Briefly 1,77 mL of Triton X-100 (3mmol) was dissolved in a solution of 1,8 mL 1-hexanol and 7,5 mL of Cyclohexane and stirred at room temperature for 30 min. Next 2 mL of an aqueous solution of Gd-DTPA (30mg/mL) was added to the solution and stirred for other 30 min. Then 100 μL of TEOS (0,4mmol) was added dropwise. The hydrolysis of TEOS was initiated by the addition of 1,5 mL of Ammonia solution (28-30%) that act as a basic catalyst. The reaction was stirred at room temperature for 6 hours. At least 4 mL of Acetone were added for demulsification and to stop the reaction. The obtained mixture was then centrifugated and washed three times with ethanol and three times with water (at 35 krcf for 20 min at 17°C). The produced NPs, called NPs3OT, were dried under vacuum overnight and then stored for further characterization. Since for this protocol the reaction yield was really low, another synthesis protocol has been tested. The methodology adopted was the same, the reverse emulsion method, but in this case, the gadolinium solution was added directly in the first mixture and Ethanol was used as demulsification agent instead of acetone. Briefly, 5,31 g of Triton X-100 (8,7mmol) was dissolved in a solution containing 4,8 mL of n-hexanol, 23,1 mL of cyclohexane and 1,14 mL of Gd-DTPA aqueous solution (1mg/mL), in a round-bottom flask and stirred on a magnetic plate for 15 min. Then 150 µL of TEOS (0,6mmol) was added to the mixture and stirred for 30 min followed by the addition of 300 µL of ammonia solution (28-30%wt). The mixture was stirring at room temperature for 6 hours. After that 50 mL of Ethanol was added in the flask to destabilize the microemulsion and stirred for 30 min. The obtained suspension was centrifuged for 30 min at 17°C at 35000 rcf. After removing the supernatant, about 2 mL of Ethanol were added in both tubes, sonicated and put into Efferndorf tube. The obtained material, called NPs4OT, was centrifugated and washed several times (for 30 min at 14500 rpm) in Ethanol and in water before left to be dried under vacuum overnight. Also, for this procedure, the reaction yield was very low.

• *Synthesis of MSP loaded with Gadopentetic acid by a direct microemulsion method (T-MSP)*

Protocol by Maqbool et al. [48]. Briefly 10 µL Tween 80 was added to 8 mL of ammonia solution (28-30 %) in a 50 mL capacity round bottom (RB) flask and stirred at 400 rpm at room temperature for 5 min. Then 1.28 mL of Ethanol and 1 mL of distilled water were added to it under 380 rpm stirring rate. The ratio of ammonia solution and ethanol was 1:0.16 v/v. This surfactant solution was then transferred to a pre-heated oil bath (maintained at 50 ºC) and stirred at 380 rpm for 30 min. After warming the surfactant solution, 0.8 mL TEOS (3mmol) was added to it dropwise for over 2 minutes under vigorous stirring (~ 1000 rpm). After about a minute, turbidity appeared in the precursor solution. The precursor solution was stirred at 50 ºC with 1000 rpm stirring rate for 2 hours. The magnetic bead was removed from the obtained white reaction mixture and the opening of RB flask was covered by perforated aluminium foil with many pores punctured by needle. This RB was then kept in a oil bath at 50 ºC for 20 h under the hood to evaporate ethanol from the solvent mixture. The obtained concentrated white sol was recovered in an Eppendorf tube and subjected to centrifugation at 12000x g for 10 minutes at 25 ºC. The process of centrifugation and re-dispersion was repeatedly carried out initially three times in distilled water and finally two times in ethanol for purification. The obtained compound was dried under to hood to obtain a fine powdery white product. This product was labeled as T-MSN. One variant of the material was prepared by changing the amount of water added to the solution (with or without Gd-DTPA) keeping other synthetic details unchanged.

- *Synthesis of positively charge MSP loaded with Gadopentetic acid (AT-MSP)*

For this part of the work, we decided to investigate as a possible synthesis procedure for silica loaded nanoparticles, the one in which the silica precursor was represented by two sources: the TEOS and the APTES. Indeed, their combination influenced particles size and also the presence of APTES modified the ζ-potential of the obtained nanosystems[51]. The synthesis procedure was the same as reported in the previous paragraph with the only change in silica precoursor. After warming the ammonia solution containing Tween 80 and Gd-DTPA, the two silica sources were added dropwise under vigorous stirring (TEOS 420 µL (1,8mmol) and APTES 380 µL (2mmol), without premixing). The solution was processed as reported before. The collected materials have been denoted as AT-MSP.

3.2.2.2 Implementation in microfluidic

The silica nanosystems described before were also implemented by a microfluidic process. A solution containing pre-synthesized SiO_2 NPs (concentration 100µg/mL) was added to a polymeric solution (composed by HA-SH 0,05%wt/v and Gd-DTPA 0,1% wt/v) and stirred on wheel to promote an adequate mixing of the component (3 days at room temperature). After that, the solution was cooled at low temperature (4°C) and mixed with the crosslinking agent (PEG-VS 0,18%wt/v) for 15 minutes. The complete solution has been injected in the middle channel of an X-Junction Chip and squeezed between two flows of acetone. The microfluidic parameter used have been selected from previously results (*see Chapter 2 for further details*): flow rate of 30 µL/min and 110 µL/min for middle and side channels respectively.

3.2.2.3 Particles Characterization

- *Scanning (SEM) and Scanning Transmission (STEM)*

Electron Microscopy: SEM and STEM images were recorded with a FEI Quanta FEG 250 instrument (FEI corporate, Hillsboro, Oregon, USA) with an acceleration voltage of 20 kV. The SEM samples were prepared by drop-casting a dispersion of particles in EtOH onto a glass coverslip, subsequently sputter coated with Au (Emitech K575X Peltier cooled) for 30s at 60 mA prior to the fixation on an

Aluminium support. The STEM samples were prepared by drop-casting dispersions of particles in EtOH onto Formvar-coated Cu grids (400 mesh) and allowed to dry overnight prior visualization.

- *Transmission Electron Microscopy (TEM)*:

TEM samples were analyzed on a FEI/PHILIPS CM120 system operating at 100 kV. Samples were prepared by drop-casting dispersions of particles in EtOH onto Formvar-coated Cu grids (400 mesh) and allowed to dry overnight prior visualization.

- *Dynamic light scattering (DLS) and Zeta Potential (ζ-Pot)*:

The measurements were conducted on a Delsa Nano C Particle Analyzer (Beckman Coulter, operative wavelength 655 nm). The DLS and ζ-Pot measurements were performed on dispersions of the particles in MilliQ water. A certain amount of nanoparticles was dispersed in 1mL of water, and sonicated before the measurement to avoid aggregation phenomena.

- *Thermal stability (TGA):*

Thermogravimetric analysis was conducted on a Netzsch model STA 449 fi Jupiter instrument. The samples (1.0-3.0 mg) were kept at 100 °C for 30 minutes for stabilization, and then heated from 100 to 900 °C at a speed of 10 °C/min, before being held at this temperature for further 30 minutes, and finally cooled. The analyses were performed under 20 mL/min airflow.

- A*ttenuated total reflectance Fourier transform infrared spectroscopy (ATR-FTIR):*

The ATR-FTIR spectra were measured with a Shimadzu IRAffinity-1 spectrometer. The powders were deposited onto the ATR crystal surface and the transmittance spectra were collected using a spectral resolution of $\Delta = 4$ cm^{-1}, accumulating 64 scans and performing the ATR correction (penetration depth mode).

- *Porosimetry:*

Nitrogen physisorption isotherms were obtained with a Micromeritics ASAP-2020 physisorption instrument. The N_2 adsorption/desorption measurements were performed at -196 °C. The surface areas were calculated by Brunauer-Emmett-Teller (BET) method in the relative pressure range *p/p0* 0.06-0.3.[52] The pore size distributions and pore volumes were calculated by density functional theory (DFT) method on the adsorption branch using a cylindrical model. The total pore volume was estimated at *p/p0* = 0.99.

- *ICP-MS and Digestion protocol*

To evaluate the amount of Gd-DTPA loaded in the nanosystem, a defined aliquot of samples was dissolved in a basic solution of NaOH (pH 12) and left for stirring on wheel for 3 days. After this contact time, the solutions were filtered with Syringe Filter 0.22um. The loading capability was calculated by Inductively Coupled Plasma (ICP-MS) NexION 350 measurements. All data are collected and processed using the Syngistix Nano Application Module. Gd-DTPA is measured at m/z 157 using a 100 µs dwell time with no settling time.

- *In vitro T1*

In vitro MR has been realized on produced nanoparticles and results were compared to the control water solutions at a known concentration of Gd-DTPA. After vigorous stirring, 300 μl of the samples were put in glass tubes and changes in relaxation time (T_1) were evaluated at 1.5 Tesla by Minispec Bench Top Relaxometer (Bruker Corporation). The relaxation time distribution is obtained by a CONTIN Algorithm and the relaxation spectrum is normalized by its processing parameters. The integral of a peak corresponds to the contribution of the species exhibiting this peculiar relaxation to the relaxation time spectrum. Experiments were repeated at least ten times.

3.2.3 Results and discussion

3.2.3.1 Characterization of Silica Nanoparticles

The morphological characterization of the organosilica material denoted as NPs1OT was first performed by scanning and transmission electron microscopy (SEM and STEM). The SEM images reported in *Figure 3. 8* displayed homogeneous spherical particles characterized by an average diameter of 56 ± 10 nm (statistical data evaluated with ImageJ software, n= 200).

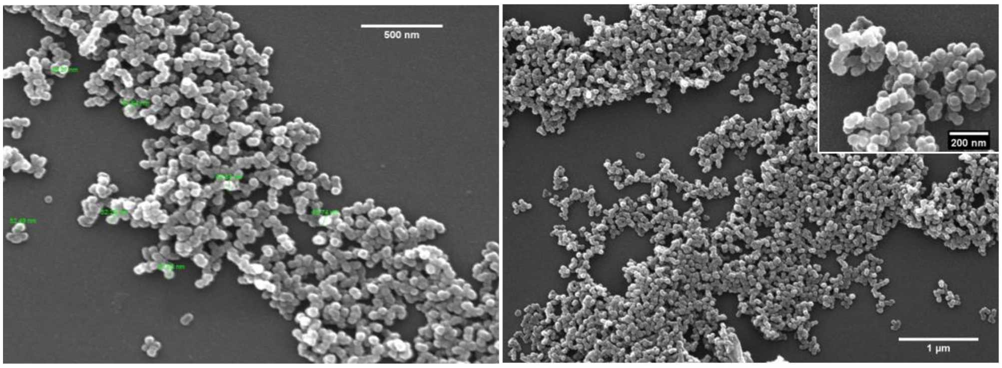

Figure 3. 8: SEM images of morphological characterization of mesoporous silica nanoparticles denoted as NPs1OT. Different zoom areas were reported.

However, this data conflicted with the DLS measurement in water that reported a mean value of 180nm. The obtained difference in size values between DLS and SEM analysis, could be further emphasized by aggregation phenomena of nanoparticles dispersed in water.

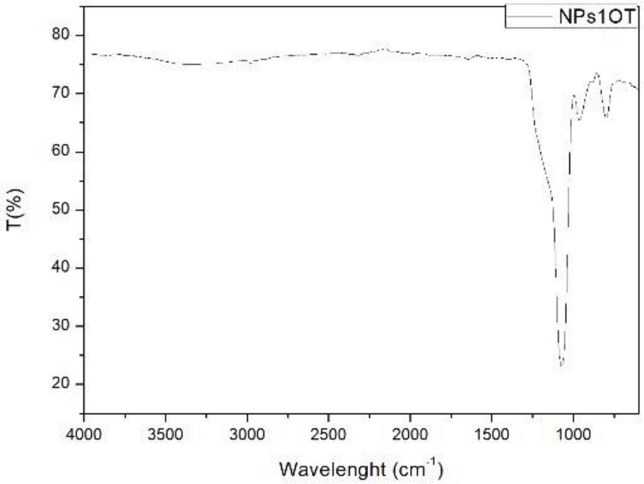

Figure 3. 9: ATR-FTIR spectrum of NPs1OT. It was possible to note the typical peak for the Si-O bond (1072cm^{-1}). Moreover, the absence of peaks in the region 2500-3700 cm^{-1} confirms the goodness of the purification protocol used.

The chemical constitution of NPs was investigated by FTIR on the dried sample (*Figure 3. 9*). The bands at 1072 cm^{-1} and 795 cm^{-1} in these NPs are due to asymmetric and symmetric stretching frequencies of Si-O-Si bond, while the peak at 964 cm^{-1} corresponds to Si-OH moiety (this band disappears after TGA analysis). The wideband at 3370 cm^{-1} can be attributed to the presence of hydroxyl groups on the surface of the NPs.

The TGA measurement showed a high thermal stability with a loss of around 2% that was attributed to the decomposition of silanol moieties (*Figure 3. 10*).

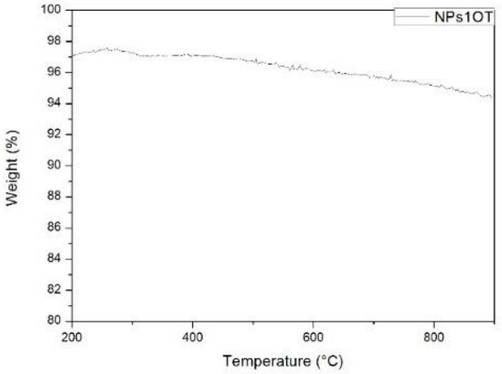

Figure 3. 10: Thermogravimetric measurement indicates a high thermal stability of the produced nanoparticles.

The N_2 sorption measurements were carried out to evaluate the mesostructural properties of these nanosystems. The analysis of the adsorption/desorption isotherms allowed to calculate for NPs1OT a BET surface area of 570,13m^2 g^{-1}, a total pore volume of 0.32 cm^3.g^{-1} and an average pore size of 3,9 nm (*Figure 3. 11*).

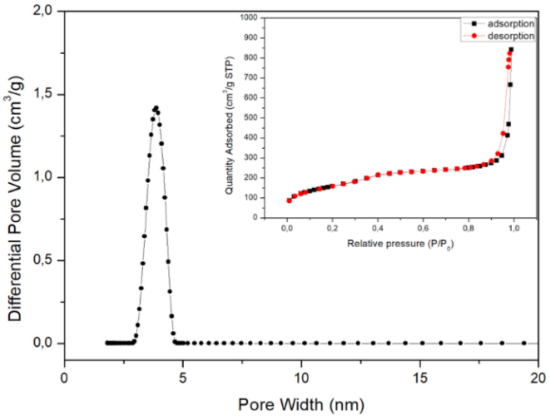

Figure 3. 11: Porosimeter measurement of NPs1OT indicates a porous mean size of 4nm, while in the inset was reported the absorption and desorption curves with NH_2, fitted with the BET methods.

To create a possible point of linkage with Gd-DTPA a post-synthesis treatment was conducted, before loading with amino group and successively with the impregnation of Gd-DTPA molecules. The success of amino groups loading on nanoparticles surface was confirmed by a variation on ζ-potential value (from -24,31± 1,03 mV to -0,28 ± 0,87mV) and in a higher loss in weight of 11% that can be attributed to the presence of -NH groups. Furthermore, a high increasing size of nanoparticles has been reported after the amino loading (DLS value: 518 ± 50 nm), but the variation of ζ-potential observed was not enough to promote a physical impregnation of Gd-DTPA molecules on NPs1OT surface.

These observations lead us to define this protocol as not optimal in our perspective to obtain nanosystems for medical applications in MR diagnostic field.

To obtain Gd-loaded silica nanoparticles, different synthesis pathways have been studied. Instead of post-synthesis modification procedures, as reported before, one-step synthesis protocols for the production of silica nanostructure loaded with Gadolinium- DTPA have been analyzed.

The silica loaded nanoparticles were synthesized using the Stober method[49] with slight modification in a W/O microemulsion. Reverse microemulsion can produce hydrophilic and uniform-sized NPs and allows easy modulation of the NP surfaces for various applications. In the synthesis of NPs3OT and NPs4OT, we have introduced the Gd-based contrast agent solution directly into the microemulsion reaction phase during the synthesis process, as reported by Zhou et al.[42], making the Gd-DTPA a direct component of this reverse microemulsion reaction system.

The morphological analysis of these two systems were reported in *Figure 3. 12*, while the high thermal stability and the chemical analysis were shown in *Figure 3.*

13. The FTIR spectra have been compared with the Gd spectra, with the aim to investigate its effective presence into the nanoparticles. The distinctive Gd-DTPA bands were not clearly present in nanoparticles spectra, furthermore, also the TGA analysis didn't reveal the typical weight variation of Gd-DTPA, as explained in *Figure 3. 14*, where are clearly represented the peaks of chelating agent degradation at high temperatures. This discrepancy could be attributedto a very low percentage of CA loaded in nanosystems.

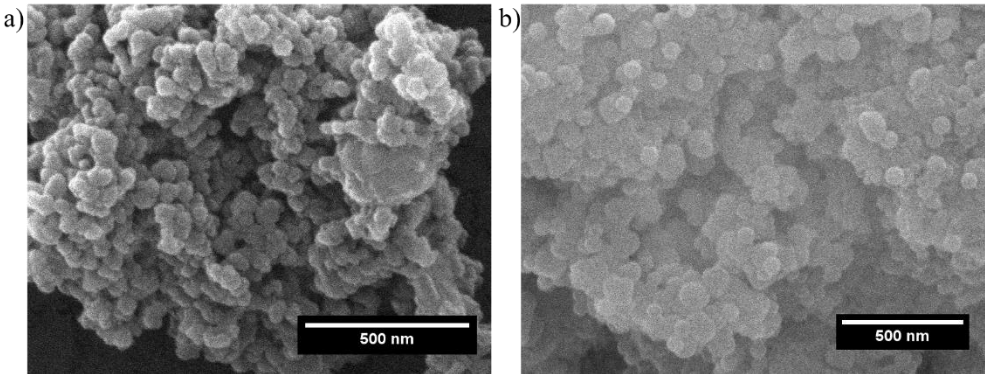

Figure 3. 12: Morphological characterization of nanosystem called NPs3OT and NPs4OT, a) and b) respectively. These systems were obtained through the microemulsion method where the Gd-DTPA solution was considered as a direct component of the emulsion.

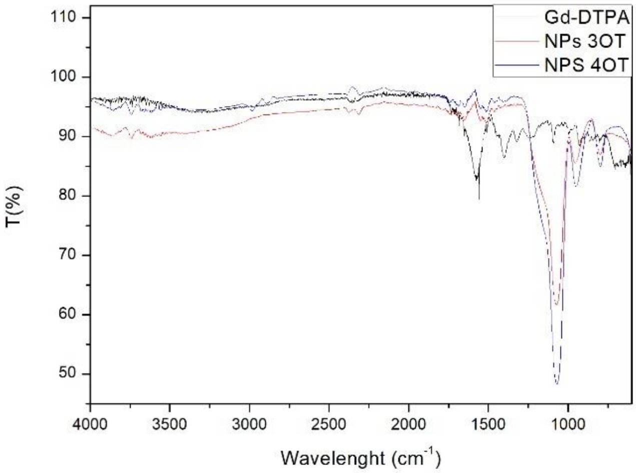

Figure 3. 13: Comparison between ATR-FTIR spectra for Gd-DTPA powder and NPs3OT and NPs4OT. The typical peak in the Gd-DTPA sample were not found in silica nanoparticles.

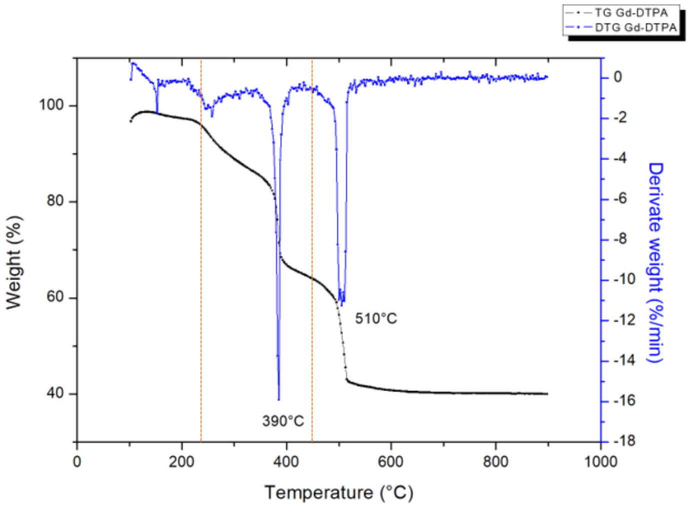

Figure 3. 14: In this figure is reported the typical curve of thermal degradation for Gd-DTPA powder.

Continuing with the aim to obtain in a single step process a silica nanostructure loaded with Gd-DTPA, different synthesis methods had been tested, using a direct microemulsion method. T-MSNs were synthesized by a modified Stober method[49] by using TEOS and Tween 80 as the structure-directing agent. As described by Maqbood[48], the major factors involved in governing the morphology of silica particles are the rate of hydrolysis of TEOS precursor and the rate of condensation of Si-OH to generate siloxane bonds. With this protocol, the formation of T-MSNs typically starts with the nucleation of silica around the head groups of Tween micelles through surfactant-silicate interaction most likely surfactants. This silica condensation subsequently results in aggregation of singular micelles to clusters. The continuous condensation of TEOS around the existing silica results in the deposition of silica between interfaces of micelles in an aggregate. The vigorous and uniform stirring favours micellar aggregate re-arrangement and helps in the formation of monodisperse nanoparticles.

Figure 3. 15: In the case of T-MSNs, after the solvent evaporation all the sample can be transferred in an Eppendorf tube for cleaning step.

In our experiment the total amount of Tween 80 and ammonia in the reaction mixture was fixed at 8 nmol and 8mL, respectively that correspond to 10µL Tween 80 into 8mL of ammonia solution (28-30%). After the complete evaporation of the solvent, the materials come up as a white sol that could be completely transferred in an Eppendorf tube (*Figure 3. 15*). The obtained T-MSNs were purified by repeated centrifugation and re-dispersion in distilled water and finally in ethanol.

A study on the ratio ethanol: water has been conducted. The characterization of the product with a ratio of ethanol: water 1,28:1, was in accordance with the result from the reference work[48]. Monodisperse spherical nanoparticles of diameter 50 ±15 nm were obtained.

N2 adsorption measurement reveals the presence of wormhole-like porosity with a pore size of 2nm (*Figure 3. 16 a*).

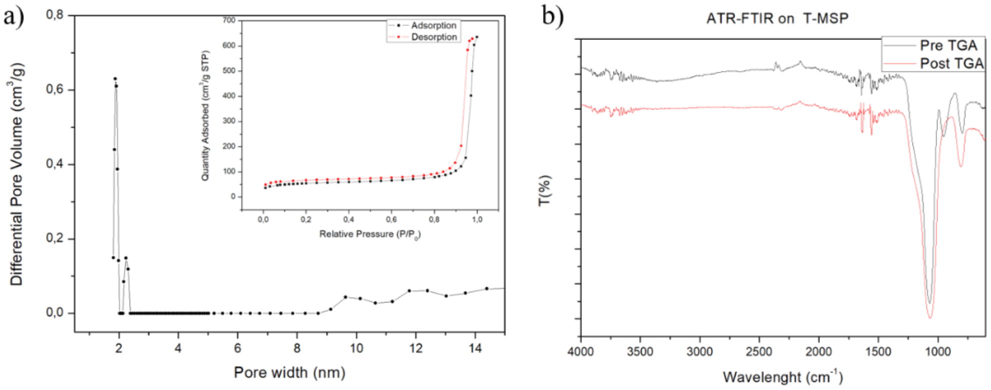

Figure 3. 16: In the panel are showed a) porosimeter and b) pre- e post- TGA measurement on sample T-MSP

Figure 3. 16 b showed the ATR-FTIR spectra of samples before and after thermal treatment (TGA measurement). It was clearly visible the typical Si-O peak for both, while the peak associated with Si-OH vibration disappear in the sample after TGA.

Interestingly when the same synthesis procedure was applied just with the presence of Gd-DTPA in the aqueous phase (the same amount of water but with a concentration of 1mg/mL) as a direct component of microemulsion, it was possible to observe an influence due to CAs salt on final products properties. The resulting material, T-MSN1, showed particles with a mean size of around 70nm while it was not possible to obtain data from N2 adsorption measurement. The non-porous material leads to hypothesize that the molecules of Gd-DTPA could be entrapped in the pore of the nanostructure. To evaluate the presence of CAs molecules a comparison of TGA and ATR-FTIR data between T-MSN and T-MSN1 has been conducted. The presence of slight variation was not enough to assert an effective presence of Gd-DTPA within the system, thus requiring further study. Conversely has been studied the effect of varying the ratio EtOH: water, considering as water phase as the one containing or not the Gd-DTPA molecules. It was possible to observe an increase of mean size value respect the water amount. In particular in the case of ratio EtOH: water 1,2:2, T-MSN2, STEM and SEM micrograph showed a double population of nanoparticles (*Figure 3. 17*).

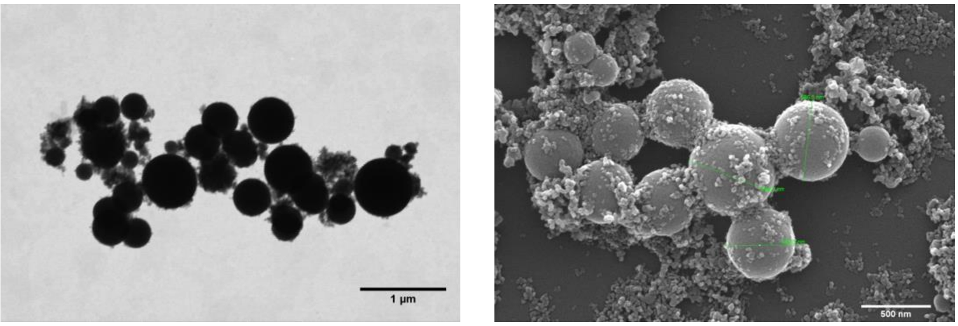

Figure 3. 17: Electron Microscopy Image showed double population of nanoparticles for the sample T-MSN2, (STEM and SEM respectively)

With the aim to synthesize MSP systems with a mean size of less than 50nm, we investigate the possibility of combining two silica precursors: TEOS and APTES. The presence of APTES molecules affected the size of nanoparticle as reported by Oliveria and co-worker[53], and increase the ζ-potential value. This new formulation, also with the addition of Gd-DTPA during the emulsion step, allowed the production of uniform nanoparticles, denoted as AT-MSN1, with a mean size around 30 nm and pore size distribution of 1,8nm by BET fitting. The small size of the obtained nanoparticles was due to the dual effect of combination Gd-DTPA as emulsion component and APTES as further silica precursors. Indeed, the same synthesis protocol, conducted without Gd-DTPA produces a monodisperse population of NPs (AT-MSN) with a higher average size (100nm). Also, in this protocol, an increase in the amount of present water leads to an increase in the average size of the obtained nanoparticles.

Following the T-MSN protocol, also the ratio TEOS: APTES has been varied, and the resulting materials showed a positive charge (ζ-pot of +17,45 mV), with a mean size of 60nm.

3.2.3.2 Microfluidic Implementation of SiO_2 NPs in PEG-cHANPs production

The organosilica systems described into *Paragraph 3.2.3.1* were also implemented by a microfluidic process to obtain a complex structure for medical application. In particular, to demonstrate the versatility of our microfluidic platform, as described in *Chapter 2*, pre-synthesized SiO_2 NPs were added to a polymeric solution containing hyaluronic acid, crosslinked PEG and Gd-DTPA, and processed in a Hydrodynamic Flow Focusing. The polymeric solution containing HA-SH, Gd-DTPA, SiO_2 NPs, and PEG-VS was kept in stirring on a wheel to promote an adequate mixing of the component. After that, the complete solution has been injected in the middle channel of an X-Junction Chip and squeezed between two flow of acetone (flow rate ratio used of 0,27). The schematic representation was illustrated in *Figure 3. 18*.

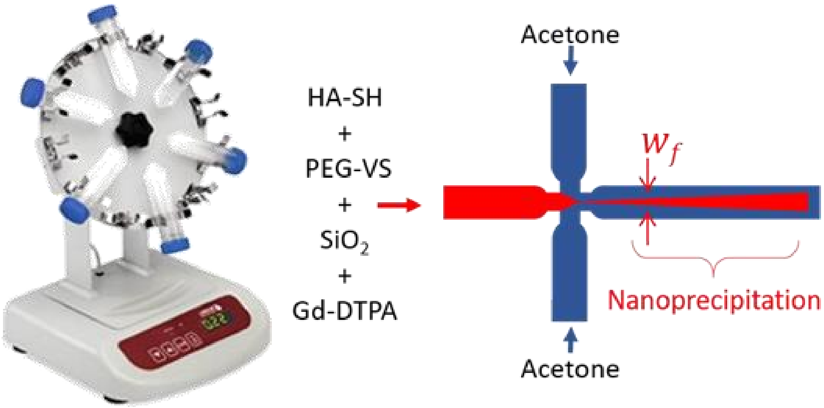

Figure 3. 18: Schematic representation of the implementation process in microfluidic.

3.2.3.3 Interference of SiO_2 in Nanoprecipitation process

The first test was conducted with *positive* MSP. The presence of solid component, represented by SiO_2, has acted as interference during the nanoprecipitation process, promoting nucleation sites. During the trial, it was possible to observe the formation of precipitate near the wall of the outlet channel.

The obtained material was collected in a closed vial containing 3mL of acetone, kept in stirring overnight and after that dialyzed to remove all the non-reacted materials.

Scanning Electron microscopy (SEM) analysis showed the formation of spherical nanoparticles, with a good dispersion and a mean size of 200nm (*Figure 3. 19.a*). The transmission micrograph showed the formation of a core-shell structure that could be attributed to an inner core of SiO_2 and an external shell composed of crosslinked HA-SH/PEG-VS (*Figure 3. 19.b-c*).

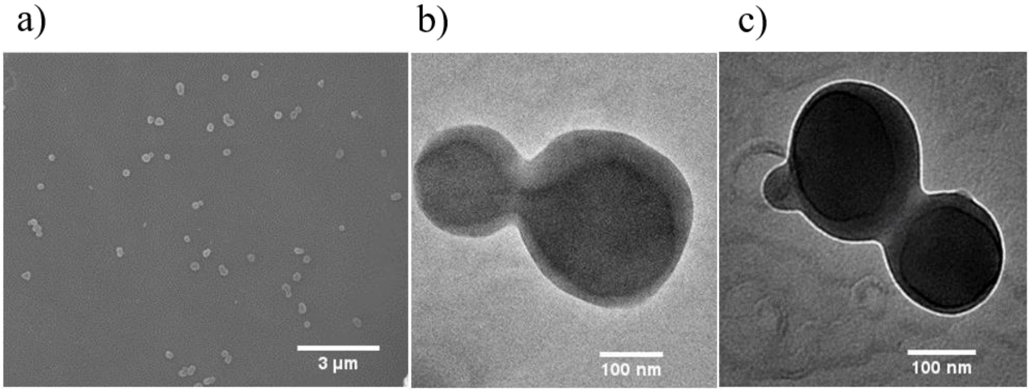

Figure 3. 19: Morphological characterization of the hybrid system: a) SEM images at the wide range of nanoparticles with a uniform population,b) and c) TEM images of core-shell structure obtained, the inner dark core could be attributed to inorganic component SiO_2 while the external layer was composed of crosslinked HA-SH/PEG-VS.

The analysis with ImageJ program reveals a thickens of the external layer of about 10nm. The content of Gd-DTPA loaded in the hybrid nanostructures has been evaluated by ICP-MS analysis and compared to the Minispec value obtained through a Contin algorithm. The data showed an encapsulation efficiency of Gd-DTPA of 40% that corresponds with a Gd-DTPA concentration of 70mM. The value of concentration obtained by MINISPEC analysis trough a calibration curve, confirm the same value of ICP-MS without an enhancement of the relaxivity signal.

It is possible to declare that in this case, the presence of selected solid components did not influence the EE% of loaded agent., but the desired effect due to Hydrodenticity was missed. It was possible to speculate that the positively charged silica nanoparticles act binding electrostatically the Gd-DTPA molecules thus inhibiting their mobility and consequently removing the effect of higher hydration due to hydrophilic mesh of polymers.

To overcome this possible effect of electrostatic interaction the additional trials have been conducted with negatively charged MSP. Two different contact times with Gd-DTPA solutions have been tested: 3 days and 30 min denoted as S4 and S5 respectively. The microfluidic procedure was the same as reported above. Results presented in *Figure 3. 20* showed that different nanostructures have been produced.

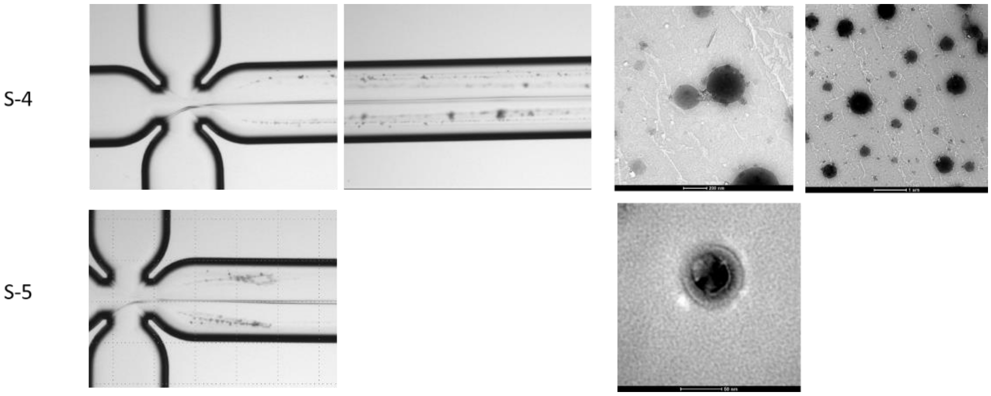

Figure 3. 20: The panel represents the optical images of the microfluidic chips during the trials and the obtained nanostructures analyzed by Transmission Electron Microscope

Indeed, in this case, the TEM images reveal a complex structure where did not appear a unique core, but there were presented many spots of electron dense material (correlated to SiO_2) embedded in less electron dense matrix. The difference due to contact time could be observed in the different precipitation patterns of material in the outlet channel, during the microfluidic process. The Minispec evaluation (*Figure 3. 21*) showed a similar relaxivity time of these two hybrid samples. Further measurements are needed to establish the correct amount of Gd-DTPA loaded in order to consider the Hydrodenticity effect.

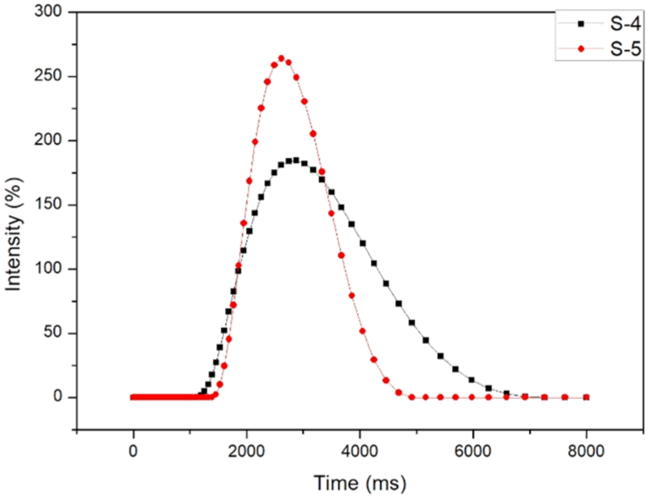

Figure 3. 21: In vitro MR. Comparison of longitudinal relaxation time distributions of trials S-4 and S5.

3.3 Encapsulation strategies of Indocyanine Green (ICG)

3.3.1 Introduction

Indocyanine green (ICG) is an amphiphilic, near-infrared dye that has been approved by Food and Drug Administration (FDA) in the USA for studies in humans. ICG exhibits emission maxima around 800 nm (excitation at 780 nm) that make it highly suitable for bio-imaging applications with high signal to- background ratio. This wavelength region is free form signal by biomolecules signals, making its fluorescence relatively free of intrinsic background interference. ICG also can convert the absorbed light into energy that can produce heat and toxic chemical species, forming the respective bases for photoacoustic imaging (PA), photothermal (PT) and photodynamic (PD) therapies[54]. Nowadays the use of this dye is limited by its drawbacks: the instability of ICG in aqueous solution (degradation follow "pseudo" first-order kinetics) is accelerated by light exposure and high temperatures[55], resulting in a simultaneous loss of absorption and fluorescence; short circulation time (half-life, $t_{1/2}$=2-4 min); easy to bind non-specifically to human serum albumin with consequently rapid clearance by the liver. Therefore, to overcome these limitations, ICG molecules can be embedded, doped and conjugated with different NPs with different preparing strategies [56-59].

In order to define the stability of ICG in our nanosystem, a physicochemical characterization has been done. The ICG stability has been studied using Spectrofluorometry and UV-vis analyses; the size and the morphology have been defined by Electron Microscopy (SEM and TEM) and DLS measurement.

3.3.2 Materials and Methods

Hyaluronate Thiol (HA-SH) with 5 mol % substitution, MW 50 kDa, and mPEG-Vinylsulfone (PEG-VS), MW 2kDa, were purchased from Creative PEGWorks. Diethylenetriaminepentaacetic acid gadolinium (III) dihydrogen salt hydrate Gd-DTPA (97%), Ethanol (ACS reagent, (200 proof), absolute; Acetone (puriss. p.a., ACS reagent, reag. ISO, Ph. Eur., ≥ 99.5%); Sodium Hydroxide NaOH (ACS reagent, ≥ 97.0 %, MW 40.00g/mol), CardioGreen (ICG) MW 774.96 g/mol (Ex/Em 780/800) and 5,5-dimethyl-1-pyrroline-1-oxide (DMPO) spin-trap, were purchased from Sigma-Aldrich, Water for synthesis and characterization, was purified by distillation, deionization, and reserve osmosis (Milli-Q Plus; Merck, Darmstadt, Germany).

3.3.2.1 Microfluidic set-up

A quartz microfluidic device "Droplet - Junction Chip" purchased from Dolomite Centre Ltd, was used. An X-junction with three inlets and a single outlet channel has been used. The device has a flow-focusing geometry with a 90° angle between the inlets to enhance the diffusion process. The flow focusing regimen in the microchannel is observed through an optical fluorescence microscope (Olympus IX71) with a 4x scanning objective.

In the middle channels the solution injected was composed by HA-SH 0,5%wt/v, PEG-VS 0,18%wt/v, ICG 0,0025%wt/v and Gd-DTPA 0,1%wt/v, while the acetone was fluxed in the side channels, with a fixed FR^2 of 0,27.

3.3.2.2 Particles Characterization

- *Fluorescence Analysis*

Samples were analyzed with a Horiba Spectofluorometer. The volume of 500uL of sample was moved in a quartz cuvette and after the analysis was carried out. For the stability study, the cuvette was recovered after each analysis and covered with aluminium foil to prevent light degradation.

- *UV-Vis Analysis*

Samples were analyzed with a spectrophotometer Varian Cary 100 Scan. The volume of 1 mL of sample was put in quartz cuvette e covered with aluminium foil to protect the sample from light degradation. The acquisition spectra used for the characterization was from 650nm to 815nm.

- *Confocal Microscopy*

Samples were imaged with a Leica TCS STEDCW microscope (Leica-Microsystems, Mannheim, Germany) equipped with an oil immersion 63x objective. Images were acquired with a field of view of 25.6 × 25.6 µm for a pixel size of 25 × 25 nm. The analysis of the images was carried out using LAS AF software.

- *In vitro T1*

In vitro MR has been realized on loaded NPs and results were compared to control water solutions at a known concentration of Gd-DTPA. After vigorous stirring, aliquots containing 300 µl of the sample were put in glass tubes and changes in relaxation time (T1) were evaluated at 1.5 Tesla by Minispec Bench Top Relaxometer (Bruker Corporation). The relaxation time distribution is obtained by a CONTIN Algorithm and the relaxation spectrum is normalized by its processing parameters. The integral of a peak corresponds to the contribution of the species exhibiting this peculiar relaxation to the relaxation time spectrum. Experiments were repeated at least ten times.

3.3.2.3 Electron Paramagnetic Resonance analysis (EPR)

The sets of EPR measurements were performed by using spin trapping. This method was used to detect reactive oxygen species (ROS) production by Indocyanine Green. For the detection of ROS species in aqueous dispersions of nanoparticles, samples were prepared by using the following procedure.

A define aliquot of NPs (20µL of NPs with a concentration of ~5µM) was added to DMPO (50µL spin trapping from a stock solution of 4mg/mL). After 5 min of contact, the sample was put in a petri dish and then irradiated for 5 minutes, with a NIR lamp, positioned at a distance of 15cm from the sample. 20 µL of liquid samples were transferred to flame-sealed glass capillaries which, in turn, were coaxially inserted in a standard 4mm quartz sample tube. Measurements were performed at room temperature.

The instrumental settings were as follows: sweep width, 100 G; resolution, 1024 points; modulation frequency,100 kHz; modulation amplitude, 1.0 G. The spectra samples were registered with an attenuation of 15 dB and several scans, respectively 512 and 32, were accumulated to improve the signal-to-noise ratio.

3.3.3 Results and Discussion

A feasibility study on fluorescence behaviour has been conducted to evaluate the best working-range for our microfluidic production process of nanovectors. In particular, taking in mind that the required dialysis steps for cleaning are conducted with different solvent (*see Chapter 2*), it was needed evaluate the effect of ethanol and water on ICG stability, Different concentration of dye have been measured for three days in distinct storage condition, with a λ_{ex} =778 and spectrum acquisition region from 795 to 845 nm. The resulting data are showing in *Figure 3. 22*. It was possible to observe that in the case of 100ug/mL of concentration, in both solvents, the fluorescent signal intensity registered is extremely low. This effect is supported by Saxena et al[55] that explain the phenomena with the formation of ICG molecular aggregate. Indeed, a higher concentration leads the formation of quenching centers, attributed to molecules closely spaced pair, that exhibit weak fluorescence intensity. This state has been observed for all the storage conditions (dark or light). For the lower concentration tested (1µg/mL) the intensity signal showed a more accentuate degradation for the storage at light when the storage is in water, as expected. It was interesting to note that in the solvent case of ethanol, the value of the intensity signal was not very high, but was more stable compared with the other condition. The best situation in terms of concentration was represented by the value of 10µg/mL. At this value of concentration, the signal intensity was well defined for each storage condition.

The degradation in water for light storage was present but a signal different to background was still appreciable. The degradation of ICG in aqueous solution is due to the formation of leucoforms, that were not able to emit in the wavelength region of ICG emission. A deeper analysis of recorded spectra, reveals furthermore, that there was a dependence on the wavelength of peak fluorescence due to increased concentration in non-aqueous solutions (see *Table 3. 2*).

Table 3. 2: Dependence of ICG peak fluorescence by solvent phase and concentration (ug/mL*)*

ICG [ug/mL]	Peak Fluorescence Wavelength [nm] H_2O	Peak Fluorescence Wavelength [nm] EtOH
1	803	808
10	804	810
100	---	818

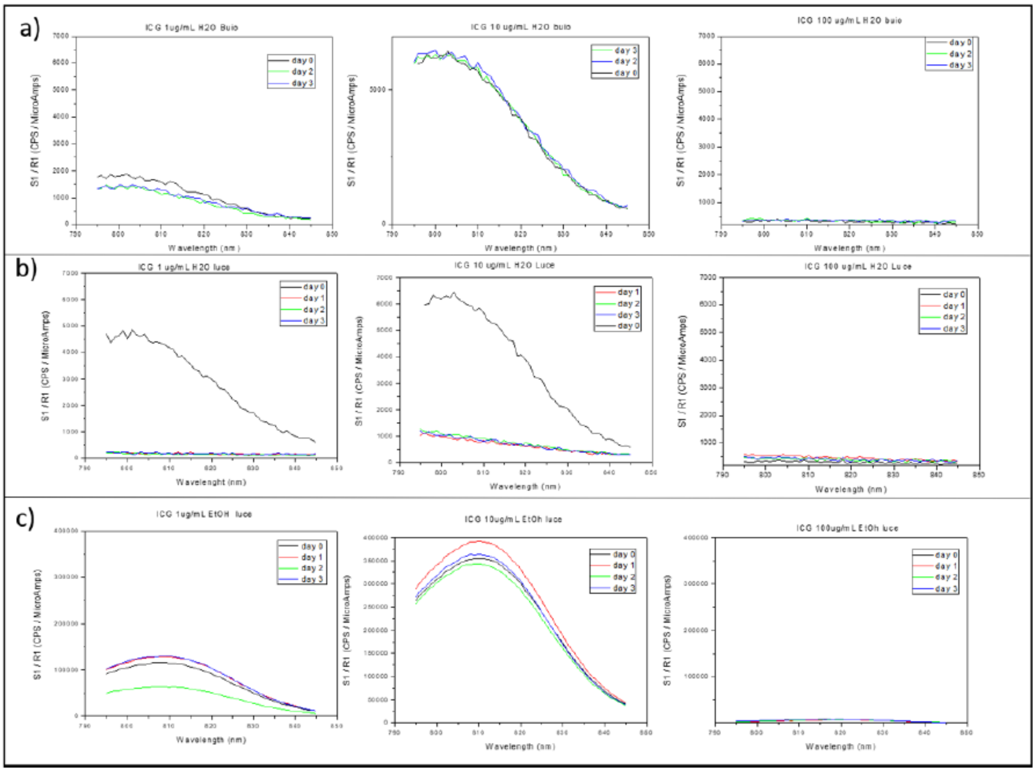

Figure 3. 22: Stability studies on different concentration at different storage condition

The best concentration range was corresponding to a concentration value of 10ug/ml (equivalent to 12nmol/ml) and according to this, spectrometer and spectrofluorimeter calibration curves in water have been calculated.

The adsorbed spectra in *Figure 3. 23*, measured by UV-Vis, showed a linear correspondence between the amount of dye and the signal intensity (a direct consequence of Lamber Beer Law). It was possible to note the presence of two absorbance peaks, due to the difference between the monomeric and dimer form if ICG. At low concentration, the monomeric form was the most influent with an intense peak (778nm), while the presence of dimer form was detectable as a peak at ~710nm[60].

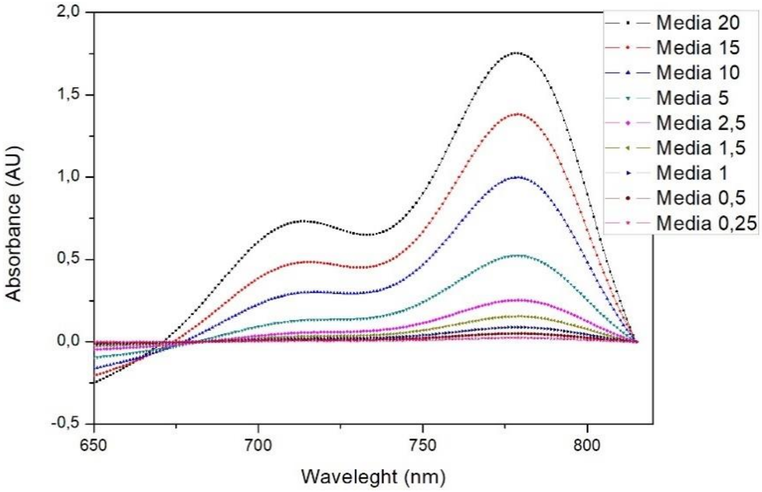

Figure 3. 23: Calibration curve obtained from UV-Vis adsorbent data of defined aliquot of dye in aqueous solution.

The fluorescent spectra (λex =778nm, windows acquisition 795-845nm) for the calibration curve were reported in *Figure 3. 24*. In this case, the data interpretation was not as easy as before for UV-Vis measurement. Indeed, at high concentration, the presence of dimers and agglomerate molecules of ICG, perform as quenching factor for intensity signal. Moreover, increased concentration corresponds to a redshift of fluorescence peak. The linear regression curve could help in the visualization of this effect. Firstly, it was necessary to separate the data into two sets: from 0 to 5nmol/mL and from 5 to 20nmol/mL. This separation allowed also to consider the effective peak region for each curve since different concentrations correspond to different peak values (range 800-803nm for concentration lower than 5nmol/mL and 803-806 nm for higher concentration). The results were presented in *Figure 3. 25*. The negative slope in *Figure 3. 25.b* could illustrate the quenching effect due to agglomerated molecules at high concentrations of ICG content.

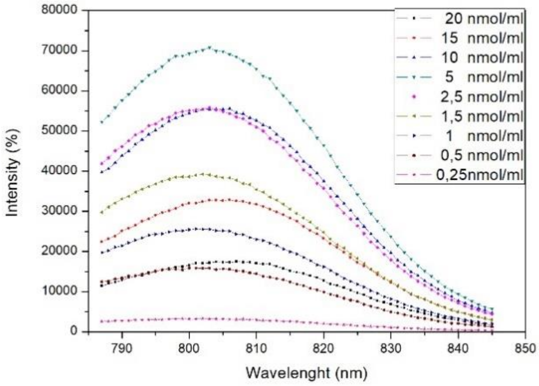

Figure 3. 24: Calibration curve obtained from fluorescence spectra of define amount of dye in aqueous solution.

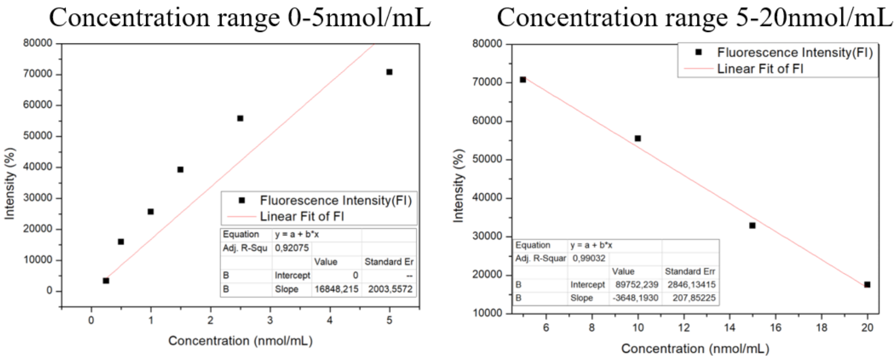

Equation	y = a + b*x		
Adj. R-Squ	0,92075		
		Value	Standard Er
B	Intercept	0	--
B	Slope	16848,215	2003,5572

Equation	y = a + b*x		
Adj. R-Squar	0,99032		
		Value	Standard Err
B	Intercept	89752,239	2846,13415
B	Slope	-3648,1930	207,85225

Figure 3. 25: The plot represents the linear fitting of the maximum value of fluorescence intensity from the calibration curve. It was necessary to split the fitting in two regions to obtain a good fitting value.

Starting from this observation, we moved to the implementation in a microfluidic one-step process to obtain PEG-cHANPs loaded with ICG.

A fresh ICG stock solution (100ug/mL) was prepared daily before using it and covered with aluminium foil as light protection. A polymeric solution containing HA-SH (0,05%wt/v), Gd-DTPA (0,1%wt/v) was stirring for 15minutes before adding ICG (0,0025%wt/v) and kept in stirring. Before adding PEG-VS (0,18%wt/v) the temperature was cooled down with an ice bath and left on stirring for 15minute.

The obtained polymeric solution was compared with the ICG solution by UV-Vis analysis to establish a possible influence due to the presence of other components. Furthermore, this polymeric solution has been diluted in ethanol in order to examine behaviour and influence on dye performance in non-aqueous solvent with polymers.

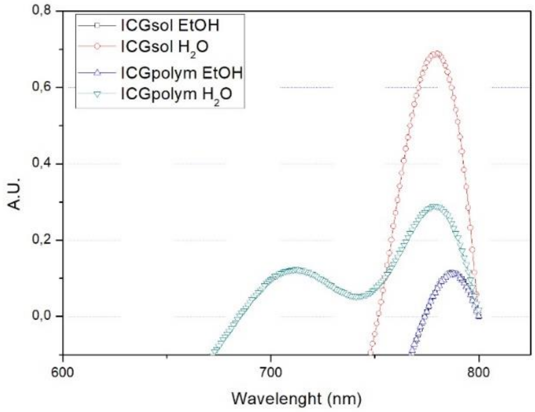

Figure 3. 26: UV-Vis data for the complete polymeric solution, dispersed in two different solvents (water and ethanol, respectively)

Recorded spectra showed, as expected, a shift in peak wavelength between the aqueous and ethanol solution, 778nm and 790nm respectively. All the samples had the same concentration in terms of ICG content, however, the intensity of absorbance varied considerably. The polymeric solution in H_2O affects the absorbance spectra of ICG. Indeed, the presence of solvent radicals, ions and reactive moieties in solution could saturate the double bond in ICG chain, leading the formation of leucoforms[55]. Otherwise, in ethanol, this effect was not registered. The ICG spectra in free and polymeric ethanol solution could be completely overlapping, emphasizing in this way the influence of polymeric materials on ICG molecules.

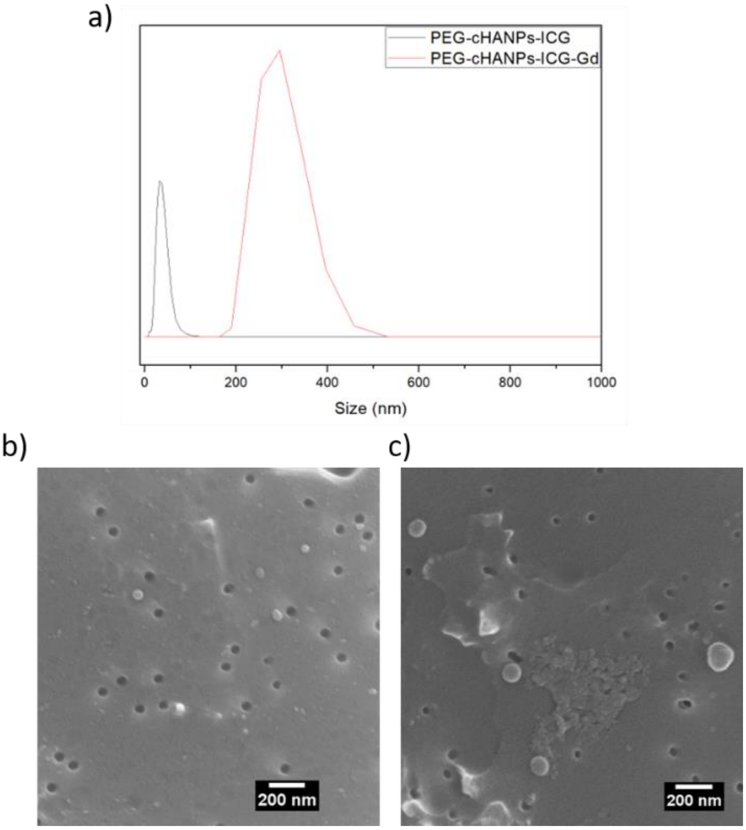

Figure 3. 27: Morphological Characterization of obtained d PEG-cHANPs loaded with ICG and co-loaded ICG-GdDTPA.

Once obtained information about the polymeric influence on ICG, the complete solution, composed by Hyaluronic Acid, PEG-Vynilsulfone, and Gd-DTPA, was processed in microfluidic. An HFF approach led to the production of PEG-cHANPs loaded with ICG molecules. The complete polymeric solution was injected in the middle channel and squeezed between two lateral flows of acetone with a final FR[2] value of 0,27 (30µl/min in the middle channel and 110µl/nm in the side channels), and collected in a Petri dish containing 20 mL of acetone. DLS and SEM micrographs reported in *Figure 3. 27* showed morphological characterization of obtained nanosystems with an average size of 40 nm and 150nm, without and with Gd-DTPA respectively. It was interestingly observed that the presence of Gd-DTPA influences the final size of the nanoparticles. Furthermore, also in this case when the collection phase is conducted in a closed vial with 3mL of acetone, the mean size of the system increased about 250nm. Confocal microscopy analysis of PEG-cHANPs-ICG was reported in *Figure 3. 28*, where the image shows luminescent dots correlated to NPs.

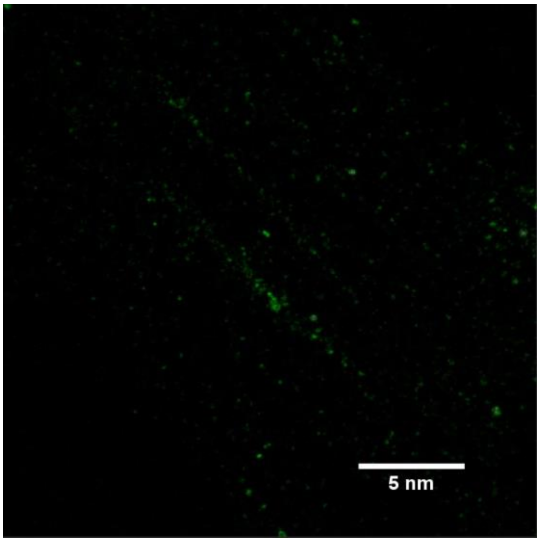

Figure 3. 28: Confocal Microscopy Image showed colored spots corresponding to NPs loaded with the dye.

In order to evaluate the properties of the loaded nanoparticles, a spectrofluorometry analysis has been conducted. The excitation wavelength select for this study was 778nm, which is the common wavelength in use for ICG studies. The spectra measurement reported in *Figure 3. 29* showed that the formation of a polymeric matrix around dye molecules could influence the fluorescence signal with a peak redshift. This effect was more intense than the one associated with different solvent influences. Indeed, PEG-cHANPs-ICG dispersed in ethanol and in water had the same peak position, 812 nm, but different intensity.

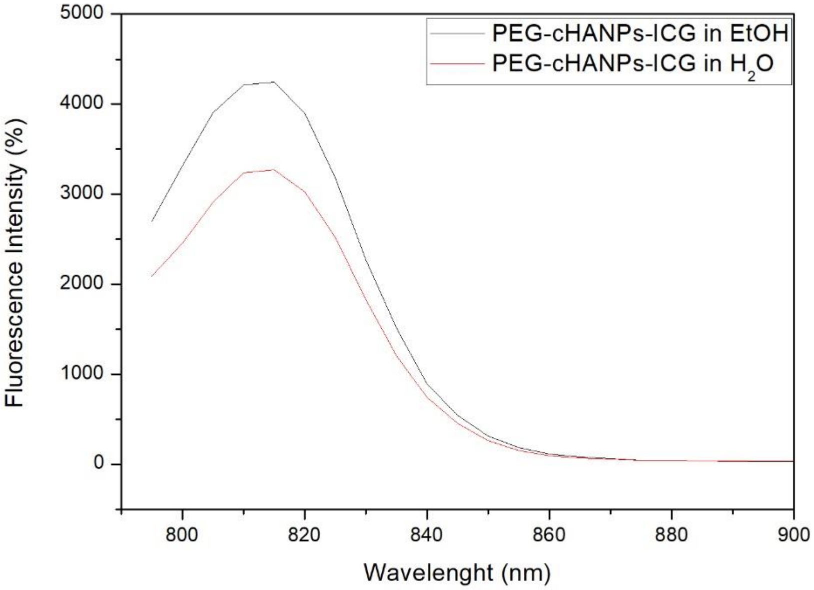

Figure 3. 29: Fluorescence spectra of PEG-cHANPs-ICG in different solvents.

3.3.3.1 CLEM Analysis

To check the effective dye presence within the nanoparticles and not their molecular presence as dissolved phase in the solvent, we moved to confocal microscopy analysis.

Unfortunately, our confocal microscopy was not equipped with a NIR laser and so, in order to conduct a more detailed confocal study on PEG-cHANPs-ICG we studied the possibility to excite the nanosystem with wavelength different from 780nm. Spectrofluorometry analyses of free ICG in aqueous solution(10nmol/mL) and PEG-cHANPs loaded-ICG, at different λ_{ex}, have been conducted in order to find the best excitation wavelength and then compared with the standard λ_{ex} of 780nm. The excitation wavelengths for testing were 405 nm and 633 nm. In *Figure 3. 30* were showing the emission spectra recorder for free ICG and PEG-cHANPs-ICG. The nanoparticulate system expressed a great interaction with λ_{ex} 405, as before reported in C*hapter 2*, but the signal around 800nm was not detectable in order to overcome the interference of the double wavelength of excitation. Also, in the case of free ICG, it was present an emission peak around 450nm.

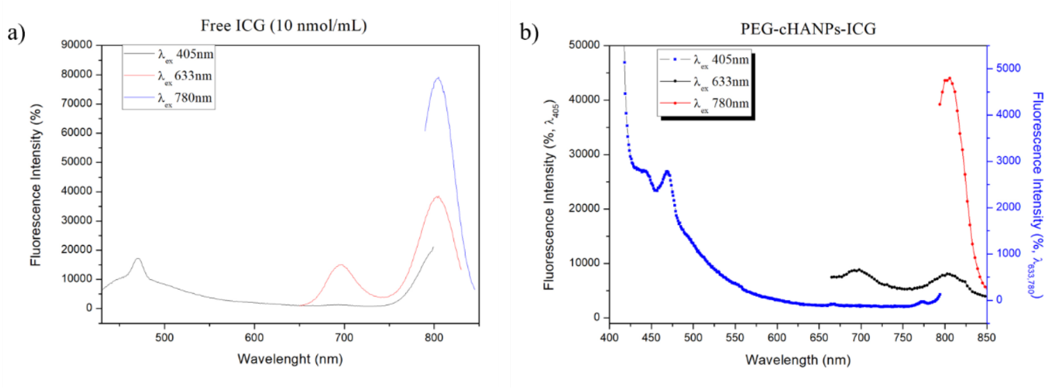

Figure 3. 30: Spectrofluorometry analyses have been conducted on free ICG in aqueous solution(10nmol/mL) and PEG-cHANPs loaded-ICG, at different λ_{ex}: 405nm, 633nm, and 780nm

Interestingly, when excited with λ_{ex} 633nm, the spectra for both samples, showed the presence of a double peak, with a good intensity that could be easily detected by confocal microscopy.

To our best knowledge, in literature data was not reported any investigation regarding the formation of these two peaks when ICG was irradiated with 633nm.

Taking into account the results of the UV-Vis absorbance curve of ICG, obtained at the wavelength of 633 nm and the intensity of 30% of the total, the further investigation of solution behaviour was conducted at this particular wavelength.

With the aim to better understand, we investigated the difference in fluorescence spectra between the free ICG solution and the polymeric solution with and without the presence of Gd-DTPA.

Indeed, the presence of salt, in our case represents by Gd-DTPA, influenced dye stability, quenching the fluorescence signal.

ICG solution

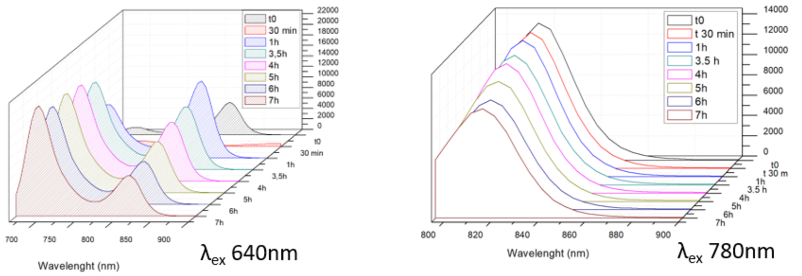

Polymeric solution + ICG

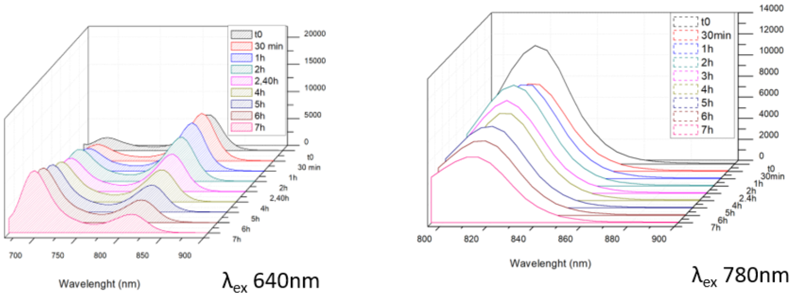

Polymeric solution + ICG + Gd-DTPA

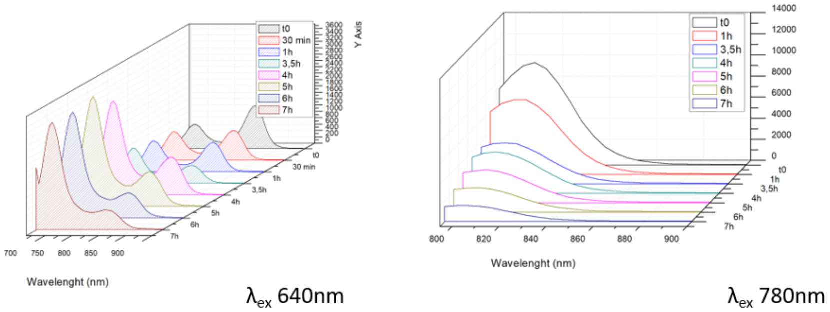

Figure 3. 31: Comparison of the degradation behaviour of different ICG solutions irradiated at 640 nm and 780nm.

As clearly demonstrated in *Figure 3. 31*, the double peak when irradiated at 640nm, could be attributed to an increased amount (or concentration) of a degradation product. During the time, when the intensity of NIR peak decreases, the intensity of degradation product increases linearly.

The presence of the polymeric solution reduces the fluorescence intensity of the starting point, but then the increment of degradation peak was slow. After the addition of Gd-DTPA to the polymeric solution, the quenching of NIR fluorescence signal was clearly detectable, while the increasing signal of degradation peak was intense.

3.3.3.2 EPR spin trapping studies

Electron Paramagnetic Resonance (EPR) study has been conducted in order to assess the photodynamic property of PEG-cHANPs-ICG systems. This property was triggered by oxidative stress due to free radical production under NIR irradiation. The generation of reactive oxygen species (ROS) in an aqueous environment was investigated by the spin-trapping method.

Indeed, the extremely high chemical reactivity of these species implies that they have too short a lifespan to be detected, so hamper direct measurements. EPR spin-trapping technique represents a useful method to overcome this problem.

The reactive free radicals interact with adequate reagents, the spintraps, to yield spin-adducts, which are longer-living free radicals and can be monitored by EPR spectroscopy at room temperature.

Preventively, we checked that DMPO after irradiation with NIR light does not produce any interfering signals.

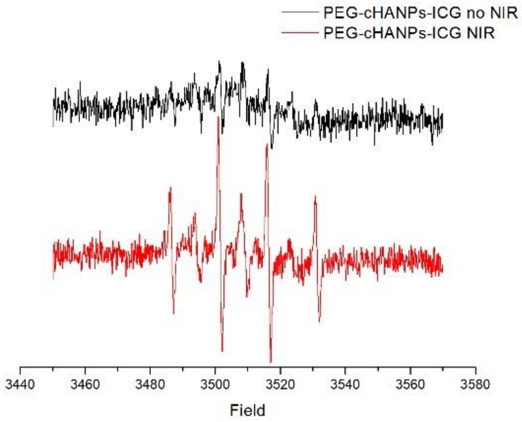

Figure 3. 32: EPR spectra of PEG-cHANPs-loaded with ICG in double condition: irradiated and not

PEG-cHANPs-ICG in aqueous environment causes the appearance of a signal in the EPR spectrum when irradiated, showing a characteristic quartet with a 1 : 2 : 2 : 1 intensity ratio (*Figure 3. 33*).

It corresponds to the DMPO–OH adduct formed from the trapping of -OH radical on DMPO.

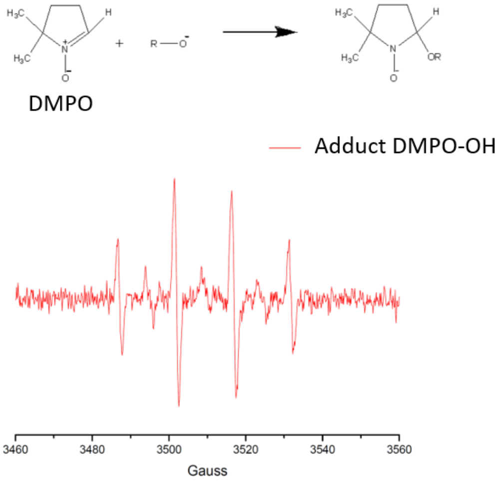

Figure 3. 33: Typical spectrum of DMPO-OH adduct for ROS detecting: intensity peak ratio 1:2:2:1

A quantitative analysis of this spectrum was realized by determination of the hyperfine coupling constants for the nitroxide nitrogen and for the b-proton, aN ¼ aHb ¼ 14.8 fi 0.1 G. These values are consistent with those reported in the literature for the DMPO–OH adducts, confirming the formation of significant amounts of °OH radicals in PEG-cHANPs. There were not detected significant signals of empty PEG-cHANPs in aqueous suspension in the EPR spectrum, thus confirming the absence of any radical species due to polymeric components of the system.

To exclude an interference due to irradiation of DMPO after NIR exposure, a spectrum of only irradiated spintrapper was recorded. Obtained data showed no significant signals.

3.4 Simultaneous encapsulation of Gd-DTPA and Atto 488 in PEG-cHANPs

3.4.1 Introduction

With the aim to produce nanovectors for multimodal imaging in this section we investigated the co-encapsulation of two diagnostic compounds, Gd-DTPA and ATTO 488 in PEG-cHANPs systems. The co-encapsulation process occurs simultaneously, making these particles suitable for multimodal MRI/ Optical diagnostics. In the combination of Optical and MRI imaging, it is possible to exploit 3D anatomical information and excellent spatial resolution provided by the MRI, and the high sensitivity and real-time analysis of the Optical imaging.

Furthermore, the two probes encapsulation has potential for PEGylated crosslinked hyaluronic acid nanoparticles (PEG-cHANPs) in the field of theranostic applications since ATTO488 can be considered as the model of a low Mw drug.

3.4.2 Materials and Methods

Hyaluronate Thiol (HA-SH) with 5 mol % substitution, MW 50 kDa, and mPEG-Vinylsulfone (PEG-VS), MW 2kDa, were purchased from Creative PEGWorks. Diethylenetriaminepentaacetic acid gadolinium (III) dihydrogen salt hydrate Gd-DTPA (97%), Ethanol (ACS reagent, (200 proof), absolute; Acetone (puriss. p.a., ACS reagent, reag. ISO, Ph. Eur., ≥ 99.5%); Sodium Hydroxide NaOH (ACS reagent, ≥ 97.0 %, MW 40.00g/mol), ATTO 488 (λ_{ex}= 504nm, λ_{em}=521nm) were purchased from Sigma-Aldrich, Water for synthesis and characterization, was purified by distillation, deionization, and reserve osmosis (Milli-Q Plus; Merck, Darmstadt, Germany).

The procedure for the synthesis was the same as reported in *Chapter 2,* with slight modification. Briefly, ATTO 488 and Gd-DTPA are added to the HA-SH aqueous solution (0,5%w/V) at a concentration of 10 nmol/mL and 0.1% w/V respectively. Then, the solution is mixed with the crosslinker PEG-VS (at a final concentration of 0,18%w/V) at a low temperature before being processed by microfluidic platform. The standard condition used were: 30µL/min for the middle channel and 110 µL/min for the side channels with acetone. The obtained material was collected in a Petri dish with 25mL of acetone.

- *Confocal microscopy*

Confocal microscopy observations are performed to assess ATTO 488 encapsulation. The presence of spherical fluorescent spots confirms the encapsulation of the dye in spherical nanoparticles. However, nanoparticles size cannot be evaluated due to the low spatial resolution of the optical light.

- *In-vitro T1*

In-vitro longitudinal relaxation time T1 evaluation is performed for pure water as control, empty PEG-cHANPs, PEG-cHANPs loaded with Gd-DTPA and PEG-cHANPs co-loaded with Gd-DTPA and ATTO 488. The longitudinal relaxation time T1 is measured at 37°C and at 1.5 T. Each measurement shows a reduced mean T1 value with respect to pure water.

The loading capability of Gd-DTPA is calculated by Inductively Coupled Plasma (ICP-MS) NexION 350 measurements. All data are collected and processed using the Syngistix Nano Application Module. Gd-DTPA is measured at m/z 157 using a 100 μs dwell time with no settling time. The concentration of loaded fluorophore is determined using Multiplate Reader Photometer (Enspire Perkin-Elmer) (λ ex/em 488-500 nm). The calibration curve is set in the range of 0–0.2 nmol/ml, to avoid system saturation with higher concentration. To overcome the scattering due to the nanoscale size of particles, all measurements are conducted with a dilution ratio of 1:4.

3.4.3 Results and Discussions

Previous optimizations led to the definition of the following conditions as standard conditions for the nanoparticle production: $T = 4°C$, $FR^2 = 0.27$ and $SH/VS = 0.0011$. Starting from these conditions, the simultaneous encapsulation of Gd-DTPA and ATTO 488 was tested to provide multimodal properties to the nanovectors. Briefly, the payload agents are dissolved in the polymer solution before the injection. Later, the nanoprecipitation occurs in the mixing channel producing the encapsulation of the compounds. We have observed that the presence of these two agents is not significantly influencing the stability of the flow focusing in the microfluidic device even if a higher precipitation rate at the interface between the solvent and the non-solvent phase in the mixing channel has been visually observed. DLS and SEM analyses show a slight increase in the mean size at 150 ± 25 nm.

ICP-MS analyses have been used to quantify the amount of Gd-DTPA entrapped in PEG-cHANPs co-loaded with Gd-DTPA and ATTO 488. The amount of loaded Gd-

DTPA was 25%, a value lower than the case of single entrapment of Gd-DTPA (*see Chapter 3.1*).

The amount of co-loaded ATTO 488 has been determined through measurement with a Multiplate Reader Photometer and the effective quantity was calculated starting from a calibration curve. Results showed a loading capability of 60%. In perspective, the encapsulation of the fluorescent compound can be used as a model for a possible drug encapsulation to provide a theranostic function to the system.

Moreover, the relaxation time of free Gd-DTPA at different molar concentrations is measured in order to compare this value to the relaxation time obtained from different nanoparticle formulations. The comparison reveals that T1 = 1640 ms associated to Gd loaded PEG-cHANPs corresponds to an equivalent free-Gd-DTPA content of 135 μM, a value slightly higher than the effective concentration inside our nanosystems (110 μM by ICP-MS measurement), precisely 1.22 times higher than the free Gd-DTPA at the same concentration. Interestingly, Gd-DTPA and ATTO 488 co-loaded PEG-cHANPs analysis reveals a T1=1130 ms, 5 times higher than the T1 signal associated with the same concentration of free Gd-DTPA. However, both Gd loaded and Gd-ATTO co-loaded PEG-cHANPs confirmed the boosting of the Relaxometric properties of the metal chelate and, therefore, also this new formulation is preserving the effect of Hydrodenticity. To explain the synergic effect of the Dye and Gd-chelate on the T1 values, we hypothesize that in the presence of hydrophilic ATTO488, the hydration of the hydrogel nanoparticles is increased because of dye molecules solvation. Indeed, by definition, in the process of solvation, molecules are surrounded by concentric shells of solvent. This can directly affect the mobility of water molecules that are coordinated around Gd-DTPA.

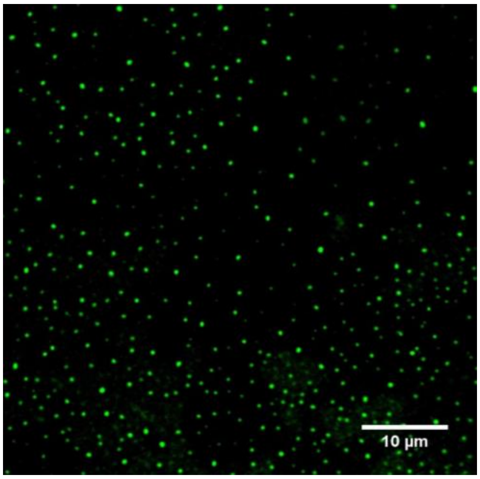

Figure 3. 34: Confocal Image of PEG-cHANPs co-loaded with ATTO488 and Gd-DTPA The green dots represent the fluorescente nanoparticles.

3.5 Chapter 3 References:

1 Holbrook, R. J. *et al.* Gd(III)-Dithiolane Gold Nanoparticles for T-1-Weighted Magnetic Resonance Imaging of the Pancreas. *Nano Letters* **16**, 3202-3209, doi:10.1021/acs.nanolett.6b00599 (2016).

2 Chang, Y., Lee, G. H., Kim, T. J. & Chae, K. S. Toxicity of Magnetic Resonance Imaging Agents: Small Molecule and Nanoparticle. *Current Topics in Medicinal Chemistry* **13**, 434-445 (2013).

3 Frias, J. C., Ma, Y. Q., Williams, K. J., Fayad, Z. A. & Fisher, E. A. Properties of a versatile nanoparticle platform contrast agent to image and characterize atherosclerotic plaques by magnetic resonance imaging. *Nano Letters* **6**, 2220-2224, doi:10.1021/nl061498r (2006).

4 Xue, S. H., Qiao, J. J., Pu, F., Cameron, M. & Yang, J. J. Design of a novel class of protein-based magnetic resonance imaging contrast agents for the molecular imaging of cancer biomarkers. *Wiley Interdisciplinary Reviews-Nanomedicine and Nanobiotechnology* **5**, 163-179, doi:10.1002/wnan.1205 (2013).

5 Lee, N. *et al.* Iron Oxide Based Nanoparticles for Multimodal Imaging and Magnetoresponsive Therapy. *Chemical Reviews* **115**, 10637-10689, doi:10.1021/acs.chemrev.5b00112 (2015).

6 Sampath, S. C. *et al.* Detection of Osseous Metastasis by F-18-NaF/F-18-FDG PET/CT Versus CT Alone. *Clinical Nuclear Medicine* **40**, E173-E177 (2015).

7 Iagaru, A. *et al.* Simultaneous Whole-Body Time-of-Flight F-18-FDG PET/MRI A Pilot Study Comparing SUVmax With PET/CT and Assessment of MR Image Quality. *Clinical Nuclear Medicine* **40**, 1-8 (2015).

8 Do, C., Barnes, J. L., Tan, C. Y. & Wagner, B. Type of MRI contrast, tissue gadolinium, and fibrosis. *American Journal of Physiology-Renal Physiology* **307**, F844-F855, doi:10.1152/ajprenal.00379.2014 (2014).

9 Guglielmo, F. F., Mitchell, D. G. & Gupta, S. Gadolinium Contrast Agent Selection and Optimal Use for Body MR Imaging. *Radiologic Clinics of North America* **52**, 637-+, doi:10.1016/j.rcl.2014.02.004 (2014).

10 Strijkers, G. J., Mulder, W. J. M., van Tilborg, G. A. F. & Nicolay, K. MRI contrast agents: Current status and future perspectives. *Anti-Cancer Agents in Medicinal Chemistry* **7**, 291-305, doi:10.2174/187152007780618135 (2007).

11 Sethi, R. *et al.* Enhanced MRI relaxivity of Gd3+-based contrast agents geometrically confined within porous nanoconstructs. *Contrast Media & Molecular Imaging* **7**, 501-508, doi:10.1002/cmmi.1480 (2012).

12 Chen, G. Y., Roy, I., Yang, C. H. & Prasad, P. N. Nanochemistry and Nanomedicine for Nanoparticle-based Diagnostics and Therapy. *Chemical Reviews* **116**, 2826-2885, doi:10.1021/acs.chemrev.5b00148 (2016).

13 Davies, G. L., Kramberger, I. & Davis, J. J. Environmentally responsive MRI contrast agents. *Chemical Communications* **49**, 9704-9721, doi:10.1039/c3cc44268c (2013).

14 Sierra-Martin, B. & Fernandez-Barbero, A. Multifunctional hybrid nanogels for theranostic applications. *Soft Matter* **11**, 8205-8216, doi:10.1039/c5sm01789k (2015).

15 Pal, K., Banthia, A. K. & Majumdar, D. K. Polymeric Hydrogels: Characterization and Biomedical Applications. *Designed Monomers and Polymers* **12**, 197-220, doi:10.1163/156855509x436030 (2009).

16 Pasqui, D., De Cagna, M. & Barbucci, R. Polysaccharide-Based Hydrogels: The Key Role of Water in Affecting Mechanical Properties. *Polymers* **4**, 1517-1534, doi:10.3390/polym4031517 (2012).

17 Port, M. *et al.* Impact of rigidification on relaxometric properties of a tricyclic tetraazatriacetic gadolinium chelate. *Contrast Media & Molecular Imaging* **1**, 121-127, doi:10.1002/cmmi.99 (2006).

18 Rudovsky, J., Hermann, P., Botta, M., Aime, S. & Lukes, I. Dendrimeric Gd(III) complex of a monophosphinated DOTA analogue: optimizing relaxivity by reducing internal motion. *Chemical Communications*, 2390-2392, doi:10.1039/b418712a (2005).

19 Rudovsky, J. *et al.* PAMAM dendrimeric conjugates with a Gd-DOTA phosphinate derivative and their adducts with polyaminoacids: The interplay of global motion, internal rotation, and fast water exchange. *Bioconjugate Chemistry* **17**, 975-987, doi:10.1021/bc060149l (2006).

20 Tang, J. B., Sheng, Y. Q., Hu, H. J. & Shen, Y. Q. Macromolecular MRI contrast agents: Structures, properties and applications. *Progress in Polymer Science* **38**, 462-502, doi:10.1016/j.progpolymsci.2012.07.001 (2013).

21 Li, Y. *et al.* Macromolecular Ligands for Gadolinium MRI Contrast Agents. *Macromolecules* **45**, 4196-4204, doi:10.1021/ma300521c (2012).

22 Courant, T. *et al.* Hydrogels Incorporating GdDOTA: Towards Highly Efficient Dual T1/T2 MRI Contrast Agents. *Angewandte Chemie-International Edition* **51**, 9119-9122, doi:10.1002/anie.201203190 (2012).

23 Guerard, F., Ray, G. L. & Brechbiel, M. W. MRI WITH GADOLINIUM-BASED NANOPARTICLES. *Nanotechnology for Biomedical Imaging and Diagnostics: from Nanoparticle Design to Clinical Applications*, 223-262 (2015).

24 Okada, S., Mizukami, S. & Kikuchi, K. Switchable MRI contrast agents based on morphological changes of pH-responsive polymers. *Bioorganic & Medicinal Chemistry* **20**, 769-774, doi:10.1016/j.bmc.2011.12.005 (2012).

25 Lux, J. *et al.* Metal chelating crosslinkers form nanogels with high chelation stability. *Journal of Materials Chemistry B* **1**, 6359-6364, doi:10.1039/c3tb21104e (2013).

26 Lux, J., White, A. G., Chan, M., Anderson, C. J. & Almutairi, A. Nanogels from Metal-Chelating Crosslinkers as Versatile Platforms Applied to Copper-64 PET Imaging of Tumors and Metastases. *Theranostics* **5**, 277-288, doi:10.7150/thno.10904 (2015).

27 Oliveira, R. N. *et al.* Mechanical properties and in vitro characterization of polyvinyl alcohol-nano-silver hydrogel wound dressings. *Interface Focus* **4**, doi:10.1098/rsfs.2013.0049 (2014).

28 Manetti, C., Casciani, L. & Pescosolido, N. Diffusive contribution to permeation of hydrogel contact lenses: theoretical model and experimental evaluation by nuclear magnetic resonance techniques. *Polymer* **43**, 87-92, doi:10.1016/s0032-3861(01)00559-6 (2002).

29 Omidian, H. & Park, K. Swelling agents and devices in oral drug delivery. *Journal of Drug Delivery Science and Technology* **18**, 83-93, doi:10.1016/s1773-2247(08)50016-5 (2008).

30 Wood, M. L. & Hardy, P. A. PROTON RELAXATION ENHANCEMENT. *Jmri-Journal of Magnetic Resonance Imaging* **3**, 149-156, doi:10.1002/jmri.1880030127 (1993).

31 Callewaert, M. *et al.* Tuning the composition of biocompatible Gd nanohydrogels to achieve hypersensitive dual T-1/T-2 MRI contrast agents. *Journal of Materials Chemistry B* **2**, 6397-6405, doi:10.1039/c4tb00783b (2014).

32 Russo, M., Ponsiglione, A. M., Forte, E., Netti, P. A. & Torino, E. Hydrodenticity to enhance relaxivity of gadolinium-DTPA within crosslinked hyaluronic acid nanoparticles. *Nanomedicine* **12**, 2199-2210, doi:10.2217/nnm-2017-0098 (2017).

33 Vecchione, D. *et al.* Hybrid Core-Shell (HyCoS) Nanoparticles produced by Complex Coacervation for Multimodal Applications. *Scientific Reports* **7**, 45121 (2017).

34 Vecchione, D. *et al.* Hybrid core shell nanoparticles entrapping Gd-DTPA and F-18-FDG for simultaneous PET/MRI acquisitions. *Nanomedicine* **12**, 2223-2231, doi:10.2217/nnm-2017-0110 (2017).

35 Russo, M., Bevilacqua, P., Netti, P. A. & Torino, E. A Microfluidic Platform to design crosslinked Hyaluronic Acid Nanoparticles (cHANPs) for enhanced MRI. *Scientific Reports* **6**, doi:10.1038/srep37906 (2016).

36 Russo, M. *et al.* PEGylated crosslinked hyaluronic acid nanoparticles designed through a microfluidic platform for nanomedicine. *Nanomedicine* **12**, 2211-2222, doi:10.2217/nnm-2017-0103 (2017).

37 Caravan, P. Strategies for increasing the sensitivity of gadolinium based MRI contrast agents. *Chemical Society Reviews* **35**, 512-523, doi:10.1039/b510982p (2006).

38 Karnik, R. *et al.* Microfluidic platform for controlled synthesis of polymeric nanoparticles. *Nano Letters* **8**, 2906-2912, doi:10.1021/nl801736q (2008).

39 Capretto, L., Carugo, D., Mazzitelli, S., Nastruzzi, C. & Zhang, X. L. Microfluidic and lab-on-a-chip preparation routes for organic nanoparticles and vesicular systems

for nanomedicine applications. *Advanced Drug Delivery Reviews* **65**, 1496-1532, doi:10.1016/j.addr.2013.08.002 (2013).

40 Valencia, P. M., Farokhzad, O. C., Karnik, R. & Langer, R. Microfluidic technologies for accelerating the clinical translation of nanoparticles. *Nature Nanotechnology* **7**, 623-629, doi:10.1038/nnano.2012.168 (2012).

41 Wartenberg, N. *et al.* A Gadolinium Complex Confined in Silica Nanoparticles as a Highly Efficient T1/T2 MRI Contrast Agent. *Chemistry-a European Journal* **19**, 6980-6983, doi:10.1002/chem.201300635 (2013).

42 Zhou, X. *et al.* Gadopentetic acid-doped, multifunctional, potentially targeted mesoporous silica nanoparticles as a novel MRI nano-contrast agent: synthesis, characterization and MRI study. *International Journal of Clinical and Experimental Medicine* **10**, 11442-11453 (2017).

43 Sharma, P. *et al.* Gadolinium-Doped Silica Nanoparticles Encapsulating Indocyanine Green for Near Infrared and Magnetic Resonance Imaging. *Small* **8**, 2856-2868, doi:10.1002/smll.201200258 (2012).

44 Gizzatov, A. *et al.* Geometrical confinement of Gd(DOTA) molecules within mesoporous silicon nanoconstructs for MR imaging of cancer. *Cancer Letters* **352**, 97-101, doi:10.1016/j.canlet.2014.06.001 (2014).

45 Hsu, B. Y. W. *et al.* A Hybrid Silica Nanoreactor Framework for Encapsulation of Hollow Manganese Oxide Nanoparticles of Superior T-1 Magnetic Resonance Relaxivity. *Advanced Functional Materials* **25**, 5269-5276, doi:10.1002/adfm.201501269 (2015).

46 Chen, H. M. *et al.* Mesoporous Silica as Nanoreactors to Prepare Gd-Encapsulated Carbon Dots of Controllable Sizes and Magnetic Properties. *Advanced Functional Materials* **26**, 3973-3982, doi:10.1002/adfm.201504177 (2016).

47 Xie, J., Lee, S. & Chen, X. Y. Nanoparticle-based theranostic agents. *Advanced Drug Delivery Reviews* **62**, 1064-1079, doi:10.1016/j.addr.2010.07.009 (2010).

48 Maqbool, Q., Chanchal, A. & Srivastava, A. Tween 20-Assisted Synthesis of Uniform Mesoporous Silica Nanospheres with Wormhole Porosity for Efficient Intracellular Curcumin Delivery. *Chemistryselect* **3**, 3324-3329, doi:10.1002/slct.201800386 (2018).

49 Stöber W, Fink A & E, B. 62-69 (J. Colloid Interface Sci., 1968).

50 Pan, L. M. *et al.* Nuclear-Targeted Drug Delivery of TAT Peptide-Conjugated Monodisperse Mesoporous Silica Nanoparticles. *Journal of the American Chemical Society* **134**, 5722-5725, doi:10.1021/ja211035w (2012).

51 Pan, D. P. J. *et al.* Nanomedicine strategies for molecular targets with MRI and optical imaging. *Future Medicinal Chemistry* **2**, 471-490, doi:10.4155/fmc.10.5 (2010).

52 tephen, B. S., H., E. P. & Edward, T. Vol. 60 309-319 (J . *Am. Chem. Soc*, 1938).

53 de Oliveira, L. F. *et al.* Tailored Silica Nanoparticles Surface to Increase Drug Load and Enhance Bactericidal Response. *Journal of the Brazilian Chemical Society* **28**, 1715-1724, doi:10.21577/0103-5053.20170017 (2017).

54 Sheng, Z. H. *et al.* Indocyanine Green Nanoparticles for Theranostic Applications. *Nano-Micro Letters* **5**, 145-150, doi:10.5101/nml.v5i3 (2013).

55 Saxena, V., Sadoqi, M. & Shao, J. Degradation kinetics of indocyanine green in aqueous solution. *Journal of Pharmaceutical Sciences* **92**, 2090-2097, doi:10.1002/jps.10470 (2003).

56 Alander, J. T. *et al.* A review of indocyanine green fluorescent imaging in surgery. *International journal of biomedical imaging* **2012**, 940585-940585, doi:10.1155/2012/940585 (2012).

57 Saxena, V., Sadoqi, M. & Shao, J. Enhanced photo-stability, thermal-stability and aqueous-stability of indocyanine green in polymeric nanoparticulate systems. *Journal of Photochemistry and Photobiology B-Biology* **74**, 29-38, doi:10.1016/j.jphotobiol.2004.01.002 (2004).

58 Saxena, V., Sadoqi, M. & Shao, J. Polymeric nanoparticulate delivery system for Indocyanine green: Biodistribution in healthy mice. *International Journal of Pharmaceutics* **308**, 200-204, doi:10.1016/j.ijpharm.2005.11.003 (2006).

59 Saxena, V., Sadoqi, M. & Shao, J. Indocyanine green-loaded biodegradable nanoparticles: preparation, physicochemical characterization and in vitro release. *International Journal of Pharmaceutics* **278**, 293-301, doi:10.1016/j.ijpharm.2004.03.032 (2004).

60 Genina, E. A., Kuzmina, M. Y., Pankov, S. S., Bashkatov, A. N. & Tuchin, V. V. in *2006 Saratov Fall Meeting.* H5351-H5351 (Spie-Int Soc Optical Engineering, 2007).

3.6 Chapter 3 List of Figures:

Chapter 4:

PRELIMINARY BIOLOGICAL APPLICATION OF PEG-cHANPS and *IN-VITRO* TEST

The use of nanosystems in medicine is a great promise for cancer theranostic applications. In this chapter we investigate the in-vitro cytotoxicity of the PEG-cHANPs nanosystem loaded with Gd-DTPA and ATTO 488,(see Chapter 3 for NPs synthesis) for cancer therapy and diagnosis. First of all, we investigate nanosystem toxicity on different cell lines, with the aim to obtain a more general characterization of biological PEG-cHANPs properties. For this reason, we select two different cancer cell lines for cytotoxicity and cellular interaction studies: Panc-1, human epithelioid carcinoma of pancreatic tissue, A549 cells, human epithelial carcinoma of lung tissue and U87-MG for brain cancer. Moreover, system stability has been investigated in different serums for a better understanding of the nanovector behaviours when the formation of the protein corona occurs. After that, starting from previously obtained results, we investigate the possibility to functionalize our NPs with a peptide to create a vector for the Blood-Brain Barrier (BBB) crossing.

4.1 Introduction

To reach the target disease sites it is necessary to consider the behaviour of nanoparticles after entering in the human body. Ideally, once delivered in the body for a particular medical intent, the nanoparticles should perform their desired function and exit from the body without causing any side effects. Several investigations have revealed that many nanoparticles exhibit minor to major hazardous/toxic effects. Thus, it is essential to comprehensively analyze nanoparticles from their toxicological perspective to carry out their clinical translation. Indeed, these stages represent one of the most common points of failure for the clinical applications of therapy and diagnosis based on nanosystem[1-4].

Nanoparticles may diffuse in biological systems and interact within various tissues, cells, and subcellular compartments. The balance between the adhesion of diffusing nanoparticles and hydrodynamic radius, determines the interaction with the surface of the cell membrane. This balance determines also the cellular uptake, in other words, it determines how fast the nanoparticles can diffuse across the cell membrane and consequently reach the interior of the cell. Nanosystem manifests different physicochemical properties when analyzed *in vivo,* compared to their properties after synthesis. Indeed, adsorption of blood components and interactions with phagocytes can modify the size, aggregation state, and interfacial composition of a nanomaterial, giving it a distinct "biological identity"[5]. For this reason, it is fundamental to take into account the *in vitro* behaviour of the nanosystem before testing it *in vivo.*

Cellular uptake mechanism *in vitro* is influenced by medium composition, particularly by the protein content, and by the surrounding conditions, the particle concentrations, the thickness of the medium on the top of the cell layer, and the medium perfusion. The biological parameters that have also need to be taken into account include cell size, proliferation rate, growth pattern and expression of uptake routes .[6]

The biological media can contain thousands of biomolecules. The blood plasma, that represents the first biological media encountered by NPs in systemic delivery, alone has almost 3700 identified proteins, thus allowing the formation of different combinations and organizations of coronas on NPs[7]. Despite the huge numbers of identified proteins, only a few dozens of proteins form the hard corona, since their affinity to the NP bare surface is very high, even if their current abundance in the biological fluid is low. According to Lundqvist's work, the proteins identified on the surface of NPs incubated in human plasma can be organized in different groups[8]. Each nanoparticle would have a unique biological identity that reflects in unique particle-protein organizations.

For a given NPs, only several dozen proteins bind to in surface in significant amounts and long enough to be biologically significant and recognized by the cell. The recognition can either be generic or highly specific, involving receptor-ligand interactions and leading to the binding of NPs to the cell, mediated by the corona[6]. This will lead to its internalization as well as the particle size and surface charge in different exposure media, which will influence the cellular uptake, with a previous possible reorganization of the cell membrane, or can even inhibit the role of surface engineering of NPs.

So, the primary contact between NPs and cells is mediated by NPs surface in the biological medium: when NP surface enters in a biological medium or body fluid, it will be modified by the adsorption of biomolecules such proteins and lipids, culminating in the formation of a layer of molecules called “protein corona”.

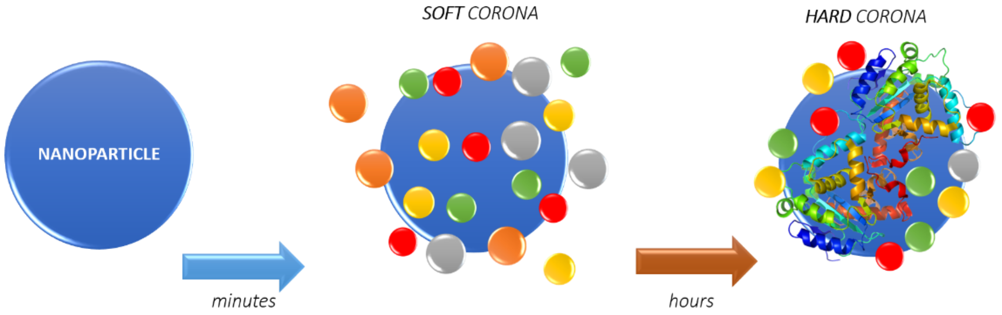

Figure 4. 1: Schematic illustration and characteristics of a hard and a soft corona. The protein corona encompassing the nanoparticles. Hard coronas are characterized by slow exchange (ie, several hours) and lower abundance, with a high affinity of proteins, whereas soft coronas are typified by rapid exchange (ie, several minutes) and lower affinity of proteins with weakly bound outer layers on nanoparticles. There is a different response of cellular and biochemical factors by soft and hard corona formation.

The protein corona has a dynamic nature since a limited number and specific type of biomolecules will compete for the NPs surface, resulting in a corona containing few identifiable proteins. If the exchange kinetics is slow enough (depending on the coating proteins and the experimental setup), the corona will be biologically relevant, and as a front line of contact with the cells, becomes the NPs biological identity[9]. In other words, the identity, organization and lifetime of these proteins adsorbed on NPs surface affect the way cells will interact with, recognize and process them [10].

Dawson and Lynch hypothesized that once NP is dispersed in any biological fluid, a cell will only “see” the system in which the core nanoparticle is surrounded by a “hard” corona of slowly exchanging proteins, tightly bound, and an outer layer of weakly interacting protein-protein complexes, rapidly exchanging with the proteins present in the environment that represents the so-called “soft” corona. Between the two, the inner hard corona is of high scientific relevance and also the most studied (*Figure 4. 1*) [9,11-14].

4.1.1 The role of NPs properties in protein corona formation

Size, shape and surface properties are the most decisive particle-related parameters for cellular uptake and might influence the relation of the phagocyte to non-phagocyte uptake[15]. Lundqvist et all categorized different hard corona formations on NPs by different chemistries (untreated polystyrene NP, carboxyl-modified, and amine-modified) with different sizes (50 and 100 nm). Interestingly, both size and surface charge played a significant role in determining the NP-coronas, even for identical NPs materials. 50-nm NPs have relatively few complement-pathway proteins detected in their coronas. These variations in which complement-pathway proteins bind as a function of NPs charge and size might suggest that different particles activate different complement pathways to different extents, and again this is a topic of considerable interest for future investigations[8]. Also, zeta potential is involved in the adsorption of proteins onto NPs. If the zeta potential is positive, NPs directly adsorb albumin, which shows a negative charge at natural conditions[16]. On the other hand, if the zeta potential is negative, for example, for TiO_2, NPs adsorb albumin through cations such as calcium[17]. Albumin is a major calcium-binding protein, and thus, calcium is an important mediator in the protein adsorption ability of NPs. When those NPs are dispersed in a complete culture medium, the adsorbed protein is almost exclusively serum albumin [18].

4.1.2 Functionalized PEG-cHANPs: the case study of crossing the Blood-Brain Barrier

Particular attention in cancer study is given to malignant brain tumors due to poor diagnosis and high recurrence. Glioblastoma multiforme (GBM) is an intracranial tumor that arises from glial tissue of the brain. The finger-like tentacles of astrocyte cells (cells from which gliomas arise) result in highly infiltrative tumors. These tumors allocate and rapidly grow into deep areas of the brain making local accessibility difficult. Glioblastoma represents the 78% of all malignant brain tumors, with a major impact on males than females. It leads to death in most patients and the length of survival following diagnosis is 12 to 15 months, with fewer than 3% to 5% of people surviving longer than 5 years; without treatments, the survival rate is only 3 months[19-21]. Nowadays surgery, radiation and chemotherapy are three modalities used in glioma therapy. After initial diagnosis, the ordinary procedure is an intracranial debulking, that is generally safe but is a really highly invasive technique that can damage the central nervous system (CNS). Furthermore, the migration of tumor cells from the apparent tumor boundaries coupled with a lack of high-resolution imaging modalities for the detection of tumor cells leads to tumor recurrence. Alternatively, several anti-cancer chemicals drugs are used as first-line treatment in glioblastoma therapy, but their efficiency is limited by several factors such as non-specific toxicity, poor pharmacokinetics, therapy resistance, potential brain damages and non-specific targeting of the tumor site. Glioma shares some common manifestations with peripheral tumors such as elevated interstitial pressure, low pH, low pO_2 and infiltrated growth, all of which present great challenges to effective drug penetration. The principal problem to reach the tumor cells is crossing the Blood-Brain Barrier (BBB)[22-24].

The BBB is a highly selective membrane formed by tightly bound endothelial cells (*Figure 4. 2*). Apart from the physical barrier, active efflux pumps on the surface of BBB endothelial cells prevent toxic substances from entering the brain. Moreover, the BBB is further bolstered by a layer of intracellular enzymes capable of metabolizing a wide range of xenobiotic compounds. Small hydrophobic molecules can cross the BBB via passive diffusion. Large therapeutic molecules that are incapable of passively diffusing through the BBB can be assisted by external stimuli[25]. A potential risk associated with BBB disruption strategies is the eventual entrance of toxic substances into the brain.

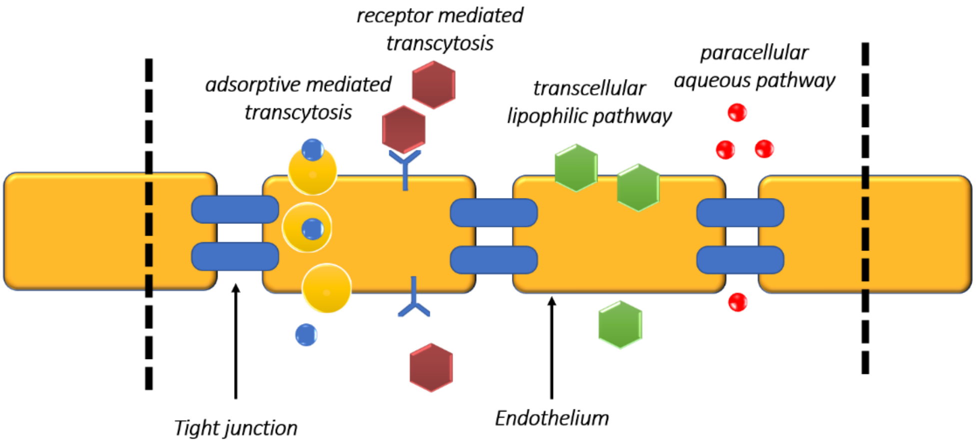

Figure 4. 2: Schematic representation of different types of transport mechanism able to across the Blood Brain Barrier.

Currently, there are three different methodologies to reach the tumour sites of interest:

- Direct brain delivery

- Direct systemic delivery
- Indirect systemic delivery

The first method increases the concentration of drugs in the brain, but it’s not enough because the compounds are not able to make a specific targeting to tumoral cells[26,27]. This problem is enhanced in the systemic delivery of the drugs, indeed the molecule has to by-pass multiple barriers before reaching the brain tumor site such as pass metabolism, opsonization, phagocytosis, hepatic and immune system. A further improvement to the NPs design can be the addition of surface ligands in order to target the tumor cells. Two disadvantages may be due to multi-ligands attachment to the nanoparticle. The first disadvantage is that many different ligands on nanoparticles surface may result in a cumbersome nanoparticle affecting both: its mobility and drug release[23]. The second disadvantage is that the targeting efficiency of the nanoparticles may be reduced as a result of competitive binding and interactions among the ligands[28]. Therefore, researchers have explored the use of a single ligand for dual BBB and tumor cell targeting[29]. Two such ligands are anti-transferrin and angiopep. Anti-transferrin ligand bound nanoparticles can cross the BBB via transferrin receptors. Since glioma tumor cells also overexpress transferrin receptors on their surface, the nanoparticles can migrate towards the tumors. Angiopep is also another ligand whose receptor, low-density lipoprotein receptor-related protein (LRP), is overexpressed on both BBB and glioma cells[30].

4.1.3 Direct conjugation with peptide Angiopep-2

Demeule et al.[31]in 2008, identified a family of peptides named Angiopep. These peptides, and in particular Angiopep-2, exhibited high transcytosis capacity across BBB ECs and parenchyma accumulation.

Angiopep-2 is a positively charged peptide of 19 amino acids identified by sequence alignment of aprotinin with other human protein having a Kunitz domain which interact with LRP1. The low-density lipoprotein receptor-related protein (LRP1) is highly expressed (BBB) and mediated the transcytosis of multiple ligands across the BBB. LRP1 was also over-expressed in human glioma cells. Therefore angiopep-2 peptides are effective at trans-cytosing the BBB and targeting glioma cells[32]. From that moment, increasing interest in this peptide arose in literature.

Huile et al[33], conjugated PEG-PCL nanoparticles with Angiopep-2 demonstrating both in vitro and *ex-vivo* enhancement of brain uptake. However, the same results were not obtained by Rooy et al[34]., demonstrating that Angiopep-2 does not target the brain *in-vivo* when coupled to a liposomal delivery vehicle. The experiments were conducted selecting five targeting ligands (transferrin, RI7217, COG133, Angiopep-2, and CRM197) and comparing their ability to target liposomes to the brain *in-vitro* and *in-vivo*. Only the RI7217 was able to significantly enhance brain uptake *in vivo*. The very same observation came from Chen at al. [35]. These observations have an important implication: when Angiopep-2 is conjugated, the targeting efficiency can be enhanced or reduced depending on the specific carrier on which it is conjugated.

Indeed, in more recent applications, Angiopep-2 has been used as a dual-targeting ligand for brain delivery when conjugated to polymeric nanoparticles. Xin et al.[30] developed Paclitaxel-loaded PEG-PCL nanoparticles conjugated with Angiopep-2. They started from the observation of Demeule et al. that demonstrated that LRP1 receptors are overexpressed also on glioma cells[32] and used Angiopep-2 as a dual-targeting ligand both for BBB crossing and for tumor targeting. In vivo results showed a high particle accumulation in the brain and no acute toxicity to the hematological system, liver, kidney, and brain tissue. The same group studied the uptake mechanism of conjugated nanoparticles on the U87 Glioblastoma cell line, confirming that the transcytosis mechanism through LRP1 receptors is the preferential transport pathway[36] . The selected peptide could be also used as a shuttle for the transport of a wide range of cargoes[37]. The high versatility of this peptide as shuttle is confirmed by the different nanoparticle's diameter used, from 7 nm up to 200 nm. Furthermore, the number of peptides required for efficient delivery is relatively low: four peptides are considered optimal for 7-8nm dendrons and 53 peptides on the surface of a 90nm nanoparticle provided efficient transport.

In this context, the current section reports the use of biocompatible PEG-cHA NPs, produced as reported in *Chapter 3*, that are conjugated with Angiopep-2 for *in-vitro* evaluations.

4.2 Materials and Methods

Thiolated Hyaluronate (HA-SH Mw =50000 Da; Substitution degree=5%), Polyethyleneglycol-vinylsulfone (PEG-VS Mw= 2000 Da SD= 100% linear chain;

Mw= 2000 Da,) were purchased from Creative PEGWorks (USA). , Gadolinium-diethylenetriamine penta-acetic acid (Gd-DTPA Mw = 547,43 g/mol) N-(3-Dimethylaminopropyl)-N'-ethylcarbodiimide hydrochloride (EDC molecular formula $C_8H_{17}N_3{\cdot}HCl$ Mw = 191,70 g/mol), N-Hydroxysuccinimide (NHS molecular formula $C_4H_5NO_3$; Mw=115,09 g/mol) were purchased from Merck KGaA (Germany), Angiopep-2 (Mw = 2625.8 g/mol) was purchased from ProteoGenix SAS (France), Acetone (CHROMASOLV, for HPLC, ≥99,8%; molecular formula CH_3COCH_3; Mw=58,08), Ethanol (ACS reagent, ≥99,5% (200 proof), absolute; molecular formula CH_3CH_2OH; Mw=46,07), Sodium Hydroxide NaOH (ACS reagent, ≥97,0%, Mw=40,00). Water, used for synthesis and characterization, was purified by distillation, deionization, reverse osmosis (Milli-Q Plus) and finally filtered with a 0,22 µm cutoff filter. Wheat Germ Agglutinin Alexa FluorTM 555 Conjugate (WGA 555) for cell membrane and vesicle staining were purchased from Thermo Fischer©. Atto 488 fluorescent label (Em/Ex 488/520) was purchased from ATTO-TEC GmbH (Germany). Dulbecco Modified Eagle Medium high glucose (DMEM), Fetal Bovine Serum (FBS), Phosphate Buffer Saline (PBS), Trypsin, Penicillin/Streptomycin, L-glutamine, Minimum Essential Medium α-Modification (α-MEM), Roswell Park Memorial Institute Medium (RPMI) and Human Serum Albumin (HSA) for cell culture and *in-vitro* study were purchased by Sigma Aldrich. The cell culture media used in this work was Dulbecco's Modified Eagle's Medium (DMEM, Gibco©). Panc-1, human epithelioid carcinoma of pancreatic tissue, and A549 cell lines human epithelial carcinoma of lungtissue were purchase from(??)U-87 MG cell lines, human epithelial-like of glioblastoma astrocytoma (passage 15-36) were purchased from ATCC. Angiopep-2 ($Mw = 2625.8\ g/mol$) was purchased from ProteoGenix SAS (France).

4.2.1 *In vitro* analysis

- *Cell culture*

The selected cell lines for the NPs *in-vitro* study were: the Panc-1 human epithelioid carcinoma of pancreatic tissue, U87-MG human epithelial-like of glioblastoma astrocytoma andA549 cells human epithelial carcinoma of lung tissue. The last one was used as a control cell line. Panc-1, U-87 MG and A549 cells were cultured at 37°C in 5% CO_2 in Dulbecco's Modified Eagle's Medium (DMEM), supplemented with 2mM Glutamine and 10% Fetal Bovine Serum (FBS) and 1% penicillin/ streptomycin (Gibco, Invitrogen, Belgium). A549 cells were passaged every 48 h and split 1/5, Panc-1 cells were passaged every 48 h and split 1/3 while U87-MG were passaged every 48h and split 1/5. Cells were passaged when reaching near 80% confluency by lifting the cells with 0.05% trypsin (Gibco) and were plated (1/5 or 1/3) onto 75cm^2 flasks.

In vitro cytotoxicity: Panc-1 and A459 cell lines

- *Cell viability, Oxidative stress and mitochondrial health*

After cell labeling cells were washed twice with 100 µl PBS/well to remove any remaining NPs. It was added to each well (100 µl/well) the medium with 200nM of MitoTracker and 100 nM of Image-iT DEAD Green and the cells were incubated for 30 min at 37°C in a 5% CO2 atmosphere. Cells were then washed twice with PBS and fixed with 4% paraformaldehyde for 15 min at room temperature in dark conditions. The fixative was then washed away with 100 µl PBS/well and treated with 4′,6- diamidino-2-phenylindole (DAPI; Molecular Probes, Invitrogen, Belgium) at 300 nM in PBS for 10 min in the dark. Each well was aliquoted with 100 µl of PBS and plates were analyzed on the InCell 2000 analyzer (GE Healthcare Life Sciences, Belgium) where phase contrast and fluorescence-based images for the red, green and blue channel were collected at minimum 2000 cells/well.

- *InCell analyzer*

The InCell Analyzer 2000 is an automated microscope designed for fast, automated imaging and analysis of fixed and live cells. The primary imaging mode is fluorescence microscopy. In fluorescence microscopy, the sample (for example, a human cell) is stained with one or more dyes that bind to certain structures of interest within the sample. The dyes are designed to fluoresce when illuminated with specific wavelengths of light; the fluorescent light that is emitted is also of a specific wavelength. During imaging, the sample was illuminated by the light of a specific wavelength. This causes any dyes with matching excitation profiles to emit light. An objective lens gathers the fluorescent light emitted by the sample, and various optics are used to direct the light towards a very sensitive CCD camera. Images taken with this camera can show, for example, the appearance and position of structures in the sample.

- *InCell developer Software*

Data acquired by InCell Analyzer were analyzed by the InCell Developer software (GE Healthcare Life Sciences, Belgium) using in-house developed protocols. Cell viability evaluation: the level of cell viability was calculated as follows: First, cells were segmented based on the phase contrast images and cell cytoplasm was then segmented based on the green channel using the segmented phase contrast images as seed images. Then, the total number of cells was diminished by the number of dead cells (red channel; dead cells are defined as clear red dots, with intensity levels minimally 3-fold above noise level and size of minimally 2 μm^2 - within the cytoplasmic area of a single cell, where multiple red dots can be colocalized with a single cytoplasmic area). These values were then normalized to the control values (= 1) to indicate the degree of cell viability.

- *Oxidative stress and mitochondrial health evaluation*

The level of oxidative stress was calculated as follows: first, cells were segmented based on the phase contrast images and cell nuclei was segmented based on the green channel (upon oxidation, the CellROX probe will localize to the nucleus). The intensity of every nucleus was then calculated and normalized to the intensity level of untreated control cells (100%). Mitochondrial health was evaluated similarly, where the intensity of the MitoTracker Red CMXRos probe depends on the mitochondrial membrane potential and thus is lost in nonfunctional mitochondria. All red spots localized within a single cytoplasm (based on phase contrast images using the green channel as seed images for the nucleus) were counted and the average intensity of all mitochondria per cell was then measured. This value was then normalized to the intensity level of untreated control cells (100%). All measurements were done in triplicates.

In vitro cytotoxicity: U87-MG cell lines

• Flow cytometry

Flow cytometer is a powerful tool used for the examination of characteristics and phenotyping of the cells. It is based on the property of light scattering by cells. Flow cytometry is a system for sensing cells or particles as they move in a liquid stream through a laser/ light beam passing the sensing area. The relative light-scattering (Forward Scattering FSC and Side Scattering SSC) and color-discriminated fluorescence (Fluorescence Laser FL1) of the microscopic particles are measured and analyzed. Differentiation of the cells is based on size, granularity, and whether the cell is carrying fluorescent molecules in the form of either antibodies or dyes. As the cell passes through the laser beam, light is scattered in all directions. The light scattered in the forward direction is at low angles (0.5–10°) from the axis. This scattering is proportional to the square of the radius of a sphere and so as to the size of the cell or particle. The scattered light may be considered to have entered the cell and be reflected and refracted by the nucleus and other contents of the cell and it represents granularity of the cell. All the analyses have been conducted on a Cyflow ® Space Partec.

• Flow cytometry protocol

$2x10^5$ U87 MG cells/well were seeded in 12-well plates (Falcon®) and incubated for 24h before the addition of NPs. Afterwards, cells were incubated with culture medium supplemented with the different serum within study and the different NPs for 3 contact time such as 30 minutes, 4 hours and 24 hours. The final concentration of PEG-cHANPs used in the incubation solution was 50µg/mL. Negative controls consisted of the complete medium condition (medium, FBS, L-glutamine and penicillin/streptomycin) but without NPs. At any contact time, the medium was removed, and the samples were washed three times with PBS to ensure the removal of the non-internalized nanoparticles. The fluorescence intensity of all PBS washes of the 24-well plates demonstrated the efficiency of the washes, following particle removal. Cells were then trypsinized for 5 min at 37ºC. After cell detachment confirmation at optical microscope, complete medium was added to neutralize the trypsin and all the content was transferred to polystyrene round-bottomed tubes (Falcon®), before samples were immediately analyzed by flow cytometry, or were centrifuged at 1000rpm for 5 minutes to remove trypsin, fixed with 4% paraformaldehyde (PFA), centrifuged again and resuspended in PBS before being analyzed. Every flow cytometry study has been conducted in triplicate, and the average of the three repetitions was used for both FSC and FL1 in order to obtain reliable results in terms of cellular uptake and viability information. Samples were analyzed acquiring at most 30000-20000 cells. A 488nm wavelength laser was used to excite NPs fluorescence, which was collected using a 595-660 nm spectral detection channel. Results are reported as the mean of the distribution of cell fluorescence intensity obtained by measuring 3000 events averaged between 3 independent replicas. Error bars correspond to the standard deviation between.

- *Confocal Microscopy:*

Confocal Laser Scanning Microscopy (CLSM) is an optical imaging technique for increasing optical resolution and contrast of a micrograph through using a spatial pinhole to block out-of-focus light in image formation. Capturing multiple twodimensional images at different depths (z-stack) it is possible to obtain a 3D reconstruction of the sample structure. In contrast with a conventional fluorescence microscope (where all parts of a specimen are excited at the same time so that a large unfocused background part of fluorescence is detected by microscope's photodetector), confocal microscopes use point illumination and a pinhole in an optically conjugate plane in front of the detector to eliminate out-of-focus signal, obtaining better resolution than wide-field microscopes. However, the increased resolution is at cost of decreased signal, so long exposures are usually required. To solve the problem of signal, sensitive detectors are used (photomultipliers PMT or hybrid detectors) which can transform the light signal into an electrical one that is recorded by a computer. One-point illumination requires scanning of the specimen to obtain a complete image. In fluorescence observations, the resolution limit of confocal microscopy is often limited by the signal to noise ratio caused by the small number of photons typically available in fluorescence microscopy.

To achieve the best resolution, Nyquist theorem says that

$$p.s = 1/2R$$

where p.s. is the pixel size and R is the nominal resolution of the instrument (200nm usually) and suggests that pixel size should be 1/2 of the nominal resolution. Parameters that control pixel size are different, so that Nyquist condition can be obtained by:

- Increasing laser intensity (risking specimen damaging);
- Acquiring more than one image and considering the average (line average);
- Increasing gain;

- Reducing zoom.

Qualitative assessment of *in-vitro* NPs internalization has been performed using an TCS SP5 Confocal Laser Microscope (Leica Microsystems©). Two lasers with different wavelengths were used for excitation of Atto 488 and WGA 555 dyes, respectively at 488 nm and 543 nm excitation and 500-530 nm and 560-610 nm emission wavelengths (it is necessary to not overlap excitation and emission intervals). HCX PL APO CS 63x1.40 Oil objective was used; laser intensities were between 5 and 20%. After sample positioning on the stage, the transmitted light is used to first focusing, before acquisitions.

- *Working solutions (WS) preparation protocol:*

This preparation protocol was composed of several steps:

- A solution of 3mL of PBS (1X)
- Vortex PEG cHANPs for 30 seconds
- Add WGA 555 (1:1000)
- Add FBS 10% or HSA 20% (ignore for no serum condition)
- 300 µL/well of WS was then added to seeded cells

The final concentration of NPs used in the working solution was 50 µg/mL for PEG-cHANPs. Negative controls consisted of the complete medium condition (medium, FBS, L-glutamine and penicillin/streptomycin) and WGA 555 but without NPs. The medium was then removed, three washes with PBS (1x) were performed and samples were then fixed with 4% paraformaldehyde (PFA) for 15 minutes, and cells were stored at 4°C until confocal microscopy was performed.

- *Confocal microscopy protocol*

8x10^4 U87 MG cells were seeded in 8-well µ-slide (inverted for high-end microscopy) (Ibidi®) and incubated at 37°C for 24 hours. Afterwards, cells were incubated with a working solution (WS) consisting of culture medium supplemented with the different sera under study, different NPs and Wheat Germ Agglutinin Alexa FluorTM 555 Conjugate (Thermo Fischer©) fluorochrome at 1:1000 concentration for 30 minutes, 2 hours and 4 hours.

4.2.2 NPs stability in different serum

- *Formation of Protein Corona on NPs:*

The dispersions of NPs were prepared by diluting the concentrated stock solutions in complete medium (DMEM or RPMI; supplemented with the different % of sera defined in *Table 4. 1*) or serum-free medium (SFM) used for cell culture at room temperature, immediately prior to the experiments on cells, with an identical time delay between diluting and introducing NPs to the cells for all experiments. Before sampling, NPs were vigorously mixed by vortex for 30 seconds. After the addition of the NPs to the different incubation solutions, these were also vortexed for 15 seconds to ensure maximum NPs dispersion.

The obtained systems have been characterized by DLS measurements, TEM images and cell viability at different time points.

Table 4. 1 In the table are indicated the serum % range used for the preparation of complete medium (CM).

SERUM	**SERUM % Added to SFM**
FSA	10%
HAS	16.4-20.5%

4.2.3 Direct conjugation with Angiopep-2

- *Functionalization Protocol*

PEG-cHANPs conjugation with Angiopep-2 peptide was obtained by activation of available carboxyl groups on particles surface, using two reagents: EDC, for the formation of an unstable reaction intermediate, and NHS for a second, stable reaction intermediate.

Stock solution preparation:

- 37 mg of EDC are dissolved in 2.5 mL of Water (0.07M)
- 6 mg of NHS are dissolved in 2.5 mL of Water (0.02M)
- 1 mg of Angiopep-2 is dissolved in 1 mL of Water (0.38 M)

Activation of available carboxyl groups on the nanoparticle surface through EDC and NHS:

- 500 µL of PEG-cHANPs water suspension
- 250 µL of EDC stock solution (0.07M)
- 250 µL of NHS stock solution (0.02M)
- 10 min of stirring on the wheel

Peptide addition:

- 50 *μL* of Angiopep-2 stock solution (0.019 M) was added to both activated nanoparticle solutions.
- 4 *h* of wheel stirring

NPs purification:

- Corning centrifugation of the sample at 1000 rpm for 10 minutes.

- *Optimization conjugation protocol*

The reported protocol for peptide addition has been also studied with the aim to obtain a higher yield of the reaction. Two different amounts of peptide were used with different times of rection on a wheel (overnight, 4hours and 1,5 hours).

- *Bicinchoninic Acid Assay*

The bicinchoninic acid assay (BCA assay, sensitivity: 0.5 μg/ml), also known as the Smith assay, is used for quantitation of total protein in a sample, in this case allowing to measure the concentration of the peptide on the surface of the PEG-cHANPs. It is based on the principle that under alkaline conditions the copper Cu^{+2} ions form a complex with peptide bonds of proteins and are reduced to Cu^{+1}. In addition, the presence of a specific chemical compound (purple colour) allows quantifying the amount of protein present in the sample of interest. The intensity variation was determined by absorbance spectrophotometer measurement at 562 nm. In a typical protocol, 150 μL of the NPs suspension reacts with an equal amount of working reagent solution and then the mixture is incubating at 37°C for 2 h. The results are compared with a bovine serum albumin (BSA) calibration curve and the concentration value is then extrapolated by a straight line of calibration built using BSA samples of known concentration (0 - 40 µg/mL). All measurements were performed in triplicate.

- *Spectrofluorometer*

Spectrofluorometry (or fluorescence spectrophotometry) measures the fluorescence signature of an analyte in a sample based on its specific excitation and emission wavelengths. The fluorescence signature can be correlated to the concentration level of the analyte in the sample. In the presented work spectrofluorometry was used for BCA assay detection with the above BCA procedure. All measurements have been conducted on an EnSpire Multimode Plate Reader PerkinElmer.

4.3 Result and discussion

4.3.1 Stability and cytotoxicity of PEG-cHANPs loaded with Gd-DTPA and ATTO488.

Nanoparticles are recognized by biological systems as foreign materials. This event may generate an adverse effect on the host site. These host-guest interactions could trigger nanotoxicity.

To understand the toxicological properties of PEG-cHANPs, loaded with GD-DTPA and ATTO488, contact tests with cell lines have been conducted. Representative images (control and NPs highest concentration-100µg/ml) are shown for the Panc-1 and A549 cells line exposed to the PEG-cHANPs loaded with GD-DTPA and ATTO488 (*Figure 4. 3* and *Figure 4. 4*). In the case of Panc-1, the cytotoxicity analysis reveals low numbers of dead cells for all concentrations tested as reported in the graph in *Figure 4. 3.a-b.*

This result matches with the images obtained by InCell analyzer, where it is possible to observe a slight reduction in the number of cells compared with the control at the highest concentration of NPs used (*Figure 4. 3.c*).

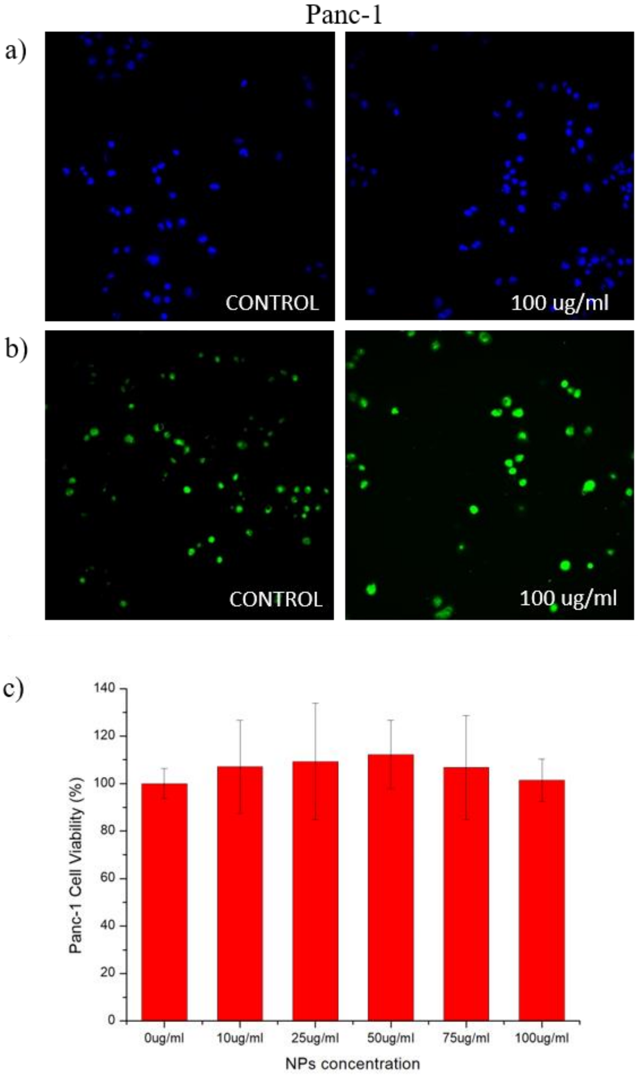

Figure 4. 3: The panel shows the Panc-1 cell a) DAPI and b) DEAD Green Viability results with a comparison between the control and the highest concentration of nanoparticles (100μg/ml). The graph bar (c) shows the cell viability of different NPs concentrations.

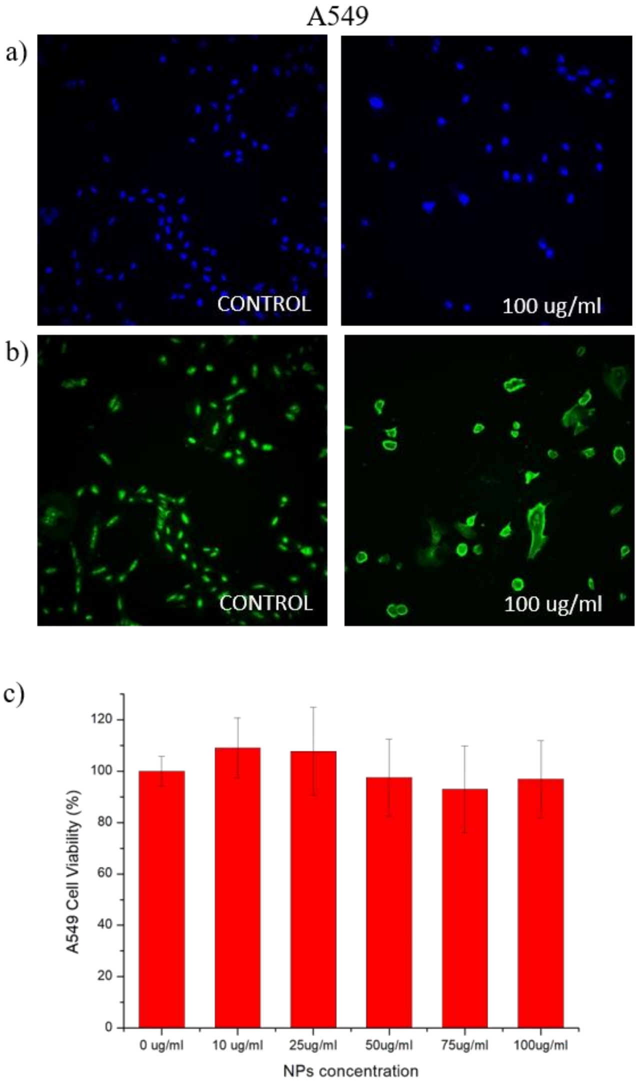

Figure 4. 4: The panel shows the A549 cell a) DAPI and b) DEAD Green Viability results with a comparison between the control and the highest concentration of nanoparticles (100µg/ml). The graph bar (c) shows the cell viability of different NPs concentrations.

In detail, it is possible to see the difference in cell viability for a set of concentration thanks to the overlapping of DAPI (blue) and DEAD Green Viability staining (green) channels. If the DEAD Green Viability staining overlaps the DAPI one, it means that the nuclei of the cells are damaged. Similar behaviour has been observed also in the case of A459 cell lines (*Figure 4. 4*).

It was also determined NP-induced ROS production by InCell analyzer measurements. Data revealed concentration-dependent induction of ROS (*Figure 4. 5* and *Figure 4. 6*), most prominently for higher concentrations of nanoparticles. This trend is consistent with the one reported for the cell viability. When there is a cell suffering, it is linked to a reduction in cell area and an increase in ROS production (*Figure 4. 5 b-c* and *Figure 4. 6 b-c*). In detail, it is possible to see the reduction of the MitoTracker channel related to the Mithocondria Staining. The A549 cell line results more influenced than Panc-1 by the presence of NPs.

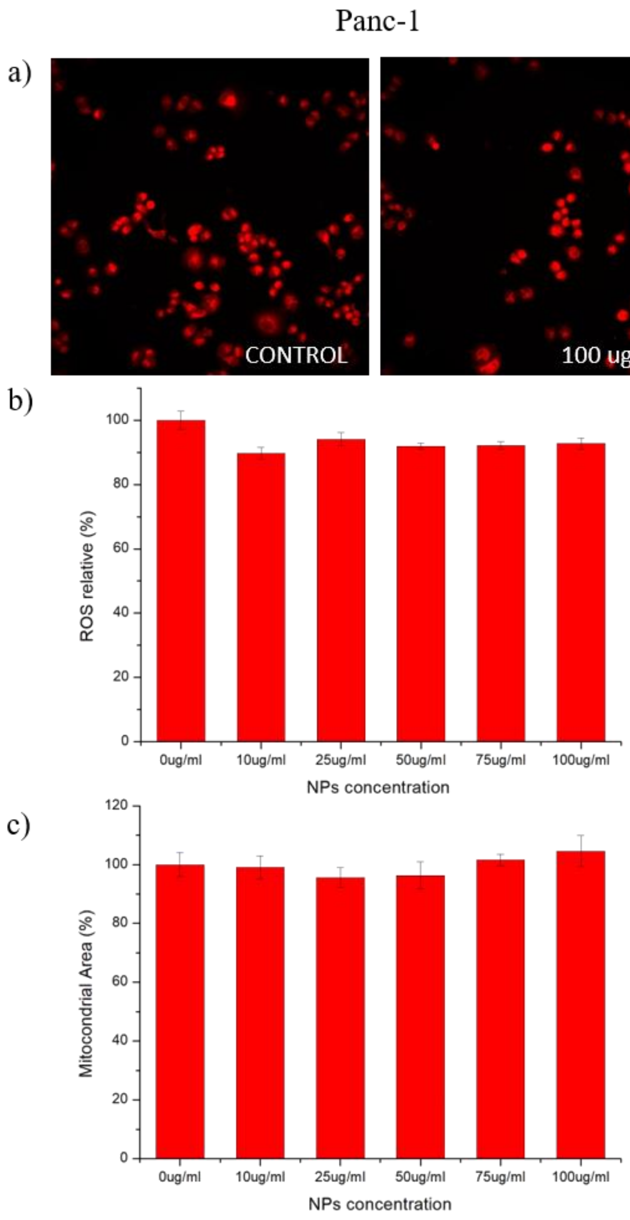

Figure 4. 5:: In the panel were reported the ROS analysis with corresponded mitocondrial area variations for the Panc-1 cell line.

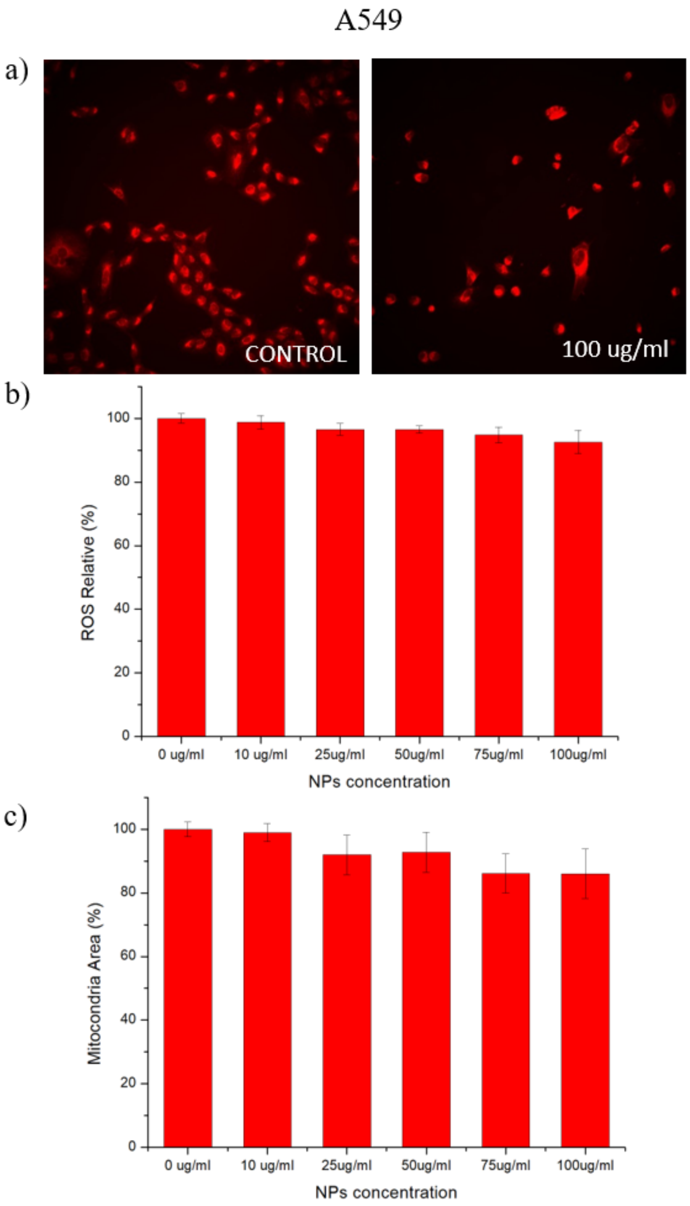

Figure 4. 6: In the panel were reported the ROS analysis with corresponded mitocondrial area variations for the A549 cell line.

4.3.2 Stability study on protein corona

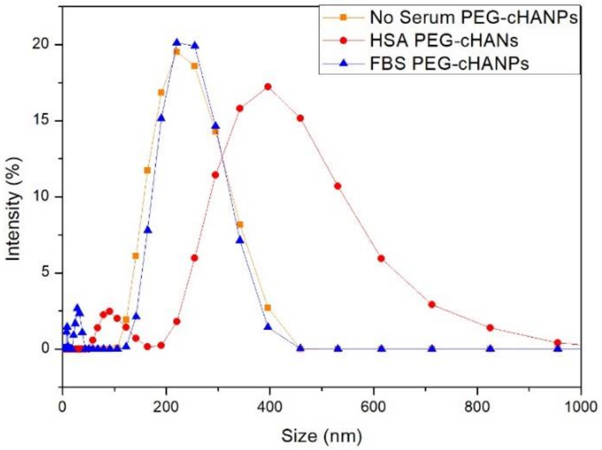

Figure 4. 7: DLS measurement of PEG-cHANPs after 30 min of contact with different serum..

DLS analysis were performed to obtain information about the dispersity and size of PEG-cHANPs in the presence and absence of biological fluids. Results in *Figure 4. 7* show that protein corona causes an increase in NPs size. Polydispersity also increases, suggesting that protein corona formation is not a repeatable phenomenon because free proteins aggregate formation. The NPs stability after the formation of the protein corona has also been also investigated (*Figure 4. 8*). The reported graph showed a good stability in the condition of no serum, while in contact with FBS or HSA there is a variation on NPs size until two hours of contact, after that we can assume a stabilization regarding the interaction between serum and NPs.

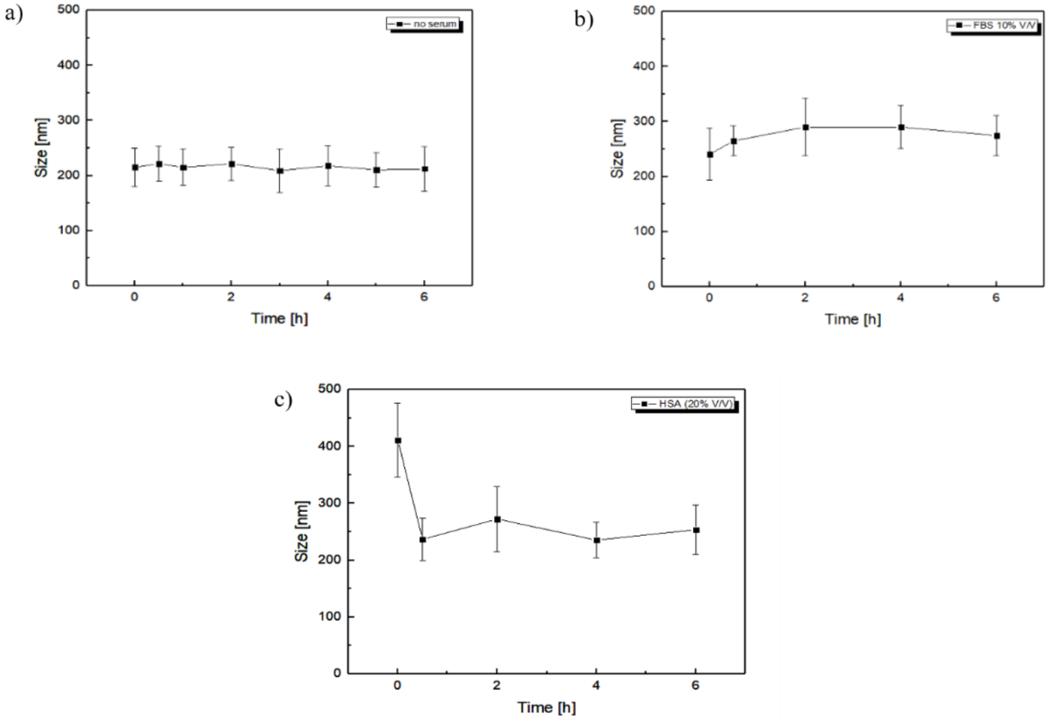

Figure 4. 8: Study on NPs stability during the time in no serum a), FBS b) and HSA c).

TEM analysis were performed to obtain information on NPs structure and stability after the protein-corona formation. *Figure 4. 9* shows a size growth after protein corona formation in agreement with the DLS results previously reported. Furthermore, the structural integrity of NPs after protein adsorption is maintained even if the presence of protein corona increases NPs surface rugosity. PEG-cHANPs show a continuous corona, suggesting a high biological affinity with PEG-cHANPs nanoparticles precursors (HA and PEG are biocompatible).

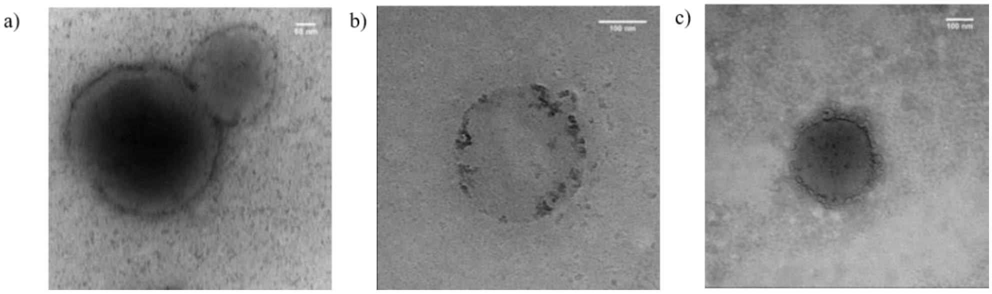

Figure 4. 9: TEM images of PEG-cHANPS naked a), after 1 hour of contact with FBS b) and after 1 hour of contact with HAS c).

Flow cytometry analysis was conducted using the U-87MG cell line to test cell viability after PEG-cHANPs treatment. Prior to the treatment, the NPs were incubated in two different serums such as FBS and HSA. Forward Scattering (FSC) values are reported for PEG-cHANPs as a cell viability parameter (*Figure 4. 10*). It is visible that FSC remains at standard values for PEG-cHANPs., allowing us to assert that the investigated nanosystem has no cytotoxic effect after 4 hours of treatment also in the presence of protein corona.

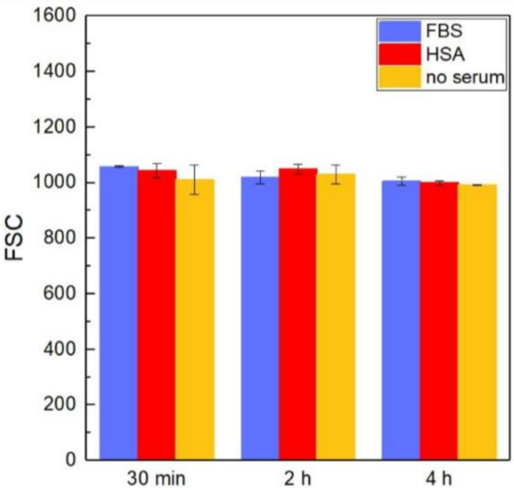

Figure 4. 10: Cell viability of U87-MG after contact with PEG-cHANPs in three serum conditions and three different time points. Forward Scattering (FSC) values are correlated as a cell viability parameter.

4.3.3 Conjugation for BBB crossing nanovector

Bioconjugation is the reaction carried out to bind covalently a molecule to the particle surface. In this work, the peptide Angiopep-2 has been successfully conjugated on PEG-cHANPs surface.

The conjugation reaction has been performed with different peptide concentrations and optimized to 50 $\mu g/mL$. The purification protocol through corning centrifugation has been optimized by trying different combinations of eluent volume, rpm and time of centrifugation. The final conditions for conjugation have been fixed to 1 mL of eluent per mL of sample, 1000 rpm for 15 min. Conjugation reaction characterization has been performed through the BCA assay and the peptide quantity calculated starting from a calibration curve (*Figure 4. 11*).

Flow cytometry analysis, conducted in contact with the U-87MG cell line, was also used to make a comparison of internalization value and cell viability for PEG-

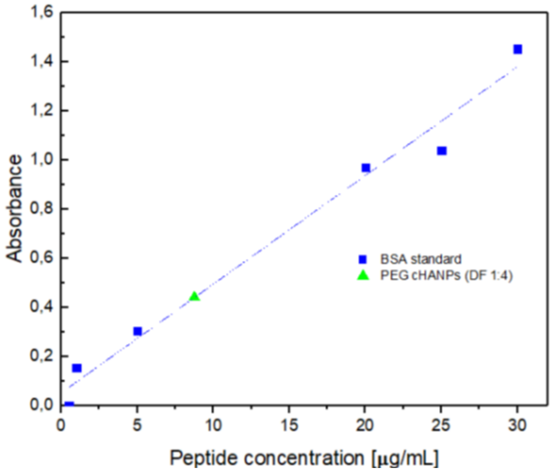

Figure 4. 11: Spectrofluorometry measurements have been conducted to generate a BCA calibration curve for evaluation of Peg-cHANPs conjugation. During the analysis the O.D. value has been registered at 562nm.

cHANPs necked, PEG-cHANPs after engineering functionalization and with the only peptide Angiopep-2 (*Figure 4. 12*).

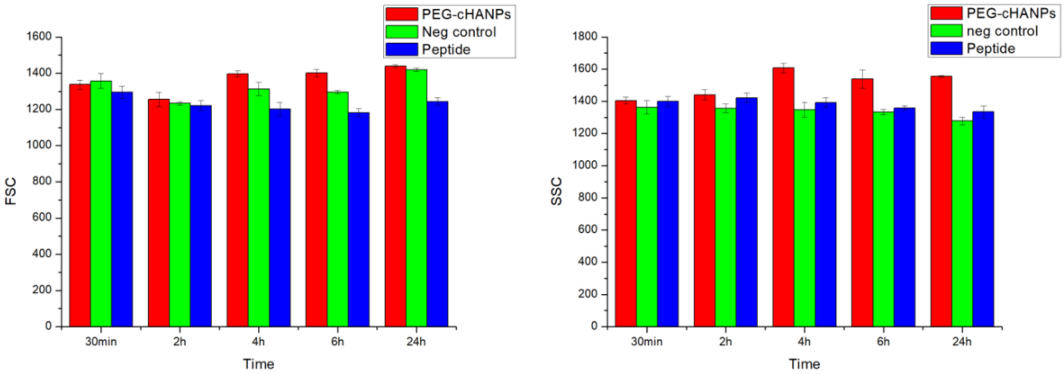

Figure 4. 12: Flow cytometry measurements have been conducted on necked and engineered PEG-cHANPs and on only peptide solution. FSC parameter reveals a good viability for all cases, while the SSC parameter, correlated to the internalization process, shows that the system NPs plus peptide have a higher interaction with the U-87MG cell line.

Nevertheless, the goodness of peptide functionalization required further study and optimization because the structural stability of nanoparticles after the engineering process cannot be demonstrated. This instability could be attributed to stronger conditions of purification step after conjugation.

4.9 Conclusion

In this section, it is proved that the PEG-cHANPs show a general effect of non-cytotoxicity at a concentration of 100ug/ml. The systems can be successfully used in combination with different biological serum showing stability until 6 hours. Furthermore, the presence of carboxylic groups on the surface allows functionalizing these nanovectors with suitable peptide to ensure the transport of cargo agents across the BBB.

The small size of the obtained nanovectors can be exploited in order to deliver different loaded agents at the tumour site, overcoming the BBB also at early disease stages.

In conclusion, the new nanoprobe results are very promising regarding their use as diagnostic tools for glioblastoma disease allowing an active targeting to the tumour site thanks to the presence of a BBB crossing peptide. Further analysis of these nanovectors will be performed, in particular for multimodal applications combining MRI and Optical Imaging.

4.4 Chapter 4 References:

1 Ross, K. A. *et al.* Nano-enabled delivery of diverse payloads across complex biological barriers. *Journal of Controlled Release* **219**, 548-559, doi:10.1016/j.jconrel.2015.08.039 (2015).

2 Choi, H. S. *et al.* Renal clearance of quantum dots. *Nature Biotechnology* **25**, 1165-1170, doi:10.1038/nbt1340 (2007).

3 Aillon, K. L., Xie, Y. M., El-Gendy, N., Berkland, C. J. & Forrest, M. L. Effects of nanomaterial physicochemical properties on in vivo toxicity. *Advanced Drug Delivery Reviews* **61**, 457-466, doi:10.1016/j.addr.2009.03.010 (2009).

4 Lewinski, N., Colvin, V. & Drezek, R. Cytotoxicity of nanoparticles. *Small* **4**, 26-49, doi:10.1002/smll.200700595 (2008).

5 Walkey, C. D., Olsen, J. B., Guo, H. B., Emili, A. & Chan, W. C. W. Nanoparticle Size and Surface Chemistry Determine Serum Protein Adsorption and Macrophage Uptake. *Journal of the American Chemical Society* **134**, 2139-2147, doi:10.1021/ja2084338 (2012).

6 dos Santos, T., Varela, J., Lynch, I., Salvati, A. & Dawson, K. A. Quantitative Assessment of the Comparative Nanoparticle-Uptake Efficiency of a Range of Cell Lines. *Small* **7**, 3341-3349, doi:10.1002/smll.201101076 (2011).

7 Monopoli, M. P. *et al.* Physical-Chemical Aspects of Protein Corona: Relevance to in Vitro and in Vivo Biological Impacts of Nanoparticles. *Journal of the American Chemical Society* **133**, 2525-2534, doi:10.1021/ja107583h (2011).

8 Lundqvist, M. *et al.* The Evolution of the Protein Corona around Nanoparticles: A Test Study. *Acs Nano* **5**, 7503-7509, doi:10.1021/nn202458g (2011).

9 Lynch, I. & Dawson, K. A. Protein-nanoparticle interactions. *Nano Today* **3**, 40-47, doi:10.1016/s1748-0132(08)70014-8 (2008).

10 Ho, Y. T., Kamm, R. D. & Kah, J. C. Y. Influence of protein corona and caveolae-mediated endocytosis on nanoparticle uptake and transcytosis. *Nanoscale* **10**, 12386-12397, doi:10.1039/c8nr02393j (2018).

11 Lee, Y. K., Choi, E. J., Webster, T. J., Kim, S. H. & Khang, D. Effect of the protein corona on nanoparticles for modulating cytotoxicity and immunotoxicity. *International Journal of Nanomedicine* **10**, 97-112, doi:10.2147/ijn.s72998 (2015).

12 Power, D. *et al.* A multiscale model of protein adsorption on a nanoparticle surface. *Modelling and Simulation in Materials Science and Engineering* **27**, 17, doi:10.1088/1361-651X/ab3b6e (2019).

13 Khan, S., Gupta, A. & Nandi, C. K. Controlling the Fate of Protein Corona by Tuning Surface Properties of Nanoparticles. *Journal of Physical Chemistry Letters* **4**, 3747-3752, doi:10.1021/jz401874u (2013).

14 Brancolini, G., Bellucci, L., Maschio, M. C., Di Felice, R. & Corni, S. The interaction of peptides and proteins with nanostructures surfaces: a challenge for nanoscience. *Current Opinion in Colloid & Interface Science* **41**, 86-94, doi:10.1016/j.cocis.2018.12.003 (2019).

15 Rejman, J., Oberle, V., Zuhorn, I. S. & Hoekstra, D. Size-dependent internalization of particles via the pathways of clathrin-and caveolae-mediated endocytosis. *Biochemical Journal* **377**, 159-169, doi:10.1042/bj20031253 (2004).

16 Wassell, D. T. H. & Embery, G. Adsorption of bovine serum albumin on to titanium powder. *Biomaterials* **17**, 859-864, doi:10.1016/0142-9612(96)83280-7 (1996).

17 Klinger, A., Steinberg, D., Kohavi, D. & Sela, M. N. Mechanism of adsorption of human albumin to titanium in vitro. *Journal of Biomedical Materials Research* **36**,

387-392, doi:10.1002/(sici)1097-4636(19970905)36:3<387::aid-jbm13>3.0.co;2-b (1997).

18 Cristian, R. E. *et al.* Analyzing the Interaction between Two Different Types of Nanoparticles and Serum Albumin. *Materials* **12**, 16, doi:10.3390/ma12193183 (2019).

19 Bhojani, M. S., Van Dort, M., Rehemtulla, A. & Ross, B. D. Targeted Imaging and Therapy of Brain Cancer Using Theranostic Nanoparticles. *Molecular Pharmaceutics* **7**, 1921-1929, doi:10.1021/mp100298r (2010).

20 Sun, C. M. *et al.* Noninvasive nanoparticle strategies for brain tumor targeting. *Nanomedicine-Nanotechnology Biology and Medicine* **13**, 2605-2621, doi:10.1016/j.nano.2017.07.009 (2017).

21 Li, M. H., Deng, H. B., Peng, H. S. & Wang, Q. Functional Nanoparticles in Targeting Glioma Diagnosis and Therapies. *Journal of Nanoscience and Nanotechnology* **14**, 415-432, doi:10.1166/jnn.2014.8757 (2014).

22 Chen, Y. & Liu, L. H. Modern methods for delivery of drugs across the blood-brain barrier. *Advanced Drug Delivery Reviews* **64**, 640-665, doi:10.1016/j.addr.2011.11.010 (2012).

23 Khan, A. R., Liu, M. R., Khan, M. W. & Zhai, G. X. Progress in brain targeting drug delivery system by nasal route. *Journal of Controlled Release* **268**, 364-389, doi:10.1016/j.jconrel.2017.09.001 (2017).

24 Saraiva, C. *et al.* Nanoparticle-mediated brain drug delivery: Overcoming blood-brain barrier to treat neurodegenerative diseases. *Journal of Controlled Release* **235**, 34-47, doi:10.1016/j.jconrel.2016.05.044 (2016).

25 Yang, F. Y. *et al.* Focused ultrasound and interleukin-4 receptor-targeted liposomal doxorubicin for enhanced targeted drug delivery and antitumor effect in

glioblastoma multiforme. *Journal of Controlled Release* **160**, 652-658, doi:10.1016/j.jconrel.2012.02.023 (2012).

26 Mujokoro, B., Adabi, M., Sadroddiny, E. & Khosravani, M. Nano-structures mediated co-delivery of therapeutic agents for glioblastoma treatment: A review. *Materials Science & Engineering C-Materials for Biological Applications* **69**, 1092-1102, doi:10.1016/j.msec.2016.07.080 (2016).

27 Allard, E., Passirani, C. & Benoit, J. P. Convection-enhanced delivery of nanocarriers for the treatment of brain tumors. *Biomaterials* **30**, 2302-2318, doi:10.1016/j.biomaterials.2009.01.003 (2009).

28 Van't Root, M., Lowik, C. & Mezzanotte, L. Targeting Nanomedicine to Brain Tumors: Latest Progress and Achievements. *Current Pharmaceutical Design* **23**, 1953-1962, doi:10.2174/1381612822666161227153359 (2017).

29 Frosina, G. Nanoparticle-mediated drug delivery to high-grade gliomas. *Nanomedicine-Nanotechnology Biology and Medicine* **12**, 1083-1093, doi:10.1016/j.nano.2015.12.375 (2016).

30 Xin, H. L. *et al.* Anti-glioblastoma efficacy and safety of paclitaxel-loading Angiopep-conjugated dual targeting PEG-PCL nanoparticles. *Biomaterials* **33**, 8167-8176, doi:10.1016/j.biomaterials.2012.07.046 (2012).

31 Demeule, M. *et al.* Identification and design of peptides as a new drug delivery system for the brain. *Journal of Pharmacology and Experimental Therapeutics* **324**, 1064-1072, doi:10.1124/jpet.107.131318 (2008).

32 Bertrand, Y. *et al.* Transport characteristics of a novel peptide platform for CNS therapeutics. *Journal of Cellular and Molecular Medicine* **14**, 2827-2839, doi:10.1111/j.1582-4934.2009.00930.x (2010).

33 Gao, H. L. *et al.* A cascade targeting strategy for brain neuroglial cells employing nanoparticles modified with angiopep-2 peptide and EGFP-EGF1 protein. *Biomaterials* **32**, 8669-8675, doi:10.1016/j.biomaterials.2011.07.069 (2011).

34 van Rooy, I., Mastrobattista, E., Storm, G., Hennink, W. E. & Schiffelers, R. M. Comparison of five different targeting ligands to enhance accumulation of liposomes into the brain. *Journal of Controlled Release* **150**, 30-36, doi:10.1016/j.jconrel.2010.11.014 (2011).

35 Chen, C. T. *et al.* Peptide-22 and Cyclic RGD Functionalized Liposomes for Glioma Targeting Drug Delivery Overcoming BBB and BBTB. *Acs Applied Materials & Interfaces* **9**, 5864-5873, doi:10.1021/acsami.6b15831 (2017).

36 Xin, H. *et al.* The brain targeting mechanism of Angiopep-conjugated poly(ethylene glycol)-co-poly(epsilon-caprolactone) nanoparticles. *Biomaterials* **33**, 1673-1681, doi:10.1016/j.biomaterials.2011.11.018 (2012).

37 Oller-Salvia, B., Sanchez-Navarro, M., Giralt, E. & Teixido, M. Blood-brain barrier shuttle peptides: an emerging paradigm for brain delivery. *Chemical Society Reviews* **45**, 4690-4707, doi:10.1039/c6cs00076b (2016).

4.5 Chapter 4 List of Figures:

Chapter 5:

CONCLUSIONS

A microfluidic-based process has been proposed to design a new class of Drug Delivery Systems for multimodal applications, in the form of intravascularly-injectable and biocompatible hydrogel nanostructures.

The proposed microfluidic method allows strict control of the physicochemical properties of the nanoparticles and the direct functionalization with PEG molecules to overcome the RES system. Our findings are interesting to investigate how the microfluidic environment determines the NPs size and stabilization, to facilitate also the further application of this rapidly growing technique. Typically, the microfluidics enables a fast mixing in the microchannels promoting the formation of nanomaterials at laminar flow condition. By taking advantages from that, in our system it has been possible to obtain more monodisperse and stable nanoparticles of defined size than the ones produced by similar bulk and microfluidic approaches.

In the first part of the thesis, the tunability of the hydrogel nanostructures, able to entrap rationally a clinically-relevant agent, through a microfluidic flow focusing method, is exploited and monodisperse crosslinked PEGylated-Hyaluronic Acid Nanoparticles (PEG-cHANPs) of 140 nm in diameter are produced by a controlled nanoprecipitation, overcoming the limits of common batch processes, and guaranteeing an instantaneous formulation and absence of purification step.

Furthermore, the crosslinking reaction is studied and performed, simultaneously to the nanoprecipitation, to improve the stability of the polymer matrix, to increase the loading capability and reduce swelling effects. Obtained results show that the crosslinking parameters (e.g. concentration, SH/VS ratio and temperature) needed for Michael addition reaction occurrence in the HFF approach are more efficient compared to the required for batch process.

In the second part of the thesis, the developed nanosystems were loaded with different active compounds. Indeed, multicomponent nanosystems represent a key instrument for personalized, targeted and regenerative medicine by delivering the next level of new drugs and treatments for real breakthroughs in healthcare. Hence difference strategies to optimize the loading capabilities of microfluidic system have been evaluated. Firstly, we entrapped Gd-DTPA as contrast agent for MRI, achieving a low polydispersity of nanoparticles and a high encapsulation efficiency of the metal compound within the nanoparticles. Moving from the Hydrodenticity concept, we exploited the ability to influencing the Gd-DTPA relaxivity by hydrogel structural parameters obtained through a microfluidic flow-focusing approach. The structures of produced crosslinked PEGylated hyaluronic acid nanoparticles are connected to the characteristic correlation times of the Gd-DTPA. Relaxometric performances are assessed in terms of longitudinal relaxivity r1. In in vitro analysis, showed that the r1 relaxivity of the Gd-loaded PEG-cHANPs is increasing up to 1,2 times at specific formulations, without the chemical modification of the relevant clinical chelate.

After that we analyzed the possibility to produce a hybrid system composed of mesoporous silica nanoparticles and hydrogel matrix, exploiting a nanoprecipitation process in microfluidics. To use SiO_2 nanosystems with defined features, new syntheses have been studied with comparison to direct and inverse micelles method for sol-gel procedure. In this way, the pre-synthesized SiO_2 NPs were coated by polymeric matrix loaded with Gd-DTPA. This result confirms the versatility of our microfluidic platform for the development of complex systems loaded with different agents.

In order to engineer a multimodal nanovector, we decide to combine Gd-DTPA for MRI and ICG for Optical Imaging. Not only the loaded capabilities of the PEG-cHANPS have been investigated but a study on ICG degradation in polymeric solution has been conducted. Our finding can be a helpful guideline for describing the stability of ICG dye in a hydrogel matrix in different solvent and environmental condition (such as pH, storage condition and salt presence). The unusual wavelength windows used for the characterization can be applied also for other systems with ICG.

Finally, in the last part of the thesis, to study the in vitro cytotoxicity of PEG-cHANPs, a system co-loaded with Gd-DTPA and ATTO488 was produced.

It is important to highlight that further benefits of our study are supported by the use of completely biocompatible and FDA approved products, the simplicity of the synthesis and the scalability of the proposed process.

Activities along three years

Papers:

- Russo M, Grimaldi AM, Bevilacqua P, **Tammaro O**, Netti PA, Torino E (2017). *PEGylated crosslinked hyaluronic acid nanoparticles designed through a microfluidic platform for nanomedicine.* DOI: 10.2217/nnm-2017-0103
- Vitiello G, Zanfardino A, **Tammaro O**, Di Napoli M, Caso M, Pezzella A, Varcamonti M, Silvestri B, D'Errico G, Costantini A and Luciani G (2018) *Bioinspired hybrid eumelanin–TiO2 antimicrobial nanostructures: the key role of organo–inorganic frameworks in tuning eumelanin's biocide action mechanism through membrane interaction.* DOI: 10.1039/C8RA04315A
- **Tammaro O**, Costagliola A, Netti PA, Torino E (2020). *One-Step Synthesis of Multimodal Imaging Nanoparticles by a Hydrodynamic Flow Focusing approach.* Paper under revision
- **Tammaro O.**, Netti P.A, De Cola L., Torino E. (2020). *Design of one- step process for Gd-DTPA loaded porous Silica NPs: synthesis and characterization.* Paper under submission
- **Tammaro O**, Netti P.A., De Cola L., Torino E., (2020) *Design of hybrid nanostructures SiO_2 -HA-PEG exploiting a Hydrodynamic flow focusing approach.* Paper under submission

Partecipation to Conferences/Seminars:

- II UNITO-POLITO Conference Series in Cancer- Imaging in Cancer Dynamics, March 2018, Turin, Italy
- 6th International Conference on Multifunctional, Hybrid and Nanomaterials (HYMA 2019), March 2019, Stiges, Spain
- Overcoming the Blood-Brain Barrier: Post-resection drug delivery to Glioblastoma Multiforme using Supramolecular Hydrogels *Prof. Oren Sherman*, July 2019, ISIS, Strasbourg, France

- Biomaterials and engineered microenvironments to control cell behavior *Prof. Giovanna Brusatin*, July 2019, ISIS, Strasbourg, France
- New in vivo optical imaging tools for cancer and stem cell research *Prof. Clemens Löwik*, 2018, UNINA, Naples, Italy
- Updates in glioblastoma: New applications in glioblastoma treatment *Prof. Gerolama Condorelli*, May 2018,UNINA, Naples, Italy May 2018
- Power of Light: Photo-Triggered Microcapsules *Prof. Tylkowski,* 2017, Naples, Italy

Communication to Conference:

- **Tammaro O**, Russo M, Netti PA, Torino E, *One-step synthesis of Hyaluronic Acid – Polyethylene Glycol nanoparticles for Multimodal Imaging by a microfluidic platform*, Poster session, 6th International Conference on Multifunctional, Hybrid and Nanomaterials (HYMA 2019), March 2019, Stiges, Spain

Other activities:

- XIX Summer School INSTM “Materials science and technologies approaches to biomedical challenges”, Prof. Andrea Caneschi Ischia, Naples July 2017
- Visiting Researcher @ Prof. De Cola group- ISIS, Strasburg, France, June-September 2019
- Biostart Internship Programme with University of Lodz, Poland 2018
- 1st StarShip Programme by European Innovation and Technology – EIT Health, Europe March-November 2017
- EIT-Health Knowledge-Transfer day, Naples 2017

HydroBlink is an entrepreneurial idea designed to develop advanced collyrium for refractive surgery. **HydroBlink** proposes an ophthalmic product to be administered after refractive surgery, able to relieve pain and facilitate vision recovery, thus improving patients’ quality of life. **HydroBlink** has developed a unique formulation through the use of nanotechnology, consisting of a microparticle suspension. It is designed to form a uniform layer, adherent to the ocular surface and support the natural re-epithelization process of the cornea.

- Award at StartCup Campania with the project “**HydroBlink**”, 13thOctober 2017,Naples, Italy.
- Premio Nazionale Innovazione (PNI 2017) with the project “**HydroBlink**”, 12 30thNovember – 1st December,Naples, Italy
- XI Best Practice with the project “**HydroBlink**”, 12 – 13th December 2017,Salerno, Italy
- EIT- Slim Project with the project “**HydroBlink**” May 2019 Naples, Delft
- EIT JumpStarter Bootcamp with the project “**HydroBlink**” April-June 2019 Naples